

Anton Tamtögl

# Adsorptions- und Desorptionsprozesse auf reinem und Zn-modifiziertem Pd(111)

DIPLOMARBEIT  
zur Erlangung des akademischen Grades  
Diplom-Ingenieur  
der Studienrichtung Technische Physik



Technische Universität Graz

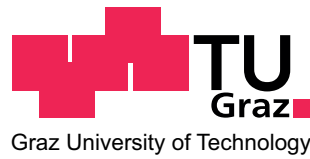
Betreuer:  
Ao.Univ.-Prof. Dipl.-Ing. Dr.techn. Adolf Winkler  
Insitut für Festkörperphyisk

Graz, Mai 2008

Anton Tamtögl

# Adsorption and Desorption Processes on Clean and Zn-Modified Pd(111)

DIPLOMA THESIS



Graz University of Technology

Advisor:

Ao.Univ.-Prof. Dipl.-Ing. Dr.techn. Adolf Winkler  
Institute of Solid State Physics

Graz, May 2008

# Acknowledgement

This diploma thesis was performed under the supervision of Univ. Prof. Dr. tech. Adolf Winkler. I would like to thank for his brilliant mentoring and his dedicated and friendly support.

Dipl. Ing. Markus Kratzer introduced me into the experimental handling. I am grateful for his extraordinary helpfulness and many fruitful discussions about the concerning physics behind the experiments.

Moreover, I would like to thank all members of the surface science group for the pleasant and cooperative working atmosphere.

This research was supported in part by a grant from the FWF.

# Abstract

In the present work the interaction of hydrogen/deuterium, carbon monoxide and oxygen with clean and zinc covered palladium (111) surfaces has been investigated under ultra-high vacuum conditions. The main experimental techniques used were thermal desorption spectroscopy (TDS), Auger electron spectroscopy (AES) and low energy electron diffraction (LEED). Zinc was evaporated by a Knudsen cell and the amount of Zn was determined by a quartz microbalance. In addition to a "normal" Pd(111) sample, a Pd(111) crystal as part of a permeation source was used. In the latter case the deuterium exposure was performed by permeation through the bulk which allowed the investigation of angular distribution measurements on these surfaces.

At low temperatures (150 K) zinc forms an epitaxial overlayer which starts to grow in islands at low coverages. With increasing temperature (above 300 K) the zinc layer starts to build a Pd/Zn surface alloy with a  $(2 \times 1)$  superstructure. Thermal desorption of zinc layers with high coverages leads to a low temperature peak (400-600 K) arising from upper zinc layers and a second peak (above 800 K) originating from the lower zinc layers which are more strongly bound. To get additional information about the desorption kinetics the TD spectra were fitted according to simulated desorption rates and the heat of adsorption was determined.

It is shown that a thick zinc layer ( $\approx 10$  ML) blocks the adsorption of CO and H<sub>2</sub>. Furthermore, on the Pd/Zn surface alloy the adsorption of hydrogen on surface sites is reduced whereas the diffusion into the subsurface region is not influenced. In addition the heat of adsorption for CO is shifted to much lower values on the Pd/Zn surface alloy than compared to Pd(111) which is due to the fact that zinc alters the interactions of CO with the surface. Different preparation conditions of the zinc layer give rise to a change in the CO desorption spectra. Hence one gets an idea about the formation of the Pd/Zn surface alloy and further alloying in the subsurface region.

Moreover, a ZnO layer was prepared by oxidation of the Zn layer. ZnO forms an overlayer of the hexagonal ZnO Wurtzite (0001) plane on Pd(111) which causes a  $(6 \times 6)$  superstructure. In addition, it is shown that the ZnO layer may be reduced by CO via the formation of CO<sub>2</sub> as well as by H<sub>2</sub> via the formation of H<sub>2</sub>O.

# Kurzfassung

Die vorliegende Arbeit befasst sich mit der Wechselwirkung von Wasserstoff/Deuterium, Kohlenmonoxid und Sauerstoff mit Zink-bedeckten Palladium (111) Oberflächen im Ultrahochvakuum. Als wichtigste verwendete experimentelle Techniken sind Thermodesorptionsspektroskopie (TDS), Auger Elektronen Spektroskopie (AES) und niederenergetische Elektronenbeugung (LEED) zu nennen. Zink wurde durch Verdampfung aus einer Knudsenzelle auf die Oberfläche aufgebracht wobei sich die aufgedampfte Zinkmenge anhand eines Schwingquarzes bestimmen lässt. Zusätzlich zur "normalen" Pd(111) Probe fand auch ein Pd(111) Kristall als Teil einer Permeationsquelle Verwendung, was der Untersuchung von Winkelverteilungen auf Oberflächen dient.

Bei tiefen Temperaturen (150 K) wächst Zink in Form einer epitaktischen Schicht auf, die bei kleinen Aufdampfmengen zunächst Inseln bildet. Mit zunehmender Oberflächentemperatur (oberhalb von 300 K) beginnt eine Pd/Zn Oberflächenlegierung mit einer  $(2 \times 1)$  Überstruktur zu entstehen. Thermische Desorption von Zinkschichten mit hohen Bedeckungen führt zu einem Tieftemperaturpeak (400 - 600 K) von Zink aus den oberen Schichten und einem weiteren Peak (oberhalb von 800 K) welcher von Zinkatomen aus den unteren, stärker gebundenen Schichten, herrührt. Um zusätzliche Informationen über die Desorptionskinetik zu erhalten, wurden die TD-Spektren anhand von simulierten Desorptionsraten gefittet und die Adsorptionsenergie wurde ermittelt.

Es wird gezeigt, dass eine dicke Zinkschicht ( $\approx 10$  ML) die Adsorption von CO und H<sub>2</sub> blockiert. Die Adsorption von Wasserstoff auf der Oberfläche der Pd/Zn Oberflächenlegierung wird durch die Zinkatome vermindert, während dies keinen Einfluss auf die Diffusion in Bereiche unterhalb der Oberfläche hat. Des Weiteren beeinflusst das in der Pd/Zn Oberflächenlegierung vorhandene Zink die Wechselwirkung von CO mit der Oberfläche, was zur Folge hat, dass die Adsorptionsenergie von CO weitaus kleiner ist als für reines Pd(111). Unterschiedliche Präparationsbedingungen der Zinkschicht führen zu Veränderungen in den CO Desorptionsspektren und es können Rückschlüsse bezüglich der Bildung der Pd/Zn Oberflächenlegierung und der Diffusion von Zink in Bereiche unterhalb der Oberfläche gezogen werden.

Außerdem kann die Zinkschicht mittels Oxidation in ZnO umgesetzt werden. Die so erhaltene ZnO-Schicht zeigt eine hexagonale Symmetrie ähnlich der (0001) Ebene der ZnO Wurtzitstruktur, was eine  $(6 \times 6)$  Überstruktur zur Folge hat. Diese ZnO-Schicht lässt sich mit CO und H<sub>2</sub> über die Bildung von CO<sub>2</sub> bzw. H<sub>2</sub>O reduzieren.

*I hereby certify that the work presented in this thesis is my own and that work performed by others is appropriately cited.*

*Ich versichere hiermit, diese Arbeit selbständig verfasst, keine anderen als die angegebenen Quellen und Hilfsmittel benutzt zu haben und mich auch sonst keiner unerlaubten Hilfsmittel bedient zu haben.*

# Contents

<b>1. Introduction</b>	<b>1</b>
<b>2. Theoretical background</b>	<b>3</b>
2.1. Gas-surface Interactions: . . . . .	3
2.2. Adsorption and Desorption . . . . .	4
2.3. Sticking and Langmuir Adsorption . . . . .	7
2.4. Dynamical Parameters of Desorbing Molecules . . . . .	10
2.5. The Angular Distribution of Desorbing Particles . . . . .	11
2.6. Temperature Programmed Desorption (TPD) . . . . .	13
2.6.1. TPD Analysis / the Redhead Concept . . . . .	14
2.7. Palladium, Zinc and the Bimetallic System Pd/Zn . . . . .	17
2.7.1. Palladium . . . . .	17
2.7.2. Zinc . . . . .	17
2.7.3. The Bimetallic System Pd/Zn . . . . .	18
2.8. The Adsorption of H <sub>2</sub> on Metal Surfaces . . . . .	19
2.9. The Adsorption of CO on Metal Surfaces . . . . .	22
<b>3. Experimental Setup</b>	<b>24</b>
3.1. Ultrahigh-Vacuum-System . . . . .	24
3.2. The Sample Holder and the Permeation Source . . . . .	27
3.2.1. The Construction of the Permeation Source . . . . .	27
3.3. The Measuring Equipment . . . . .	29
3.3.1. LEED . . . . .	30
3.3.2. AES . . . . .	31
3.3.3. QMS . . . . .	31
3.3.4. Ion Sputter gun . . . . .	32
3.3.5. The Detector Chamber . . . . .	32
3.3.6. The Zinc Evaporator . . . . .	33
3.4. Sample Cleaning . . . . .	34
3.5. Preparation of the Zinc layer . . . . .	37
3.6. Measurement of the Angular Distribution of Desorption . . . . .	38
<b>4. Zn and ZnO on Pd(111)</b>	<b>39</b>
4.1. Zn on Pd(111) . . . . .	39

4.1.1. Desorption Kinetics of Zn on Pd(111) . . . . .	43
4.2. ZnO on Pd(111) . . . . .	50
<b>5. CO on Clean and Zn Modified Pd(111)</b>	<b>52</b>
5.1. CO on Pd(111) . . . . .	52
5.2. CO on Pd(111)/Zn . . . . .	54
5.2.1. Influence of different Zn Layer Preparation Methods on the CO Adsorption . . . . .	57
5.3. CO on Pd(111)/ZnO . . . . .	65
<b>6. Adsorption and Desorption of H<sub>2</sub> on Clean and Zn Modified Pd(111)</b>	<b>69</b>
6.1. Hydrogen on Clean Pd(111) . . . . .	69
6.2. Hydrogen on Pd(111)/Zn . . . . .	71
6.3. Hydrogen on Pd(111)/ZnO . . . . .	72
<b>7. Adsorption and Desorption of Sequentially Dosed H<sub>2</sub> and CO on Pd(111)</b>	<b>74</b>
7.1. CO Followed by H <sub>2</sub> . . . . .	74
7.2. H <sub>2</sub> Followed by CO . . . . .	75
<b>8. Adsorption and Desorption of O<sub>2</sub> on Pd(111)</b>	<b>77</b>
8.1. Formation of a Palladium-Oxide . . . . .	78
<b>9. Angular Distribution of D<sub>2</sub> Desorbing from Pd(111) and Pd/Zn</b>	<b>81</b>
9.1. The Simulation Program . . . . .	82
9.2. Comparison of Simulated and Measured Results . . . . .	83
9.2.1. Angular Distribution of D <sub>2</sub> Desorbing from Pd(111) . . . . .	83
9.2.2. Angular Distribution of D <sub>2</sub> Desorbing from Pd/Zn . . . . .	83
<b>10. Summary</b>	<b>85</b>
<b>11. Bibliography</b>	<b>89</b>
<b>A. Appendix - Matlab Programme and Calculated Values</b>	<b>96</b>
A.1. Calculation of the Desorption Energy and the Coverage Using the Matlab Programme . . . . .	96
A.2. The Matlab Programme . . . . .	98

# List of Figures

2.1. Example of a Lennard-Jones potential . . . . .	4
2.2. Schematic of the potential energy curve for dissociative adsorption . .	6
2.3. Variation of the sticking probability with increasing coverage . . . . .	9
2.4. Angular dependence of the desorption coefficient . . . . .	12
2.5. Series of calculated thermal desorption spectra . . . . .	15
2.6. Crystal structures of Pd and Zn . . . . .	17
2.7. The CuAu L1 <sub>0</sub> tetragonal structure of PdZn . . . . .	18
2.8. Schematic potential energy diagram for H and H <sub>2</sub> . . . . .	19
2.9. Sticking coefficient versus translational energy . . . . .	20
2.10. Illustration of the steering effect . . . . .	21
2.11. Orbital scheme for CO bonding on a metal surface. . . . .	22
3.1. Schematic illustration of the UHV-system. . . . .	25
3.2. Cross-section of the permeation source . . . . .	27
3.3. Arrangement scheme of the measuring setup . . . . .	29
3.4. Schematic diagram of a four-grid LEED . . . . .	30
3.5. Illustration of an Auger-process . . . . .	31
3.6. Schematic image of the detector chamber . . . . .	32
3.7. Cross section of the evaporation source . . . . .	33
3.8. Cross section of the zinc can . . . . .	34
3.9. AES of the Pd(111) sample during the cleaning procedure . . . . .	35
3.10. Desorption of the zinc layer . . . . .	36
3.11. AES of Zn evaporated on Pd(111) . . . . .	37
3.12. D <sub>2</sub> signal during the translational displacement . . . . .	38
4.1. LEED patterns of the prepared Zn layers on Pd(111) . . . . .	39
4.2. STM images of Zn evaporated on Pd(111) . . . . .	40
4.3. Structure model for a p(2×1) Zn superstructure on Pd(111) . . . . .	41
4.4. STM images of Zn evaporated on Pd(111) . . . . .	42
4.5. Desorption series with increasing amounts of deposited zinc . . . . .	43
4.6. Desorption series of figure 4.5 fitted with multiple peaks . . . . .	44
4.7. Desorption series of figure 4.5 fitted with simulated desorption rates .	46
4.8. Desorption series with increasing amounts of deposited zinc . . . . .	47
4.9. Desorption series of figure 4.8 fitted with multiple peaks . . . . .	48
4.10. LEED pattern of ZnO on Pd(111) . . . . .	50

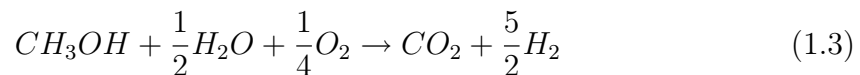
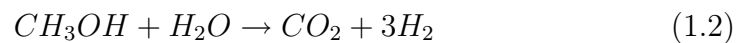
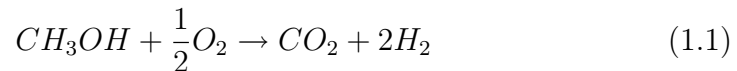
4.11. ZnO structure on Pd(111)) . . . . .	50
4.12. STM images of ZnO on Pd(111) . . . . .	51
5.1. TDS of CO adsorbed on clean Pd(111) . . . . .	52
5.2. Structure model for 0.75 ML CO on Pd(111) . . . . .	53
5.3. TDS of CO adsorbed on PdZn . . . . .	54
5.4. Desorption series of CO adsorbed on Pd/Zn . . . . .	55
5.5. TDS peak area of CO adsorbed on Pd/Zn . . . . .	56
5.6. Coverage dependence of the desorption energy of CO on Pd/Zn . . . . .	57
5.7. Desorption series of CO adsorbed on Pd/Zn prepared at 150 K . . . . .	58
5.8. TDS of CO adsorbed on Pd/Zn prepared at 300 K . . . . .	59
5.9. TDS of CO adsorbed on Pd/Zn prepared at 350 K . . . . .	60
5.10. Structure model for CO adsorption on differently prepared zinc layers . . . . .	61
5.11. Amount of adsorbed CO as a function of the zinc coverage . . . . .	62
5.12. CO TDS after annealing the zinc layer at different temperatures . . . . .	63
5.13. Change of the CO and CO <sub>2</sub> TD spectra with the CO adsorption cycles . . . . .	65
5.14. AES signal versus number of CO desorption cycles . . . . .	67
5.15. Change of the Pd/ZnO LEED pattern with CO desorption . . . . .	67
5.16. Structure model of the reduction of Pd/ZnO by CO . . . . .	68
6.1. TDS of H <sub>2</sub> adsorbed on clean Pd(111) using different exposures . . . . .	69
6.2. TDS of H <sub>2</sub> adsorbed on Pd/Zn using different exposures . . . . .	71
6.3. TD spectrum of hydrogen adsorbed on Pd/ZnO . . . . .	72
6.4. Change of the Pd/ZnO LEED pattern with H <sub>2</sub> desorption . . . . .	73
6.5. AES signal versus number of H <sub>2</sub> desorption cycles . . . . .	73
7.1. TDS of adsorbed H <sub>2</sub> after preadsorption of CO on clean Pd(111) . . . . .	74
7.2. TDS of adsorbed CO after preadsorption of H <sub>2</sub> on clean Pd(111) . . . . .	75
8.1. TDS of O <sub>2</sub> adsorbed on clean Pd(111) . . . . .	77
8.2. p(2×2) superstructure of oxygen adsorbed on Pd(111) . . . . .	78
8.3. LEED patterns of the PdO superstructure on Pd(111) . . . . .	79
8.4. LEED schematics of the PdO superstructure . . . . .	79
9.1. Sample arrangement during the angular distribution measurements . . . . .	81
9.2. Angular distribution of Deuterium desorbing from clean Pd(111) . . . . .	83
9.3. Angular distribution of Deuterium desorbing from clean Pd/Zn . . . . .	84

# 1. Introduction

The main task of surface science is the investigation of interactions between atoms or molecules with a solid surface including effects of surface layers and structures, which is closely correlated with the growing field of nanoscience. For example the catalytic effect of surfaces can strongly depend on the special chemical composition and on the structure of the surface.

This comes into play due to the fact that global energy shortage and the reduction of carbon dioxide have raised the issue of fuel cells and hydrogen vehicles. But since current technologies for on board storage of hydrogen gas are still not economically attractive, new concepts involve small scale steam reforming to provide hydrogen to fuel cells. The basic idea is to use a methanol tank and a steam reforming unit to replace the bulky pressurized hydrogen tanks which may also mitigate distribution problems (see [1]).

Hence hydrogen is provided by oxidative methanol reforming:



This involves the combination of an exothermic partial oxidation (equation 1.1:  $dH_0 = -154,8kJ/mol$ ) with an endothermic steam reforming (equation 1.2:  $dH_0 = +231kJ/mol$ ) of methanol in such a ratio that the overall reaction (equation 1.3) is thermal neutral or at least modestly exothermic.

Nowadays commercially used catalysts for oxidative methanol reforming are based on copper and zinc which are high active and selective catalysts but their drawback is the rapid deactivation of the catalyst by sintering of the metal at temperatures above 300°C. This fact obstructs the application for on-board hydrogen production (see [2]).

Thus new concepts involve Pd/ZnO catalysts. Pure palladium itself has a poor selectivity for steam reforming of methanol resulting in an predominant decomposition to hydrogen and carbon monoxide. But since carbon monoxide is a poison to the electrocatalyst at the fuel cell anode this would make it necessary to include complex CO removal systems.

However, the catalytic properties of palladium can be greatly improved by supporting ZnO which causes an enhancement of the selectivity in methanol steam reforming. Hence Pd/ZnO catalysts show a high selectivity towards hydrogen production as well as a higher melting point compared to copper giving rise to a better thermal stability at higher reaction temperatures. PdZn catalysts show superior long term thermal stability under real catalytic conditions compared to Cu/ZnO catalysts (see [3], [4], [5]).

Due to the rising importance and interest in this system, the aim of this work is to increase the knowledge about the system Pd/Zn itself and about the interaction of PdZn and PdZnO surfaces with different gases.

## 2. Theoretical background

*In this chapter, the theoretical background is explained: the physics of adsorption and desorption, the sticking-coefficient, the angular distribution of desorbing particles and the theoretical concept of temperature programmed desorption. The used sample is a palladium single crystal, which is modified by Zn and ZnO coverages. Several properties of palladium, zinc and their compounds are mentioned.*

### 2.1. Gas-surface Interactions:

When a molecule or an atom impinges on a surface, several possible reactions may occur [6]:

#### **Elastic scattering:**

The particle is scattered without any energy exchange between the particle and the surface. Thus the particle is reflected back without any possibility to stick and the energy of the particle and the surface is conserved. This process includes diffraction and since the de Broglie wavelength of thermal atoms and molecules is within the realm of atomic distances in solids, diffraction patterns can be observed.

#### **Inelastic scattering:**

An energy transfer between the impinging particle and the surface by phonon or electronic processes occurs. The particle may turn energy into the surface or receive energy from the surface. One distinguishes between direct processes, whereupon the whole energy is transferred at a single collision event and indirect processes with multiple collisions. Anyway, the energy-loss of the particle is too low to allow it to stick on the surface.

#### **Trapping and Sticking:**

If the impinging particle loses enough of its translational energy perpendicular to the surface, it will not be able to leave the attractive surface potential. For a surface temperature greater than 0 K the particle is then oscillating with respect to the surface and can leave the surface again by absorbing energy from the solid. Thus the molecule is trapped by the surface for some time.

If this residence time is big compared to the oscillation period of the particle in the potential well, the particle sticks on the surface, it is adsorbed. The adsorption process may then be treated independently of the inverse effect, the desorption process.

## 2.2. Adsorption and Desorption

Adsorption takes place when an attractive interaction between a particle and a surface is strong enough to overcome the disordering effect of thermal motion. Usually one distinguishes the interaction forces leading to adsorption with respect to their physical origin (see [7], [8], [9] [10]).

- **Physisorption:** When the attractive interaction is essentially the result of Van-der-Waals forces physisorption takes place. Van-der-Waals forces originate in the ground state fluctuations of the electronic charge of an atom, which generates a dynamic dipole moment. The electric field emerging from this fluctuating dipole gives rise to an induced dipole moment in a second atom at a distance  $r$ . The energy of the induced dipole is negative and thus leads to an attractive interaction proportional to  $r^{-6}$ .

At smaller distances, the Pauli repulsion between closed shells arises and balances the Van-der-Waals interaction. Since it is proportional to the overlap of the wave functions the Pauli-repulsion increases exponentially with decreasing distance and is usually approximated by an  $r^{-12}$  dependence.

Thus for a physisorption system the interaction between the adsorbate and the atoms of the solid surface may be approximated by the so called Lennard-Jones potential:

$$V(r) = V_0 \left\{ \left( \frac{r_0}{r} \right)^{12} - 2 \left( \frac{r_0}{r} \right)^6 \right\} \quad (2.1)$$

whereas  $-V_0$  is the potential at the equilibrium distance  $r_0$ . Figure 2.1 shows the one-dimensional potential energy curve ( $V(r)$  versus  $r$ ) for a molecular adsorbate approaching a surface along the perpendicular distance  $r$

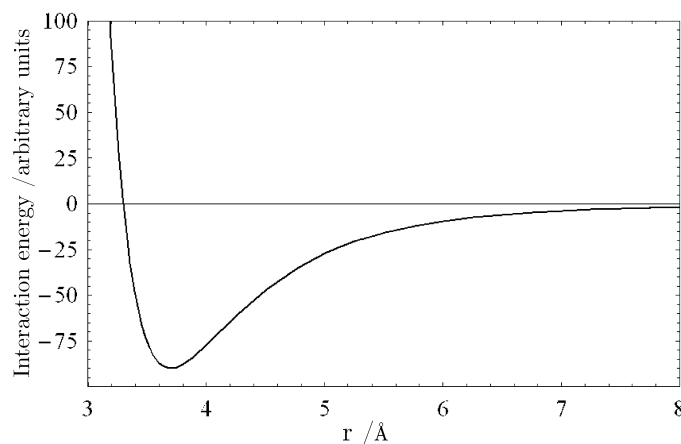


**Figure 2.1.:** Example of a Lennard-Jones potential

The energy zero is chosen such that  $V(r)=0$  for  $r = \infty$ . At the equilibrium distance  $r_0$ , where the potential energy curve exhibits a minimum, the adsorption energy  $V_0$  is gained. The deeper the potential well the stronger is the interaction and the equilibrium position  $r_0$  increases with decreasing surface-atom bond strength.

In principle the situation at a surface is much more complex since an adatom is usually not coupled to a single surface atom, but rather to a whole array of atoms. Thus for a physisorption system the Van-der-Waals interaction is with all atoms of the solid whereas for the repulsive part only the nearest neighbours matter. Therefore the interaction potential is the sum over all two-body potentials (equation 2.1).

- **Chemisorption:** As the name suggests chemisorption implies the formation of a chemical bond. It occurs when the overlap between the molecular orbitals of the adsorbed particle and the surface atoms permit the formation of chemical bonds.

Van-der-Waals forces dominate at large distance from the surface and exist for all molecules approaching a surface. In this range, the surface exhibits delocalized electronic bands, whereas the adatom has still discrete atomic orbitals of sharp energies as long as it is rather far away from the surface. As the distance  $r$  gets smaller the orbitals of the adatom also get broader and shift, and certain degeneracies are lifted, owing to the reduction of overall symmetry caused by the presence of the surface. This gives rise to a direct intermingling of the adsorbate and substrate charge densities, leading to the build-up of a chemical bond.

The equilibrium is reached when the adsorbed particle resides at the bottom of the potential well, whose depth reflects the energy of the respective bond, if the adsorption is molecular and non-activated. A good example of a typical chemisorption case is carbon monoxide on transition metal surfaces. A more detailed model to describe this interaction mechanism will be given later on in this chapter.

**Dissociative Adsorption:** Apart from the already mentioned molecular (associative) adsorption with the whole molecule bonding to the surface, molecules such as  $H_2$  and  $O_2$  typically dissociate, so that bonding occurs with individual atoms (see [7], [8], [9] [11]). Therefore the process is called dissociative adsorption. Figure 2.2 represents the potential energy curve of this process.

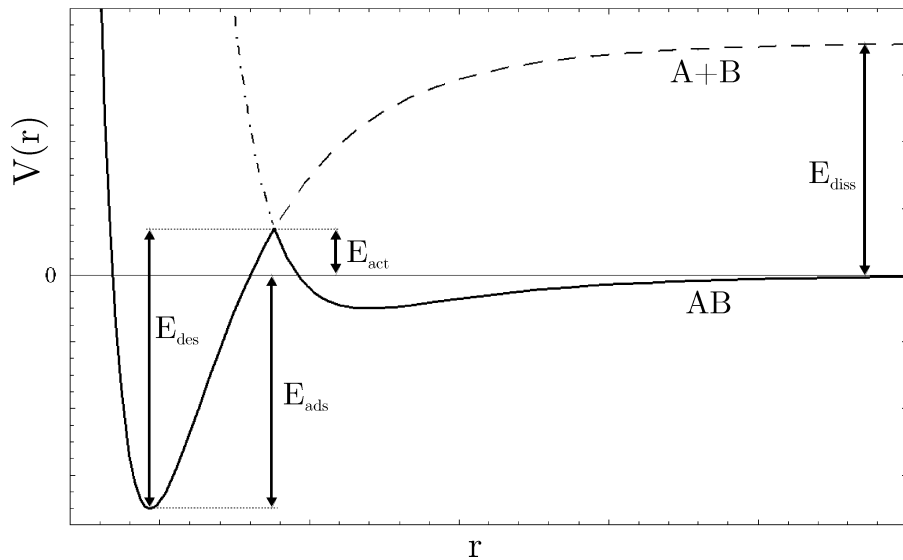


**Figure 2.2.:** Schematic of the potential energy curve for dissociative adsorption: The case of activated chemisorption with an activation barrier  $E_{\text{act}}$ .  $E_{\text{ads}}$  is the binding energy in the chemisorbed state,  $E_{\text{des}}$  the barrier for desorption from the chemisorbed state and  $E_{\text{diss}}$  the dissociation energy for the molecule in the gas phase

As the molecule (AB) approaches the surface,  $V(r)$  exhibits the familiar physisorption minimum (dash-dot curve). Now split the molecule into its atomic constituents A+B (dashed curve). Far away from the surface, the separated atom energy lies above the energy of the bound molecule which is taken as zero. The difference of these energies is the dissociation energy  $E_{\text{diss}}$ , which is the amount of energy that has to be put into the system in order to cause dissociation of the molecule. However this holds only for large distances where the molecule can be treated as being isolated from the surface, but at closer distances,  $V(r)$  can develop a deep minimum if the individual atoms A+B form strong chemisorptive bonds to the surface (dashed curve).

The energy of the true adsorbate complex evolves along the path of the minimum energy (solid curves). Thus the molecule initially approaches the surface along the physisorption curve. If it has sufficient energy it may pass straight into the chemisorption well or, alternatively, it may first undergo transient physisorption. From this state the molecule can either desorb back as a molecule into the gas phase or cross over the barrier into the dissociated, chemisorptive state. In the latter case, one says that the physisorbed state is a precursor to the chemisorbed state.

The characteristics of this type of dissociative adsorption depends on the details of the competing potential energy curves and especially on their crossing points. For example, the molecule spontaneously dissociates if the curve crossing occurs below the zero point of energy.

By contrast, if the curve crossing occurs above the energy zero (see 2.2), molecular

physisorption results at low temperature and the activation energy  $E_{act}$  has to be put into the system to allow the molecule to undergo dissociative chemisorption. The dissociated species ultimately appears at higher temperatures because thermal activation carries the system into the lowest energy state over the potential energy barrier. From the diagram one can see that:

$$E_{act} = E_{des} - E_{ads} \quad (2.2)$$

The above mentioned distinction between physisorption and chemisorption is sometimes also according to the adsorption energy, with physisorption denoting the realm of lower adsorption energies. However this classification is not very distinct and a weak chemical interaction is always present.

Furthermore, it should be noted that in fact the one-dimensional model for dissociative adsorption oversimplifies the problem. The molecule has internal degrees of freedom that is vibrational and rotational eigenstates. In addition the molecule may approach the surface from different angles and strike the surface at a different position with respect to the surface structure. Thus the one-dimensional model has to be further improved to include additional coordinates corresponding to each degree of freedom (see [12], [13], [14], [15]).

### 2.3. Sticking and Langmuir Adsorption

Sticking is not only determined by the energy transfer of the impinging particle but also by the ability of the surface to form bonds. In literature sticking is usually discussed by means of a sticking probability,  $S(\theta)$  which is a function of the surface coverage  $\theta$  [16]. Thus the sticking coefficient is the probability of particles to adsorb on a surface which is defined by the ratio of the number of adsorbing particles  $N_{ads}$  and the number of impinging particles  $N_{imp}$ :

$$S(\theta) = \frac{N_{ads}}{N_{imp}} \quad (2.3)$$

The rate of adsorption  $r_{ads}$  is then related to the sticking probability by

$$r_{ads} = S(\theta) \cdot I \quad (2.4)$$

where  $I$  is the total flux of impinging molecules on the surface in molecules/cm<sup>2</sup> · s. Assuming molecules that are impinging isotropically on the surface from the gas phase, the flux is calculated according to:

$$I = \frac{dN_i}{dt} = \frac{p}{\sqrt{2\pi m_{Mol} k_B T_{Gas}}} \quad (2.5)$$

with the molecular weight  $m_{Mol}$ , the temperature  $T_{Gas}$ , the pressure  $p$  and  $k_B$ , Boltzmann's constant. The total number of impinging gas molecules can then be

determined by integration of equation 2.5.

In the experiment the surface is usually exposed to a certain gas pressure for a given time. Assuming that  $T_{Gas}$  is the room temperature ( $\approx 300$  K), the number of impinging particles per  $\text{cm}^2$  of the surface is then given in terms of the exposure  $EX$  in Langmuir ( $1 \text{ L} = 10^{-6} \text{ Torr}$ ) by:

$$N \approx EX[L] \cdot \frac{2.023 \cdot 10^{15}}{\sqrt{m_{Mol}}} \quad (2.6)$$

To determine the coverage dependent sticking coefficient experimentally one usually measures so-called uptake curves. These curves are plots of the amount of adsorbate versus the gas exposure. To evaluate the amount of adsorbate  $A_{ads}$ , the adsorbed species is desorbed using TPD and the peak area of the according mass signal in the spectra is then calculated. Generally, a rapid initial uptake of gas is observed, followed by a continually slowed-down uptake the closer the actual coverage comes to the saturation value.

By deriving the uptake curve, the sticking coefficient is calculated as:

$$S(\theta) = \frac{dA_{ads}}{d\epsilon} \quad \text{with} \quad \epsilon = \int \frac{p}{\sqrt{2\pi m_{Mol} k_B T_{Gas}}} \cdot dt \quad (2.7)$$

Since the sticking coefficient represents a probability it can take per definition values between 0 and 1. The absolute determination of sticking turns out to be quite intricate in the experiment, however there are some feasible methods described by [17], which allow an accurate determination of  $S(\theta)$ .

Starting with a clean surface without any adsorbed particles on it the sticking coefficient is referred to be the initial sticking coefficient. When the number of particles on the sample surface increases, the sticking coefficient usually decreases. At a saturation coverage  $\theta_{sat}$  the sticking coefficient approaches to zero.

A simple model, to calculate the coverage dependence of the sticking coefficient is the so called Langmuir adsorption model [16]. Langmuir assumed that all adsorption sites are equivalent, only one molecule can reside in each adsorption site and that the adsorption is limited by the monolayer coverage. Thus an incident particle sticks on an empty adsorption site with a certain probability  $S_0$ , and it is scattered on an occupied adsorption place with the probability one. The sticking probability  $S(\theta)$  becomes:

$$S(\theta) = S(0) \cdot (1 - \theta)^n \quad (2.8)$$

where  $n$  is the number of sites that are needed to hold the adsorbate. For molecular adsorption  $n = 1$  holds and for dissociative adsorption  $n = 2$  holds if the dissociative products are mobile. The adsorption rate (equation 2.4) becomes:

$$r_{ads} = S(0) \cdot I \cdot (1 - \theta)^n \quad (2.9)$$

In figure 2.3  $S(\theta)/S(0)$  versus the coverage  $\theta$  is plotted. Curve (a) and (b) show the cases of  $n = 1$  and  $n = 2$  respectively.

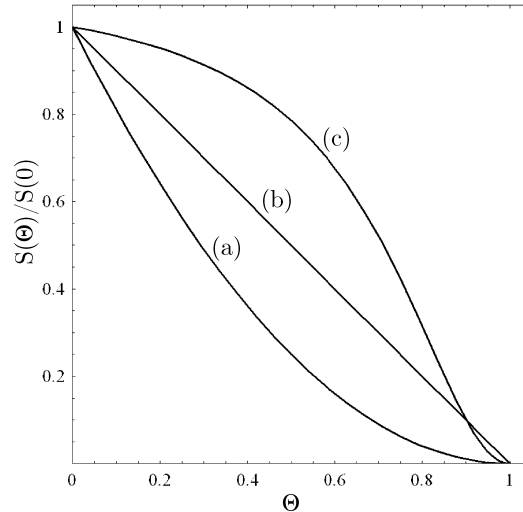


**Figure 2.3.:** Variation of the sticking probability with increasing coverage: Molecular adsorption with  $n = 1$  (b), dissociative adsorption with  $n = 2$  (a) and precursor mediated adsorption with  $n = 2$  and  $K = 10$  (c).

Equation 2.8 is a good approximation, but it does not describe precursor mediated adsorption. In this case the molecule which has been trapped in the precursor state can either desorb back into the gas phase or go into the chemisorbed state. By introducing the rate constant  $k_a$  for adsorption from the precursor state into the final chemisorbed state and the rate constant  $k_d$  for desorption from the precursor state, the sticking coefficient can be expressed as [16]:

$$S(\theta) = S_p \frac{(1 + K)(1 - \theta)^n}{1 + K(1 - \theta)^n} \quad (2.10)$$

with  $K = k_a/k_d$ . Instead of  $S_0$ , the trapping probability  $S_p$  from the gas phase into the precursor state is introduced. Curve (c) in figure 2.3 displays this case for  $n = 2$  and  $K = 10$ .

Equation 2.10 holds for a precursor-mediated adsorption of non-interacting adsorbates. For a low desorption rate from the precursor state ( $K \rightarrow \infty$ )  $S$  approaches 1 whereas in the case of a high desorption rate from the precursor state ( $K \rightarrow 0$ )  $S$  approaches the Langmuir type kinetics (equation 2.8).

However the variance of the sticking coefficient may be different from these simple curves in the experiment. Several reasons give rise to deviations: There can be more than one possible adsorption site for a certain molecule and the adsorbate may possess a certain mobility. In addition defect sites on the surface can act as active centers for adsorption [11].

## 2.4. Dynamical Parameters of Desorbing Molecules

For a gas in equilibrium at a temperature  $T$  and without the influence of external fields the velocities are characterized by a Maxwell-Boltzmann distribution. Due to homogeneity the number density is independent of the coordinates:  $n(x, y, z) = n$ . The number of molecules per unit volume, having a velocity in the infinitesimal element  $(dv_x, dv_y, dv_z)$  about  $\vec{v} = (v_x, v_y, v_z)$  is then given by [18]:

$$d^3n = n \left( \frac{m}{2\pi k_B T} \right)^{3/2} \exp \left[ -\frac{m(v_x^2 + v_y^2 + v_z^2)}{2k_B T} \right] dv_x dv_y dv_z \quad (2.11)$$

with the Boltzmann constant  $k_B$  and  $m$ , the mass of the molecules. The symmetry with respect to  $v_x, v_y, v_z$  emphasizes the isotropy of the velocity distribution. Based on this isotropy it is convenient to introduce spherical coordinates in equation 2.11. By integrating over the polar angle  $\vartheta$  and the azimuth angle  $\varphi$ , one gets the number of molecules with speeds between  $v$  and  $v + dv$  in the unit volume:

$$dn = 4\pi n \left( \frac{m}{2\pi k_B T} \right)^{3/2} \exp \left[ -\frac{mv^2}{2k_B T} \right] v^2 dv \quad (2.12)$$

In surface science one is usually not interested in the velocity distribution of a volume but in the number of molecules impinging on a surface during a time interval. Thus imagine to build a cylinder upon a surface area  $dA$  with the cylinder height equal to the velocity  $v$ . Then the height of the cylinder is exactly the distance which a particle with the velocity  $v$  passes per unit time. The number of particles in the cylinder is given by equation 2.11. Again it makes sense to use spherical coordinates with the zenith taken perpendicular to the surface area.

But for particles which are impinging on the surface with the angle  $\vartheta$  the area is reduced from  $dA$  to  $dA \cdot \cos \vartheta$  and the cylindrical volume becomes  $dA \cdot \cos \vartheta \cdot v$  [19]. Thus the number of particles impinging at angles between  $\vartheta$  and  $\vartheta + d\vartheta$  per unit angle with the velocity between  $v$  and  $v + dv$  and per unit time is given by:

$$dF = dn \cdot v \cdot \cos \vartheta = n \left( \frac{m}{2\pi k_B T} \right)^{3/2} \exp \left[ -\frac{mv^2}{2k_B T} \right] v^3 \cos \vartheta dv \quad (2.13)$$

As already mentioned, in a system in equilibrium, the molecules leaving the surface have an identical distribution to the molecules impinging on the surface [20]. Thus the molecules leaving a surface at equilibrium are also described by equation 2.13. If the sticking probability  $S = 1$ , all impinging molecules adsorb and all leaving molecules are desorbing ones.

Then equation 2.13 applies at equilibrium also for the desorbing molecules. Since in many cases  $S$  might be very near to unity in the significant range of  $v$  and  $\vartheta$ , the equation applies within a small experimental error.

## 2.5. The Angular Distribution of Desorbing Particles

By integrating equation 2.13 over the velocity  $v$  one obtains the total flux leaving a surface area  $dA$  into a solid angle direction  $\vartheta, \varphi$ :

$$F(\vartheta, \varphi) \cdot dA = \frac{n}{4\pi} \left( \frac{8k_B T}{\pi m} \right)^{1/2} \cos \vartheta \cdot dA \quad (2.14)$$

Thus molecules leaving the surface at equilibrium have a distribution proportional to  $\cos \vartheta$  [21].

If we recall again the sticking probability which was introduced in section 2.3, it should be mentioned that this quantity is in fact also affected by other parameters such as the energy and the angle of the impinging particles. We want to concentrate on the angular dependence of the sticking coefficient in the following.

First experiments were done by Van Willigen (see [22], [23]) who showed that hydrogen desorbing from Fe, Pd and Ni exhibited strongly forwarded angular flux distributions: The concentration of desorbed molecules was higher in the vicinity of the surface normal.

These results may be interpreted in terms of a one-dimensional barrier model: A Maxwellian hitting a one-dimensional barrier will be attenuated in the low energy end of the spectrum. The velocity component normal to the barrier ( $v \cdot \cos \vartheta$ ) can only be used to overcome the barrier when the “normal translational energy”  $E \cos^2 \vartheta$  is greater than the barrier height. With increasing angle  $\vartheta$ , fewer and fewer particles out of the Maxwellian are able to cross the barrier.

Thus with increasing barrier height the desorption flux  $D(\vartheta)$  becomes more and more concentrated around the surface normal. The angular dependence of the desorption flux is then approximated by:

$$D(\vartheta) = D(\vartheta = 0) \cdot \cos^n \vartheta \quad (2.15)$$

In order to get information about the angular dependence of the sticking probability we need to define the concept of detailed balance [24]. What one does in the experiment is to get as close as possible to the dynamic equilibrium, whereas the rate of adsorption equals the rate of desorption:  $r_{\text{ads}} = r_{\text{des}}$ .

According to the concept of microscopic reversibility, there exists an identical reverse path to each forward path which is achieved by reversing the time. Detailed balance demands that in thermal equilibrium each forward path occurs with the same probability as the corresponding backward path.

According to equation 2.4 the adsorption rate is given by the sticking coefficient  $S$  times the number of impinging particles. Considering the angular distribution of the

impinging particles the  $\cos \vartheta$  term has to be introduced and the concept of detailed balance becomes:

$$S(\vartheta) \cdot \cos \vartheta = D(\vartheta) \quad (2.16)$$

By inserting equation 2.15 one gets:

$$S(\vartheta) = S(\vartheta = 0) \cdot \cos^{n-1} \vartheta \quad (2.17)$$

Now it is possible to determine the parameter  $n$  of the angular distribution according to 2.15. First the angular distribution of desorbing molecules from a surface is determined experimentally. Then the experimental data is fitted by a  $\cos^n \vartheta$  distribution whereas  $n$  is varied until the simulated curve matches the experimental data optimally (see [25], [26], [27]).

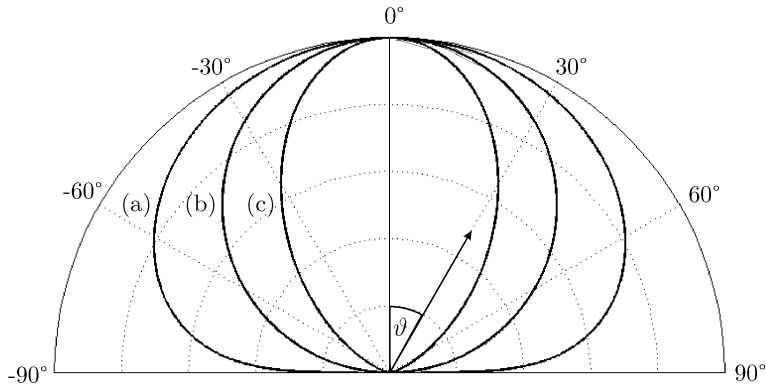


**Figure 2.4.:** Angular dependence of the desorption coefficient according to  $\cos^n \vartheta$  with  $n = 0.3$  (a),  $n = 1$  (b) and  $n = 3$  (c).

Figure 2.4 displays a polar plot of the  $\cos^n \vartheta$  distribution with various  $\vartheta$ .

- For  $n = 1$  the angular dependence of the desorption coefficient obeys a cosine. According to equation 2.17, the sticking coefficient is then independent of the angle in this case.
- For  $n > 1$  the angular distribution of the desorption coefficient is sharper than the normal cosine, giving rise to a higher concentration of desorbed molecules in the vicinity of the surface normal. The sticking coefficient obeys a  $\cos^{n-1} \vartheta$  distribution. This corresponds to an activated adsorption process.
- For  $n < 1$  the angular dependence of the desorption and sticking coefficient is less pronounced and somewhat broader than the cosine distribution which describes a precursor mediated adsorption

## 2.6. Temperature Programmed Desorption (TPD)

The opposite phenomenon of adsorption is desorption and thermal desorption spectroscopy is one of the most frequently used methods to gather information on the energetics and kinetics of adsorbed particles (see [27], [28], [29], [30], [16], [8]).

As explained in the preceding sections, in the adsorbed state and in thermal equilibrium the trapped particle resides at the bottom of the potential well whereat the depth of this well corresponds to the adsorption energy  $E_{\text{ads}}$ . It is either physically or chemically adsorbed to the solid surface. In order to desorb it from the surface, one has to supply it thermally or electronically with the energy required to transfer it to the gas phase.

Looking at the desorption process, the energy necessary to move the adsorbed particle away from the surface is called energy of desorption  $E_{\text{des}}$ . If there is no activation barrier,  $E_{\text{des}}$  has the same value as the adsorption energy  $E_{\text{ads}}$ , but in case of an activation barrier (figure 2.2) equation 2.2 holds. Thus the activation barrier has to be additionally overcome, and the desorbing particle possesses more energy than it had when it was in thermal equilibrium with the surface.

The procedure to obtain a spectrum of the desorbing particles is the following: After adsorption of one or more molecular species onto the sample surface at low temperature, the adsorbate covered surface is heated. This is usually done, following a linear temperature ramp and the desorbing particles are monitored with a mass spectrometer. The obtained data consists of the intensity variation of each recorded mass fragment as a function of the sample temperature.

This so called TPD spectra allow several conclusions (see [27], [28], [31], [16]):

- The area under a peak is proportional to the amount originally adsorbed and thus proportional to the surface coverage.
- The peak profile and the coverage dependence of the desorption characteristics include information about the kinetics of desorption and thus on the state of aggregation of the adsorbed species, that is molecular versus dissociative.
- The temperature at which the peak maximum occurs is related to the enthalpy of adsorption, that is to the strength of binding to the surface.

### 2.6.1. TPD Analysis / the Redhead Concept

The kinetic approach to thermal desorption spectra is based on the principle of microscopic reversibility, demanding that a reaction passes through exactly the same states irrespective of whether it proceeds forward or backward. Therefore adsorption and desorption can be described by the same set of rate equations. The desorption is then written in terms of a desorption rate  $r_{\text{des}}$  which is the number of particles desorbing from the unit surface area per unit time:  $r_{\text{des}} = -\frac{d\theta}{dt}$ .

Under the assumption that all adsorbed atoms or molecules occupy identical sites and do not interact with each other, the desorption rate is expressed by the Polanyi-Wigner equation:

$$r_{\text{des}} = -\frac{d\theta}{dt} = k_n(\theta) \cdot \theta^n = \nu_n(\theta) \cdot \exp\left(-\frac{E_{\text{des}}(\theta)}{RT}\right) \cdot \theta^n \quad (2.18)$$

with the activation energy  $E_{\text{des}}$  for desorption, the order  $n$  of desorption kinetics, the surface temperature  $T$  and the coverage  $\theta$ . The preexponential factor  $\nu$  describes an empirical relationship between the temperature and  $r_{\text{des}}$ . The model is much easier to handle if one assumes that the desorption energy and the preexponential factor  $\nu$  are independent of the coverage. For a first order reaction with  $n = 1$ ,  $\nu$  is then given in units of  $\text{s}^{-1}$ ; this is why it is often referred to as frequency factor in literature.

Interpretation of the thermal desorption spectra is most commonly performed by the use of this Polanyi-Wigner equation (see [32]): During a TDS experiment one linearly increases the temperature  $T$  of the sample with the heating rate  $\beta$  ( $T = T_0 + \beta \cdot dt$ ) and simultaneously measures the rate  $r_{\text{des}}$ . This method is called Temperature-Programmed Desorption (TPD), because the temperature is monotonically increased. With a given initial temperature  $T_0$  and heating rate  $\beta$  equation 2.18 becomes:

$$\frac{d\theta}{dT} = \frac{\nu_n}{\beta} \cdot \theta^n \cdot \exp\left(-\frac{E_{\text{des}}}{RT}\right) \quad (2.19)$$

The exponential term in the equation increases with increasing temperature but at the same time the desorption rate diminishes the residual coverage. Thus, if the desorption rate is plotted as function of the sample temperature one usually observes a peak in the diagram.

Depending on the order  $n$  of the desorption process, different shapes of thermal desorption spectra are obtained. Figure 2.5 shows series of thermal desorption spectra for different initial adsorbate coverages and different  $n$ .

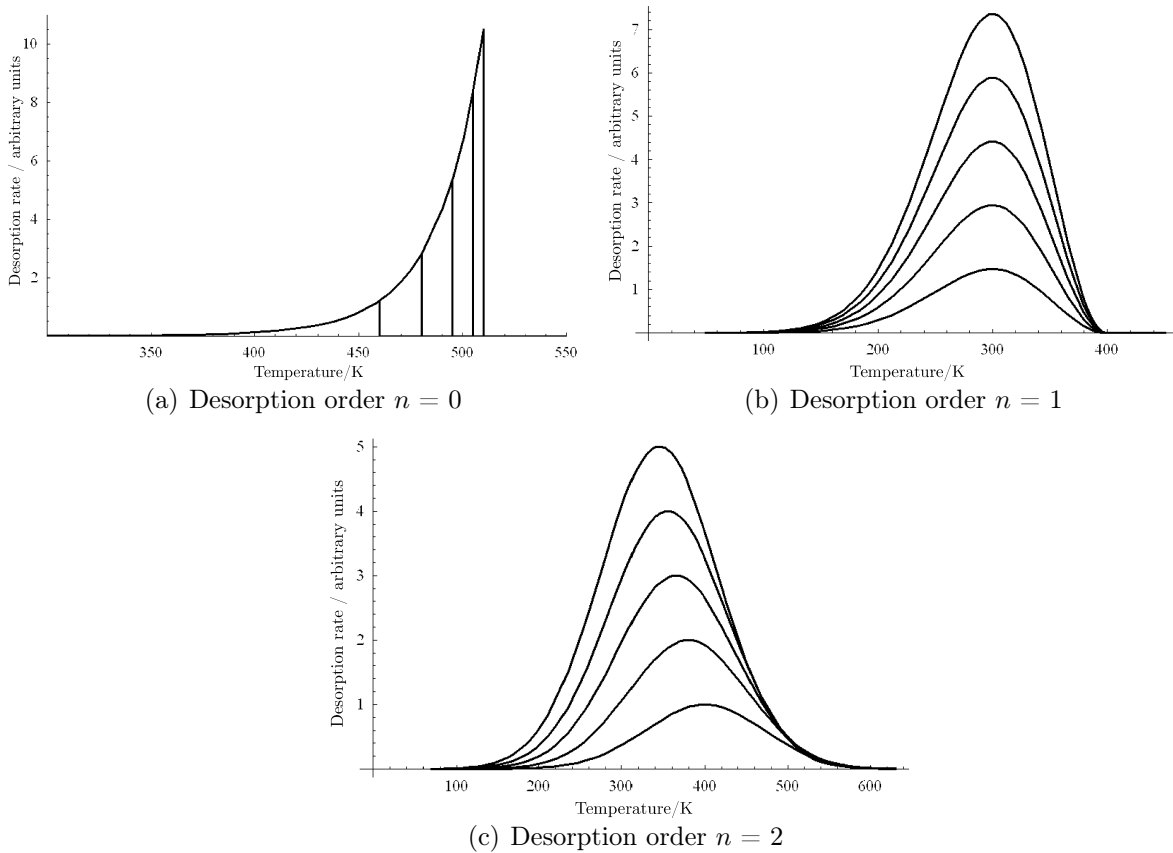


**Figure 2.5.:** Series of calculated thermal desorption spectra with increasing coverage  $\theta$  for the desorption order  $n = 0, 1, 2$ .

- In zero order kinetics ( $n = 0$ ), the desorption rate does not depend on the coverage. In equation 2.19 only the constant  $\nu$  and the exponential temperature-dependent factor remain. Thus the desorption rate increases exponentially with  $T$ . There is a rapid drop in the spectrum after all molecules have desorbed and the temperature of the peak maximum moves to higher  $T$  with increasing coverage  $\theta$ . Zero-order kinetics takes place at the desorption of a homogeneous multilayer film.
- In first-order kinetics ( $n = 1$ ), the desorption rate is proportional to the coverage  $\theta$ . The spectra feature a characteristic asymmetric peak shape but the temperature at which the peak maximum occurs, stays the same with increasing coverage. In this case the preexponential factor  $\nu$  is in units of the frequency  $s^{-1}$  and its order is roughly of the atomic frequency of the crystal lattice ( $\approx 10^{13}s^{-1}$ ). The desorption process corresponds to the simplest case, when single atoms desorb directly and independently from their sites.
- In second-order kinetics ( $n = 2$ ) the desorption rate is proportional to  $\theta^2$ . The TDS are then characterized by a nearly symmetric peak shape. The

peak maximum moves with increasing coverage towards lower temperatures. This kinetics occurs in the case of associative molecular desorption, where the desorbing molecule originates from two atoms residing initially at separate sites.

Despite the mentioned exponents, it may be necessary to use other exponents to describe complicated kinetic processes. Hence in reality, kinetics might result in exponents of a higher order and even fractional ones. Nevertheless we want to concentrate on the analysis of zero and first order desorption.

In the case of zero order kinetics a single TD spectrum contains all the information. The desorption rate does not depend on the coverage and by taking the logarithm of equation 2.19 with  $n = 0$  one gets:

$$\ln \left( \left| \frac{d\theta}{dT} \right| \right) = -\frac{E_{\text{des}}}{RT} + \ln \left( \frac{\nu_0}{\beta} \right) \quad (2.20)$$

When plotting  $\ln(d\theta/dT)$  versus  $1/T$  one obtains a straight line whereby  $E_{\text{des}}/R$  corresponds to the slope and  $E_{\text{des}}$  can be evaluated. In addition the y-intercept may be used to evaluate the  $\nu_0$

For first order desorption it is possible to determine the desorption energy  $E_{\text{des}}$  with experimentally obtained TPD spectra according to a concept which was introduced by Redhead [33]. Therefore he assumed that the activation parameters are independent of the coverage and started with equation 2.19 in the case of  $n = 1$ .

For the temperature at which the peak exhibits its maximum  $T = T_m$  the condition  $\frac{dr_{\text{des}}}{dT}|_{T_m} = 0$  holds. Then, according to  $r_{\text{des}} = -\frac{d\theta}{dt} = -\beta \frac{d\theta}{dT}$ ,  $\frac{d^2\theta}{dT^2}|_{T_m} = 0$  has to be fulfilled. Thus one gets:

$$\frac{E_{\text{des}}}{RT_m^2} = \frac{\nu_1}{\beta} \cdot \exp \left( \frac{E_{\text{des}}}{RT_m} \right)$$

Taking the logarithm and solving for  $E_{\text{des}}$  gives rise to:

$$E_{\text{des}} = R \cdot T_m \left[ \ln \left( \frac{\nu \cdot T_m}{\beta} \right) - \ln \left( \frac{E_{\text{des}}}{RT_m} \right) \right] \quad (2.21)$$

The second part in the brackets is small relative to the first one and is estimated as  $\ln \left( \frac{E_{\text{des}}}{RT_m} \right) \approx 3.64$ . The introduced error due to this estimate is less than 1.5% for  $10^8 < \nu/\beta < 10^{13} \text{K}^{-1}$ .

Hence if an approximate value of  $\nu$  is known the activation energy can be extracted from a single desorption spectrum by determining the temperature of the peak maximum  $T_m$ .

## 2.7. Palladium, Zinc and the Bimetallic System Pd/Zn

### 2.7.1. Palladium

The used sample is a palladium single crystal. Palladium is a rare silver-white transition metal of the platinum group with the ordinal number 46. The electron configuration is  $[Ar]3d^{10}4s^24p^64d^{10}$ , characterized by a fully filled  $4d^{10}$  subshell. Palladium is the most reactive element of the platinum group. Its melting point is 1828 K, its boiling point 3236 K [34].

It does not react with oxygen at room temperature, thus it does not tarnish in air. Palladium has a great affinity for hydrogen that is, it is able to absorb 900 times its own value of the gas. Furthermore, it is a very good catalyst that speeds up hydrogenation and dehydrogenation reactions, therefore it is mainly used as a primary component in autocatalysts. It may also be used as permeation source since hydrogen diffuses quickly through thin palladium pieces at high temperatures.

Palladium crystallizes face centered cubic (figure 2.6(a)) whereas the length  $a$  of the unit cell is 3.880 Å [35]. The used palladium sample exhibits a (111) surface plane which is characterized by a hexagonal structure with a hexagon side length of 2.745 Å (figure 2.6(b))

### 2.7.2. Zinc

Zinc is a moderately-reactive bluish-white metal with the ordinal number 30. Its electron configuration is  $[Ar]3d^{10}4s^2$ , its melting point is 692.68 K and its boiling point is 1180 K. The most stable isotopes of zinc are  $^{64}\text{Zn}$ ,  $^{66}\text{Zn}$  and  $^{68}\text{Zn}$  with a natural abundance of 49%, 28% and 19% respectively.

The crystal structure of Zn is hexagonal close packed (see figure 2.6(c)) with  $a = 2.665$  Å and  $c = 4.947$  Å. Thus the lattice mismatch between the hexagonal Zn(0001) surface plane and the Pd(111) surface plane is just about 3%.

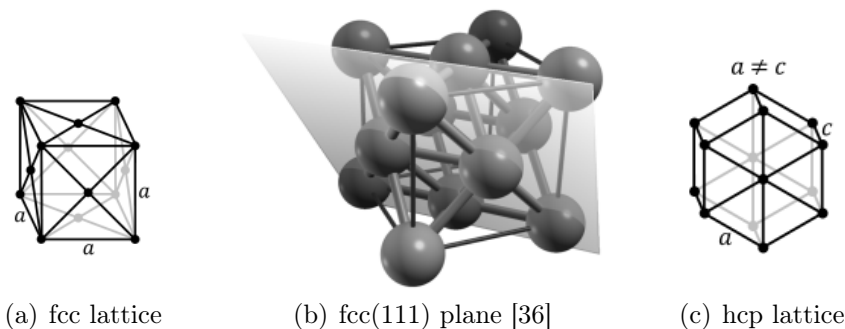


**Figure 2.6.:** Crystal structures of Pd and Zn

### 2.7.3. The Bimetallic System Pd/Zn

Pd and Zn are very miscible and form alloys with a large range of relative compositions. The cohesive energy  $E_B$ , which describes the difference between the energy per atom of a system of free atoms at rest apart from each other, and the energy of the solid, is  $-3,70$  eV/atom for palladium,  $-1,10$  eV/atom for zinc and  $-2,98$  eV/atom for PdZn [37].

The electronic properties of the system PdZn are of particular interest because the electronic perturbation induced by zinc modifies the chemical properties and a correlation between the changes in core level binding energies and variations in the ability to adsorb gases is observed.

As already mentioned, the electronic configuration of atomic Pd is  $4d^{10} 5s^0 5p^0$ . To form metal-metal bonds the palladium atom has to be promoted from  $4d^{10}$  to  $4d^{10-x-y} 5s^x 5p^y$ . This rehybridization transfers charge from Pd(4d) to Pd(5s,5p) orbitals and thus from inner and localized orbitals to outer and more diffuse orbitals. In addition the electronic structure of atomic zinc with its filled 4s subshell alters to  $4s^{2-x} 4p^x$  in order to form metal-metal bonds. Thus Zn exhibits a large fraction of empty states in the 4s and 4p valence band which gives rise to a charge transfer from Pd to the Zn(4s,4p) subshells (see [38], [39]).

According to this charge transfers the PdZn molecule shows a significant reduction in the electronic population of the Pd(4d) orbitals and an increase in the population of the Pd(5s,5p) orbitals which gives rise to a reduction in the electron-electron repulsion and moves the palladium core levels towards higher binding energies. Hence the palladium density of states profile in PdZn is more similar to the profile of copper than to that of pure palladium metals [40]. This can also be understood using simple arguments: If one mixes  $d^{10}$  (Pd) atoms with  $d^{10}s^2$  atoms (Zn) one obtains an alloy with an electronic configuration of the average atom  $d^{10}s^1$  which is the electron configuration of Cu atoms.

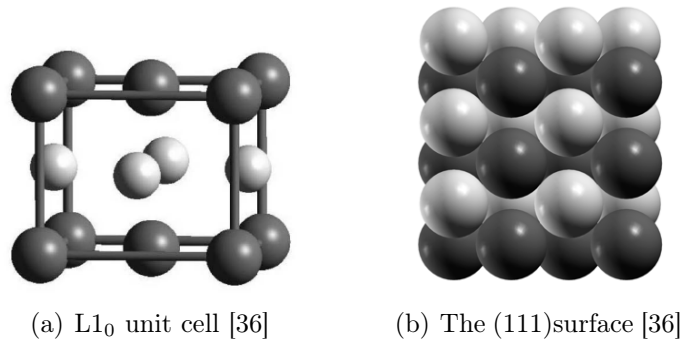


**Figure 2.7.:** The CuAu L1<sub>0</sub> tetragonal structure of PdZn.

Light spheres: Zn, dark spheres: Pd

In fact PdZn alloys with an atomic ratio of palladium to zinc close to 1 have the

structure of the tetragonal CuAu  $L1_0$  type. In figure 2.7 the  $L1_0$  lattice and the corresponding (111) surface of the PdZn alloy are shown.

The  $L1_0$  structure is a tetragonal distortion of the fcc structure by a tetragonal prism with a square base (fcc when  $c = a$ ). The lattice parameters are  $a = 4,15 \text{ \AA}$  and  $c = 3,39 \text{ \AA}$ . The lattice constant  $a$  is only slightly longer than the lattice constant  $a$  of the corresponding metal palladium but  $c$  is much shorter than the lattice constant  $a$ . On the stoichiometric (111) surface, the palladium atoms of the first layer move inward (into the bulk) while the Zn atoms of the first layer relax somewhat more outward to the surface [41].

## 2.8. The Adsorption of $H_2$ on Metal Surfaces

The interaction of hydrogen with palladium has been studied thoroughly. In figure 2.8 a simple schematic potential-energy diagram for H and  $H_2$  interacting with a palladium surface is shown.

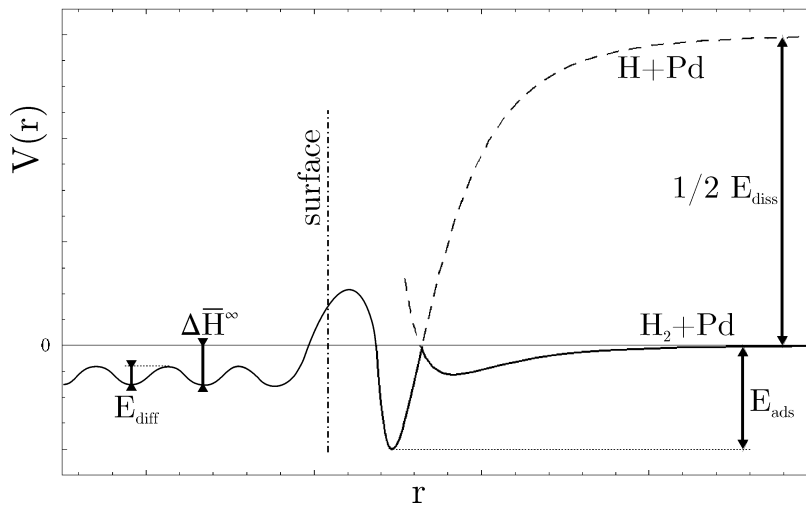


**Figure 2.8.:** Schematic potential energy diagram as a function of the distance  $r$  from the Pd surface for H between the gas phase (right) and the bulk (left).  $E_{ads}$  is the adsorption energy,  $E_{diff}$  the dissociation energy,  $\Delta \bar{H}^\infty$  the heat of solution and  $E_{diff}$  the activation energy for bulk diffusion.

The potential-energy curve for the  $H_2$  molecule exhibits a weak physisorption minimum, while the H potential energy curve has a rather deep minimum in the chemisorptive state. The crossing of the curves is below the zero energy giving rise to a spontaneous dissociation of  $H_2$  on Pd(111) [42]. The adsorption energy  $E_{ads}$  for H on Pd(111) has been measured by Conrad et al [43] to be 0.46 eV at low coverages. The equivalent quantity for the bulk is the heat of solution  $\Delta \bar{H}^\infty$  which is 0.20 eV [44]. The fact that  $\Delta \bar{H}^\infty$  is smaller than the heat of adsorption results in a preferably higher concentration of hydrogen at the surface than in the

bulk. A distinction between the different adsorption states is possible by means of desorption kinetics using TPD [45].

When considering the adsorption of hydrogen on metals one often finds a decrease of the sticking coefficient  $S$  with increasing translational energy. The sticking coefficient for such a system is shown in figure 2.9. This behaviour has traditionally been interpreted in terms of an adsorption via a molecular precursor state whereas the molecules are temporarily trapped in the physisorption state.

The trapping occurs because the molecules lose energy when impinging on the surface, mainly to the substrate phonons. Thus the energy dependence is related to the trapping probability into the precursor state and decreases with increasing energy. The sticking probability rises then again at higher energies which is explained by means of a direct activated adsorption path.

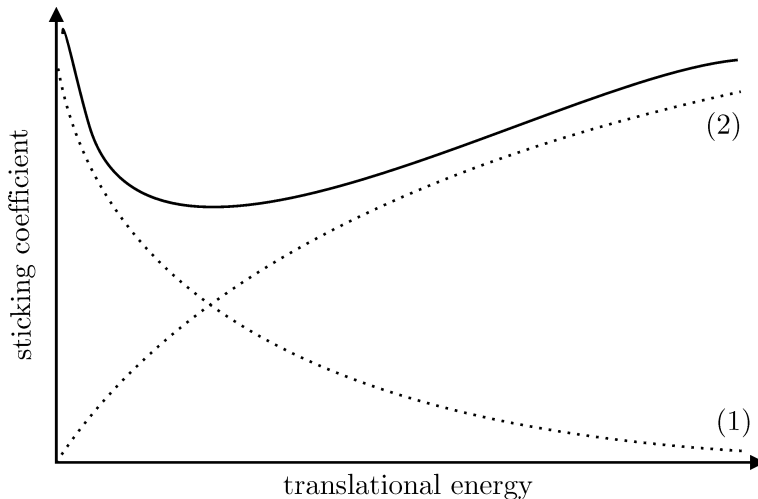


**Figure 2.9.:** Typical behaviour for the sticking coefficient versus the translational energy of the impinging molecule for  $\text{H}_2$  on Pd(111). The dashed lines correspond to the sticking coefficient for a system with a precursor path (1) and a direct activated path (2)

The precursor state is already contained in the Lennard-Jones model which was described above but especially for hydrogen adsorption on metal surfaces the energy transfer should be relatively small due to the large mismatch in the masses of the adsorbate and the substrate, making a precursor mechanism ineffective. Therefore an alternative explanation for this behaviour was proposed including adsorption facilitated through dynamical steering. Thereby the rotation of the molecule is considered (see [46], [47]):

At low translational energies the motion of the approaching molecule is strongly influenced by the interaction potential with the surface. This allows the slowly moving adsorbate to reorientate and translate across the surface in order to find the optimum dissociation position: The molecule is steered in phase space along a channel of

low potential energy directly into the dissociated state which is illustrated in figure 2.10. For example, molecules approaching the surface with their axis perpendicular to the surface will normally be reflected but due to the steering mechanism the molecule may rotate into an orientation parallel to the surface leading to dissociative adsorption [48].

However this steering effect becomes less effective with higher energies: The molecule may rotate so fast that it encounters a more repulsive part of the potential energy surface more rapid and it is therefore reflected back into the gas phase. Thus the dissociation probability and sticking coefficient also decrease with increasing energy.

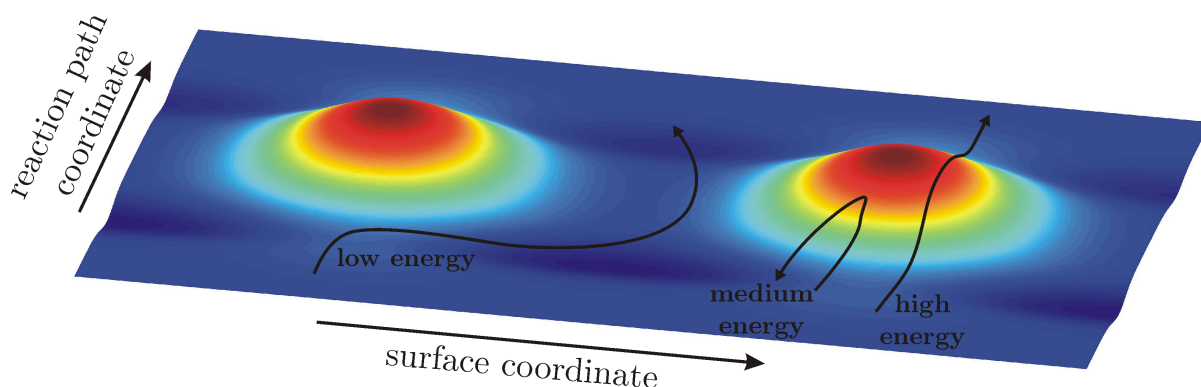


**Figure 2.10.:** Illustration of the steering effect [46]: Three typical trajectories corresponding to the low, medium and high kinetic energy regime are plotted on a cut through a six-dimensional potential energy surface including the reaction path coordinate and one surface coordinate. In this representation the reaction path coordinate connects the molecule in the gas phase with the dissociated molecule on the surface.

For both low and medium energy trajectories the energies are too small to allow a direct crossing of the barrier the particles are directed at. However, at the low kinetic energy the forces acting on the incoming particle can redirect it so that it follows a path that leads to the purely attractive region of the PES. In the case of medium energy, the same forces act on the incoming particle but now it is too fast to be steered significantly. It is reflected at the repulsive part of the potential and scattered back into the gas phase. If the energy is further increased, then the particles will eventually have enough kinetic energy to directly cross the barrier (high energy trajectory).

## 2.9. The Adsorption of CO on Metal Surfaces

Molecular bonding of CO involves the Highest Occupied Molecular Orbital (HOMO) and the Lowest Unoccupied Molecular Orbital (LUMO). For CO the HOMO is the  $5\sigma$ -orbital which is a bonding orbital. The LUMO is the  $2\pi^*$ -orbital which is antibonding with respect to the CO molecular bond.

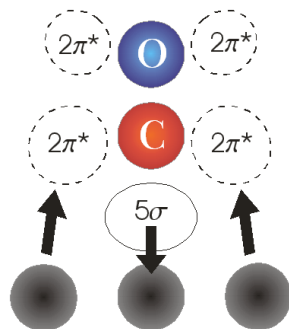


**Figure 2.11.:** Orbital scheme for CO bonding on a metal surface: The bonding mechanism involves  $\sigma$ -donation and  $\pi$ -backdonation.

The bonding mechanism of CO on metal surfaces involves two mechanisms:

- Electronic transfer from the CO( $5\sigma$ ) orbital into the empty bands of the metal. The  $5\sigma$  orbital forms bonding and antibonding combinations with the unoccupied metal states and thereby establishes a chemical bond to which the CO-molecule contributes two electrons. Thus charge is donated to the surface. This mechanism is the so called  $\sigma$ -donation. Since the  $5\sigma$  orbital carries the largest weight on the backside of the carbon atom, the CO molecule bonds in an upright position with the carbon pointing towards the surface. (see figure 2.11)
- Electronic transfer from occupied bands of the metal into CO( $2\pi^*$ ) orbitals. The  $2\pi^*$ -orbitals form bonding and antibonding combinations with the occupied metal states and electrons from the metal are back donated into the molecule. Thus this mechanism is called  $\pi$ -backdonation. Since the  $2\pi^*$ -orbital is an antibonding orbital for the CO molecule this back donation weakens the internal chemical bond of the CO molecule (see [7], [49]).

According to the formalism of MO perturbation theory (see [50], [51], [40]) the heat of adsorption of CO on a Pd adatom  $Q_{\text{CO}}$  is proportional to the occupancy of the Pd(4d) orbital ( $N_{\text{Pd}(4d)}$ ) and inversely proportional to the energy separation between the Pd(4d) and CO( $2\pi^*$ ) orbitals:

$$Q_{\text{CO}} \propto \beta^2 \frac{N_{\text{Pd}(4d)}}{E_{\text{CO}(2\pi^*)} - E_{\text{Pd}(4d)}} \quad (2.22)$$

whereas  $\beta$  is the resonance integral  $\beta = |\langle \psi_{\text{Pd}(4d)} | \psi_{\text{CO}(2\pi^*)} \rangle|$ .

Due to the interaction between Pd and Zn the Pd(4d) orbitals are shifted away from the CO( $2\pi^*$ ) orbitals and the electronic population of these orbitals is reduced by Pd(4d)  $\rightarrow$  Zn(4p) electron transfer.

Therefore, corresponding to equation 2.22, the Pd-Zn interaction weakens the strength of the Pd(4d)  $\leftrightarrow$  CO( $2\pi^*$ ) bond which gives rise to a reduction in the adsorption energy of CO on Pd.(see [39], [40]) This can be observed in TPD spectra where the CO desorption temperature of the peak maximum shifts towards lower temperatures than compared to that of pure Pd.

## 3. Experimental Setup

*This chapter provides a description of the experimental setup, that is the ultrahigh vacuum (UHV) chamber is described. Short specifications of the permeation source and the detector chamber are given together with the measurement equipment and the theoretical background of the analyzing methods.*

*In addition the preparation of the sample including the cleaning procedure and the evaporation of zinc are pictured, as well as a description of the measurement of the angular distribution*

### 3.1. Ultrahigh-Vacuum-System

Since it is important to keep the surfaces on which the measurements take place clean, UHV is needed. Thus to avoid an unintentional coverage of particles in the residual gas during the required timescales of the experiment the pressure is held at values below  $10^{-9}$  mbar.

The main features of the used UHV system have been designed by Christian Eibl. A short overview is given below (for further descriptions see [52]) along with descriptions of further adaptations and special experimental techniques.

Figure 3.1 provides a schematic buildup of the UHV system. The used vacuum system consists of two separately evacuated chambers, the main and the detector chamber. The sample holder and all necessary devices that are used to perform sample preparations are situated in the main chamber. To distinguish between particles originating directly from the sample and background particles, the detector chamber is used. Both chambers are connected to each other using a bypass which is closed during the measurements.

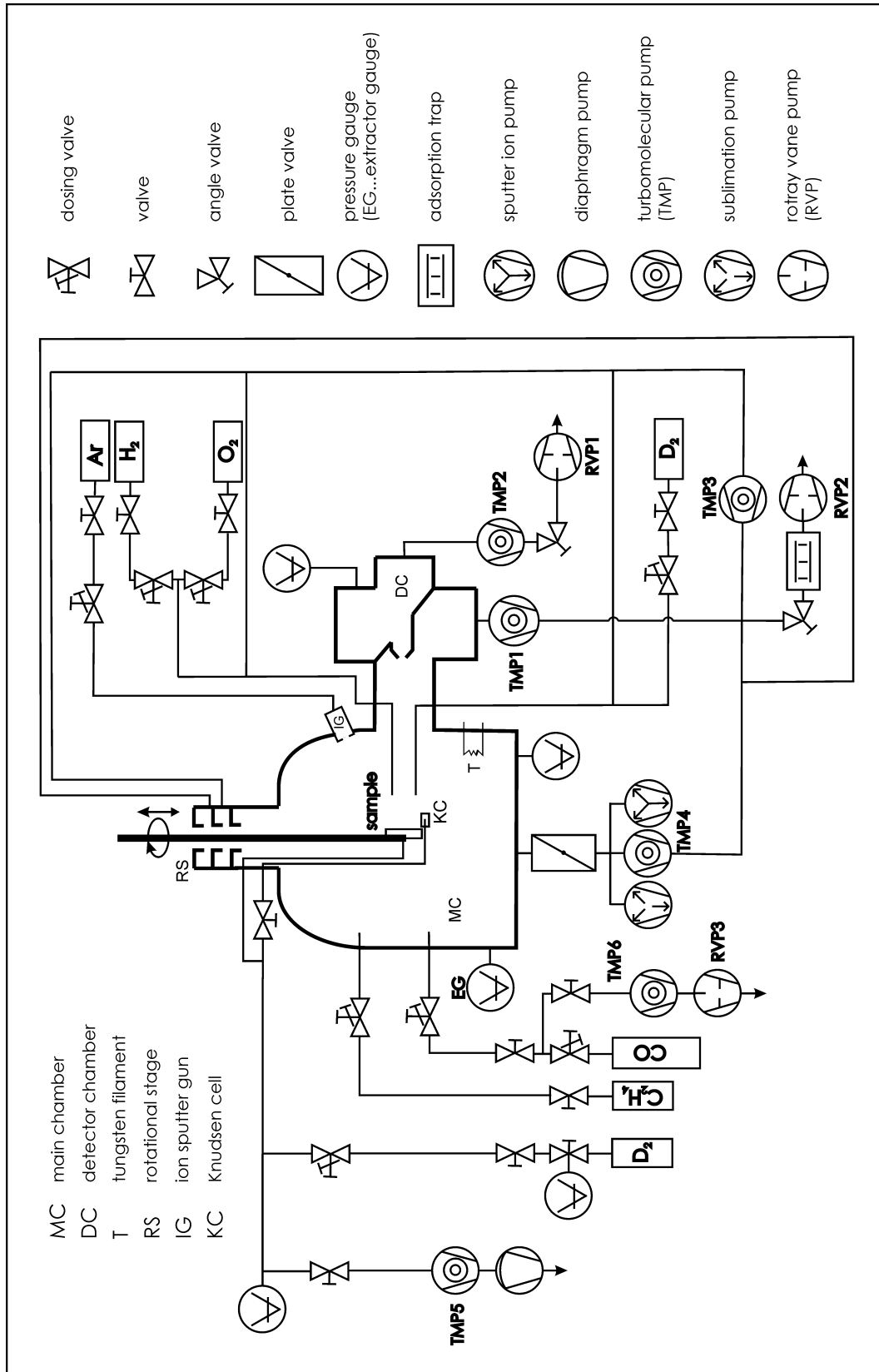


Figure 3.1.: Schematic illustration of the UHV-system.

The main chamber itself is separated into two parts by a gate-valve, whereas the lower part is evacuated using a turbomolecular pump (TMP4: LEYBOLD Turbovac 360, pumping speed  $S = 345$  l/s) and a titanium sublimation pump. The upper part holds a turbomolecular pump (TMP1: Pfeiffer TMU 521,  $S = 520$  l/s) and a small turbomolecular pump (TMP3: Pfeiffer TMU 071 P,  $S = 60$  l/s). To maintain the necessary outlet pressure, a rotary vane pump (RVP2: Pfeiffer DUO 20,  $S = 20$  m<sup>3</sup>/h) is used as forepump.

In the detector chamber, a sputter ion pump with  $S = 20$  l/s was installed but due to the slow background decrease after dosing gas and the high amount of CO in the residual gas, the ion pump was replaced by a turbomolecular pump (TMP2: Pfeiffer TMU 521,  $S = 520$  l/s) and a rotary vane pump (RVP1: Pfeiffer DUO 20,  $S = 20$  m<sup>3</sup>/h) as shown in the figure.

Several additional actions have been performed to obtain pressures in the range of  $p = 1 \cdot 10^{-10}$  Torr. Thus, each time after the vacuum system had been opened the evacuation process was followed by a bake-out of the chambers. Therefore the whole system is held at a temperature of about 130°C for at least 24 hours, mainly to reduce the amount of water in the chambers.

An extractor ionization gauge (LEYBOLD Ionivac IM 510) is used to measure the pressure in the main chamber. Since different gases are ionized according to different ionization probabilities this factor has to be taken into account when determining the partial pressure of a gas. Furthermore, the ionization gauge has to be calibrated which was done using a gas friction manometer.

By combining the pressure indication with the QMS-signal the total pressure in the UHV chamber may be corrected due to the composition of the gas and the partial pressures may be specified. During the exposure of one particular gas one might assume that the pressure is mainly caused by one nature of gas in the main chamber. Thus the displayed pressure value  $p_{\text{disp}}$  may be simply corrected by multiplying with the calibration factor  $K$  and the ionization factor  $I$  to give the real pressure  $p_{\text{true}}$ :

$$p_{\text{true}} = p_{\text{disp}} \cdot K \cdot I = p_{\text{disp}} \cdot F \quad (3.1)$$

All exposures which are given in the later sections are already corrected according to equation 3.1. The correction factors for the most commonly used gases are given in the following table.

	$F$	$I$	$K$
H <sub>2</sub>	3.60	2.45	1.47
D <sub>2</sub>	3.37	2.29	1.47
O <sub>2</sub>	1.60	1.09	1.47
CO	1.42	0.97	1.47

## 3.2. The Sample Holder and the Permeation Source

Two different kind of sample holders were used. To investigate the adsorption and desorption processes a circular Pd(111) single crystal was used. The crystal is held by small tungsten wires in the sample holder, wherewith it is heated and cooled. Thus the temperature of the crystal is adjusted by current heating and cooling the sample with liquid nitrogen. The sample holder itself is installed in the main chamber and may be rotated by  $360^\circ$  around its vertical axis and moved nearly  $\pm 20$  mm in all spatial directions

To determine the angular distribution of deuterium particles desorbing from the palladium surface another sample holder was used, that is a permeation source. Therefore a constant deuterium flux through the palladium crystal for at least half an hour is needed. Since palladium has the ability to absorb the maximum amount of hydrogen in the bulk, it is the adequate material to build a permeation source.

### 3.2.1. The Construction of the Permeation Source

(see [53], [54]) The permeation of a gas (instead of adsorbing and desorbing it) shows many advantages: The desorbing gas flux is almost constant over a time period in the range of some hours. In addition, palladium has the ability to clean the gas flux. Permeation means the penetration of a substance through a solid. Thus in a permeation source a palladium plate separates the region of high  $H_2$  pressure (gas bottle) and low  $H_2$  pressure (UHV recipient) which gives rise to transport of H from the high pressure to the low pressure site by permeation.

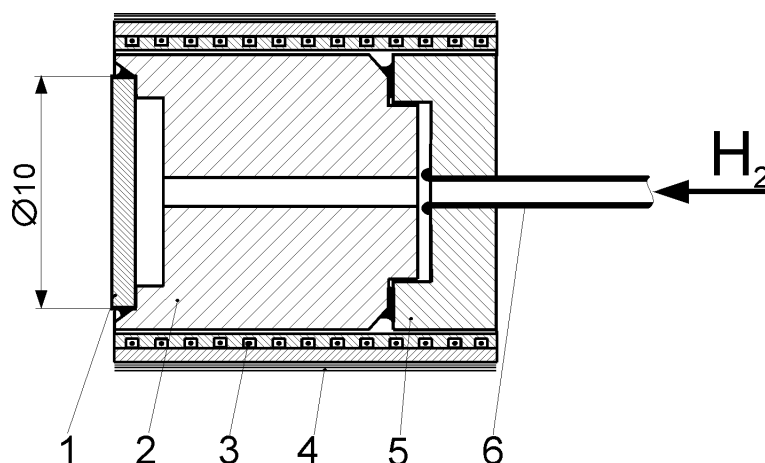


**Figure 3.2.:** Cross-section of the permeation source.

- 1: palladium sample, 2: high purity Ni-cylinder, 3: molybdenum heating coil embedded in ceramics, 4: several layers of tantalum foil for radiation shielding, 5: stainless steel cap, 6: stainless steel pipe, welded to the stainless steel cap

In 3.2 the cross-section of the permeation source is shown. The permeation source consists basically of the palladium crystal (10 mm in diameter, 1 mm thickness) which is welded into a cylinder of another high-purity material (nickel). A stainless steel cap is welded onto the nickel cylinder. The cap contains a stainless steel pipe, which is used as the gas inlet. Thus the gas is applied at high pressures from the backside of the sample crystal, giving rise to diffusion of the gas through the crystal bulk towards the outer surface. Then, at the outer surface, the permeated gas desorbs at low pressure from the palladium surface.

The cylindrical mounting has a much lower permeability for deuterium, so it is guaranteed that most of the deuterium, which is absorbed in the palladium, desorbs from the palladium on the outer surface. In fact  $D_2$  was used instead of  $H_2$  in the experiments due to the fact that there is always a rather high amount of  $H_2$  in the residual gas and thus to allow a distinction from the background.

The pressure at the backside of the permeation source is measured by a piezo - membrane gauge. During measurements, this pressure is in the range of 1 mbar. In addition the setup is covered with a ceramics, in which a molybdenum heating coil is embedded. This molybdenum coil is used to heat the sample up to 1000K.

### 3.3. The Measuring Equipment

To perform preparations and analysis of the sample surface, several measurement devices are installed in the main chamber which is shown in figure 3.3. Those are:

1. LEED (low energy electron diffraction), used to determine the surface structure.
2. To determine the particles desorbing from the surface and to measure the partial pressures, two QMS (quadrupole mass spectrometer) with one in the main chamber and one in the detector chamber are mounted.
3. AES (Auger electron spectroscopy) with which the composition of the surface is proved.
4. The zinc coverage of the surface is created using the evaporator. The corresponding rate of deposition of zinc is determined with a quartz crystal microbalance.
5. The sample surface is cleaned by sputtering with an argon - gun.
6. The respective pumping speed of the two chambers is determined by two tungsten coils

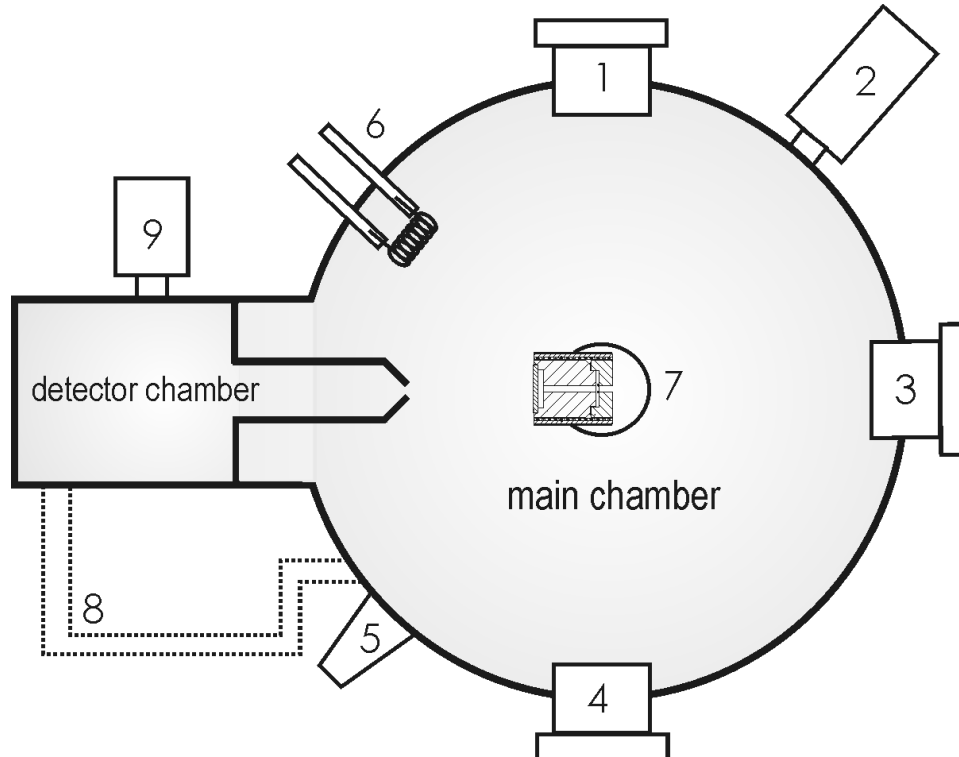


**Figure 3.3.:** Arrangement scheme of the measuring setup:

1: LEED, 2: QMS, 3: AES, 4: Zinc-evaporator and quartz crystal microbalance, 5: Argon-gun, 6: Tungsten-coil, 7: Sample-holder, 8: Bypass, 9: QMS.

A short description of the different analyzing methods is given below (see [16]).

### 3.3.1. LEED

LEED is used to analyze the surface structure of the sample. The main elements of a LEED are shown in figure 3.4.

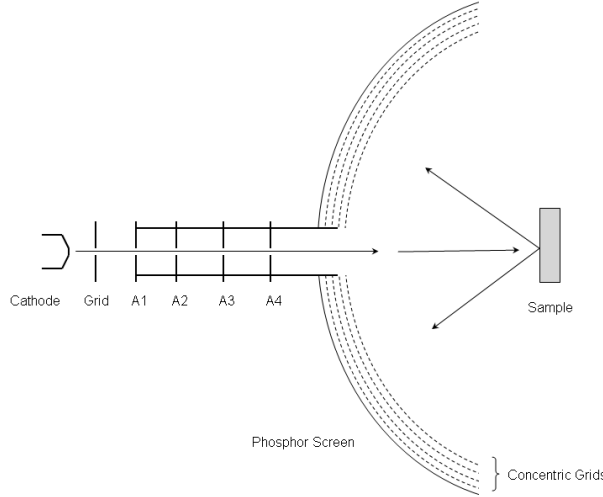


**Figure 3.4.:** Schematic diagram of a four-grid LEED

The electron gun produces a beam of collimated low-energy electrons with energies in the range of 30-500 eV. These electrons reach the well ordered sample surface, where they are scattered. Since the de Broglie wavelength of an electron is given by

$$\lambda = \frac{h}{\sqrt{2mE}}, \quad \lambda[\text{\AA}] = \sqrt{\frac{150}{E(\text{eV})}} \quad (3.2)$$

the electrons have a wavelength ( $\approx 1 - 2\text{\AA}$ ) of the order of the interatomic distances and satisfy the atomic diffraction condition.

The sample and the first grid are at earth potential. Thus after the scattering process the electrons propagate through the field-free space towards the grid. The second and third grid are used to reject the inelastically scattered electrons. Their potential is close to that of the cathode but somewhat lower in magnitude. The fourth grid is at earth potential again and screens other grids from the field of the fluorescent screen. After passing the retarding field, the elastically scattered electrons are reaccelerated towards the fluorescent screen, where they cause a light spot and the diffraction pattern is observed.

### 3.3.2. AES

Auger electron spectroscopy is used to analyze the chemical composition of the surface by measuring the energies of Auger electrons. Figure 3.5 illustrates an Auger-process.

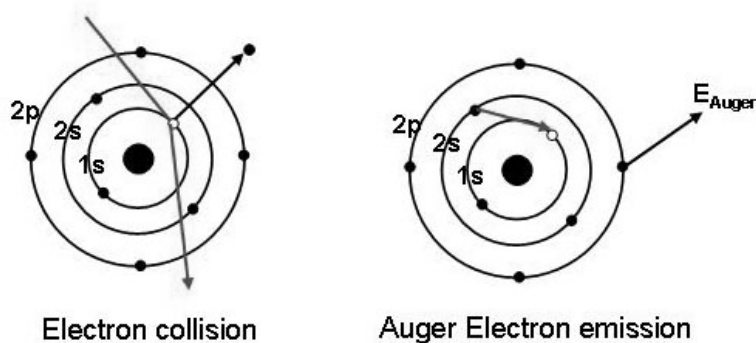


Figure 3.5.: Illustration of an Auger-process

An incident electron creates a hole in one of the core levels. An electron from a higher level fills the hole and the transition energy is imparted to another electron which is emitted as an Auger-electron. The final atomic state thus has two holes. Since the involved levels are discrete each Auger electron has a distinct energy which is characteristic of the element

The energy of the Auger electrons is determined using a cylindrical mirror analyzer, which allows only electrons with a certain energy to pass. This energy is characteristically in the range of 10eV - 2keV which corresponds to a mean free path of several atomic layers and gives rise to the surface sensitivity of AES.

### 3.3.3. QMS

Quadrupole mass spectrometer were used to detect particles according to their mass and to determine the partial pressure. In general, a mass spectrometer consists of an ion source, an analyzer and a detector. After ionizing the particles, they are passing an analyzer, where they are separated according to their mass to charge ratio.

In case of a quadrupole mass spectrometer, the analyzer is built of four parallel electrodes in such a way that opposite electrodes have the same potential. Between two opposed electrodes a voltage of  $U(t) = \pm U + V \cos(\omega t)$  is applied. The applied voltage determines the trajectories of the ions, which are moving along the center of the four electrodes. Thus for each voltage only particles with a certain mass to charge ratio are moving along a stable track and reach the detector where they are subsequently detected by a secondary electron multiplier.

### 3.3.4. Ion Sputter gun

Surface contaminants can be sputtered off together with the substrate top layer by bombardment of the surface by noble gas ions ( $\text{Ar}^+$ ). The ion sputter gun produces an ion beam by admitting argon gas through a dosing valve, directly into the ionization chamber of the gun, where the gas atoms are ionized via electron impact. The produced ions are then accelerated and directed towards the sample surface.

A side effect of the ion bombardment is the degradation of the surface structure. Therefore subsequent annealing is required to restore the surface crystallography and to remove embedded and adsorbed Ar atoms. The annealing process involves heating the sample and then maintaining a suitable temperature for an appropriate time. For the clean Pd(111) surface this is usually done at 900K for 5-15 minutes.

### 3.3.5. The Detector Chamber

To distinguish between particles of the residual gas and particles coming directly from the sample surface the detector chamber is used. In addition in the detector chamber the noise caused by reactions on hot filaments or on the main chamber walls is rather good avoided. The arrangement of the detector chamber is illustrated in figure 3.6.

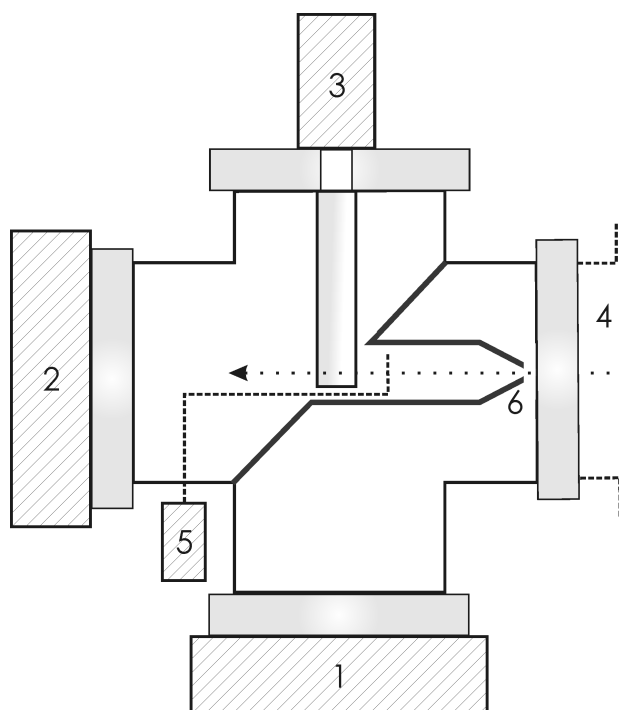


**Figure 3.6.:** Schematic image of the detector chamber.

1: Turbomolecular pump connected to the main chamber; 2: Turbomolecular pump for the detector chamber; 3: QMS; 4: Main chamber; 5: Rotary feed through with shutter; 6: Aperture

If the sample is positioned directly in front of the aperture the QMS detects only particles that are coming directly from the sample. Thus a detection of the particles that are desorbing from the sample or scattered on the sample is possible. As shown in the figure 3.6 the detector chamber is pumped with a separate turbomolecular pump. This arrangement is also called LOS (Line of Sight) since the QMS is in one line with the desorbing particles

There are some other features in the detector-chamber: A shutter can be set in front of the QMS. Thus it is possible to distinguish between the  $2\pi$ -signal and the inline-signal.

### 3.3.6. The Zinc Evaporator

The cross section of the evaporation source, which was constructed in our workshop by Martin Kornschober, is shown in figure 3.7.

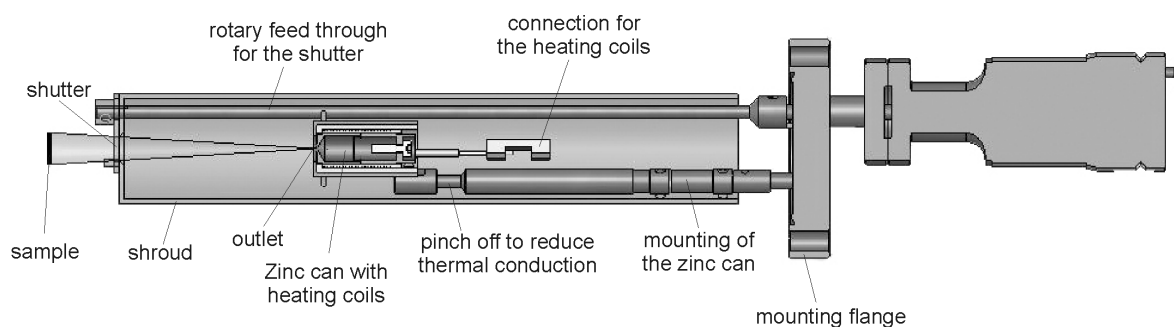


**Figure 3.7.:** Cross section of the evaporation source

To evaporate the zinc only at the desired temperature into the main chamber, the zinc-can with the heating coils itself is surrounded by a cylindrical shroud that is provided with a shutter. Thus the zinc is first heated up to the desired temperature. Then the sample is placed in front of the shutter, which is then opened for the required time, letting the zinc evaporate onto the sample surface.

The zinc-can is mounted only with a small rod to reduce the heat conduction to the surroundings. This is further prevented by the fact that the mounting rod exhibits pinch-offs. A more precise cross section of the evaporation source itself is illustrated in figure 3.8.

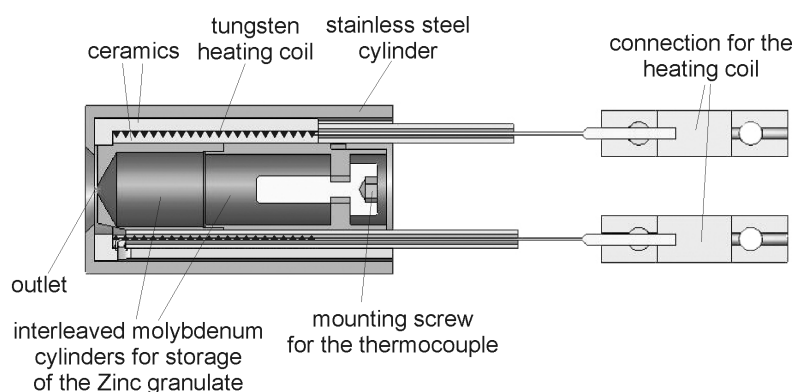


**Figure 3.8.:** Cross section of the zinc can

The zinc granulate is placed between two interleaved molybdenum cylinders whereas one of them is provided with a small outlet hole for the evaporating zinc. Between two ceramics which surround the molybdenum cylinder, the tungsten filament is wound.

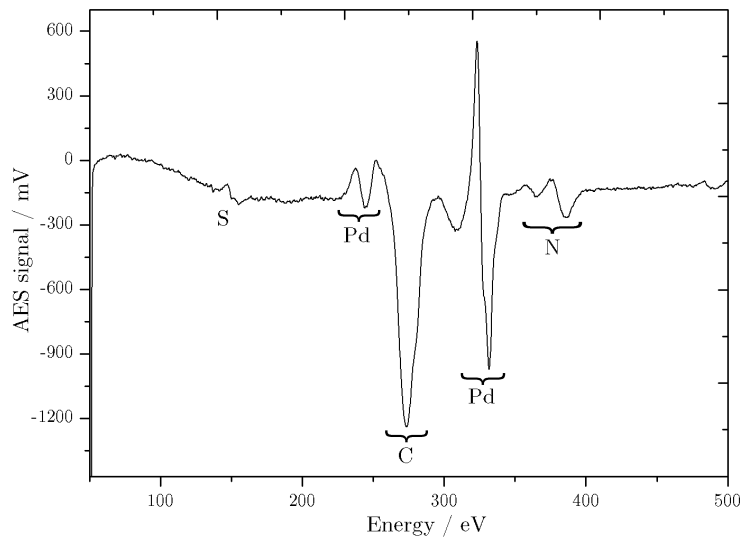
To refill the zinc, the second molybdenum cylinder can be lifted by a molybdenum screw that is provided into the base area. On this screw the thermocouple, used to measure the evaporating temperature, is clamped with a second but smaller screw. The whole assembly is then placed in a stainless steel cylinder which provides a centering device and is then mounted in the shroud.

### 3.4. Sample Cleaning

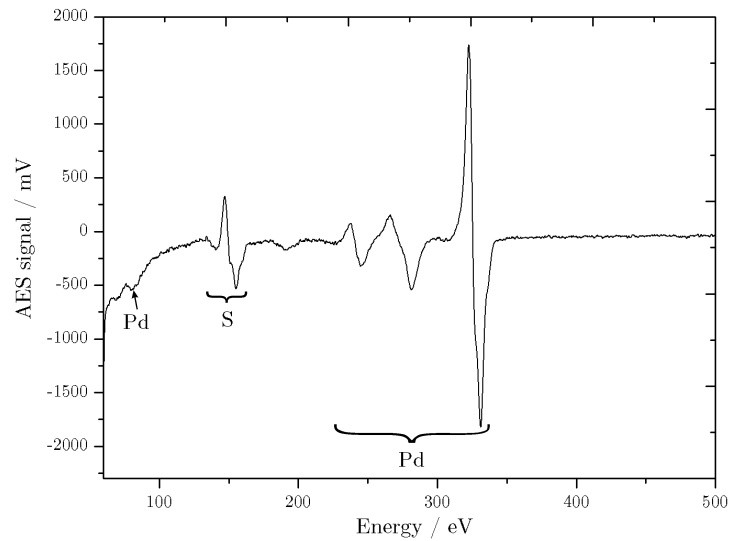
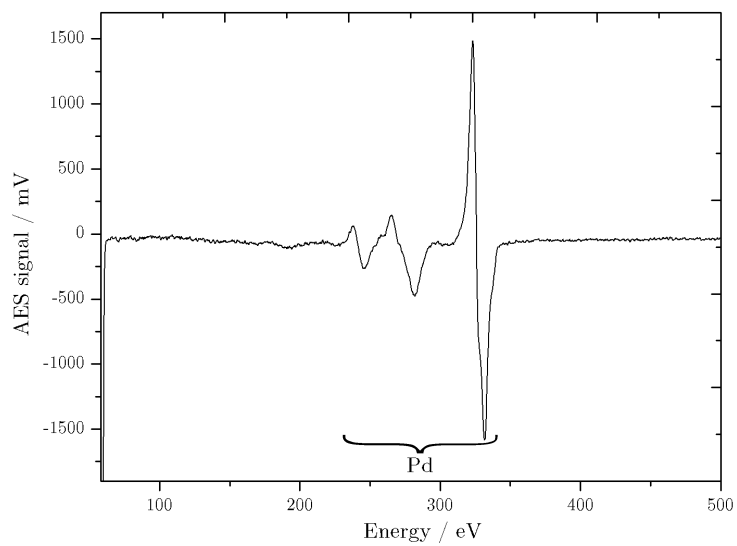
To ensure the cleanliness of the Pd(111) surface both AES and LEED were used. The position and the shape of the peaks in the AES give rise to conclusions about the contaminating elements. In addition the ratio of the peak heights allows to estimate the amount of the contamination.

Figure 3.9 shows a series of Auger-spectra which were obtained during the cleaning procedure after the UHV has been opened and the sample was exposed to air. The Auger spectrum 3.9(a) which was obtained right after the chamber had been opened indicates that the Pd(111) surface is mainly contaminated with carbon. Furthermore, there are also small amounts of nitrogen and sulfur on the surface. The carbon may be removed by  $\text{Ar}^+$  sputtering with 600 eV for about 20 minutes using an argon pressure of approximately  $4 \cdot 10^{-7}$  Torr.

But due to the fact that this ion bombardment give rise to a degradation of the surface structure, subsequent annealing is necessary. Annealing at 900 K for 5 minutes maintains again a well ordered Pd(111) surface which is proven by a sharp (1×1) LEED-pattern. But because of the annealing at such a high temperature, sulfur which is contained in the palladium bulk, migrates to the surface. Thus the Auger-spectrum 3.9(b) indicates a contamination of the surface by sulfur.



(a) After the chamber has been opened.

(b) After  $\text{Ar}^+$  sputtering of the surface followed by annealing.(c) Further  $\text{Ar}^+$  sputtering of the surface and annealing.**Figure 3.9.:** AES of the Pd(111) sample during the cleaning procedure

To remove the remaining sulfur the surface was sputtered again but now only for about 5 minutes. This was followed by annealing at 900 K for 2 minutes. Thereafter the Auger-spectrum (figure 3.9(c)) as well as the LEED indicated a clean and ordered Pd(111) surface.

In addition to that, the cleanliness of the Pd sample may also be checked by CO. Therefore CO is exposed to the sample and desorbed using TPD. Since the TDS of CO adsorbed on a clean Pd(111) surface is well-established in the literature, the obtained spectra can be compared (see figure 5.1). Thus a change in the shape of the TDS, for example an additional peak, is likely to be caused by a contamination of the surface.

Furthermore, a cleaning of the sample is necessary after zinc has been deposited onto the palladium sample. To remove the remaining zinc, thermal desorption is used. In figure 3.10 the desorption of a zinc layer on Pd(111) is shown. It displays the QMS signal of mass 64 and 66, which are the most abundant zinc isotopes with 49% and 28% natural abundance, respectively.

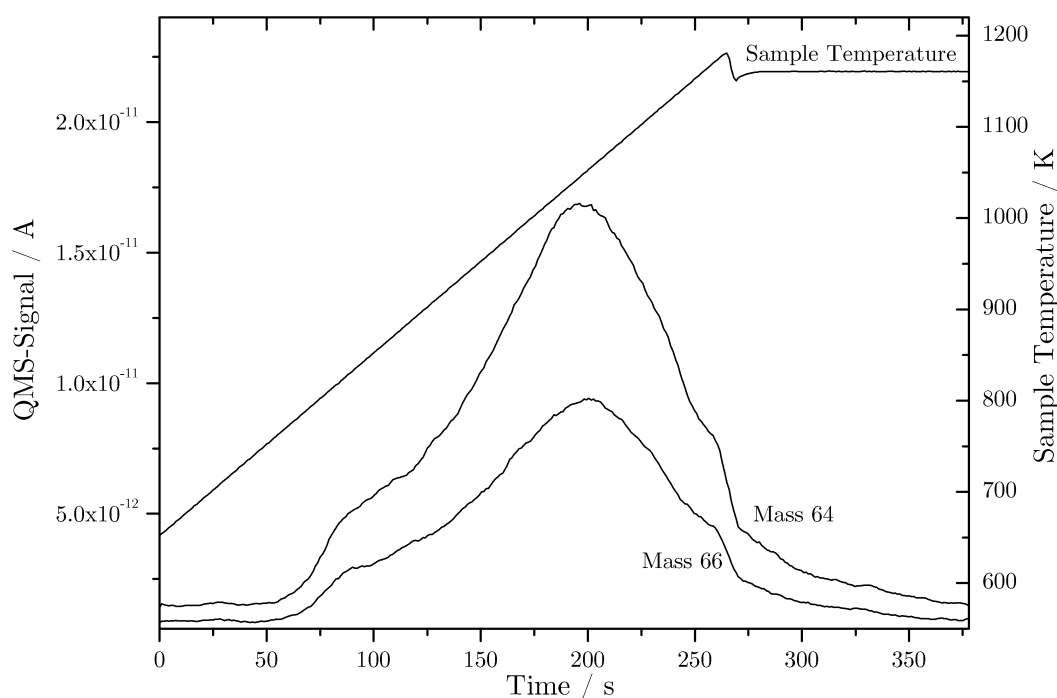


**Figure 3.10.:** Desorption of the zinc layer:

QMS-Signal of zinc (mass 64 and 66) versus time. The sample is first heated up linearly to 1180 K and then held at 1160 K for approximately 120 seconds.

Thereby the sample is first heated linearly up to 1180 K and then held at 1160 K for approximately 120 seconds. The zinc layer starts to desorb above 760 K and the sample is then held at 1160 K until there is no indication of remaining zinc in the QMS signal.

### 3.5. Preparation of the Zinc layer

During the evaporation of zinc on the Pd(111) sample Auger spectra were obtained to prove the zinc uptake. In addition to ensure that the zinc layer was distributed uniformly among the sample, Auger spectra at different positions, including the midpoint and the edges of the sample, were obtained after the evaporation. Figure 3.11 provides an Auger spectrum of zinc that has been evaporated on palladium with a surface temperature of 145 K.

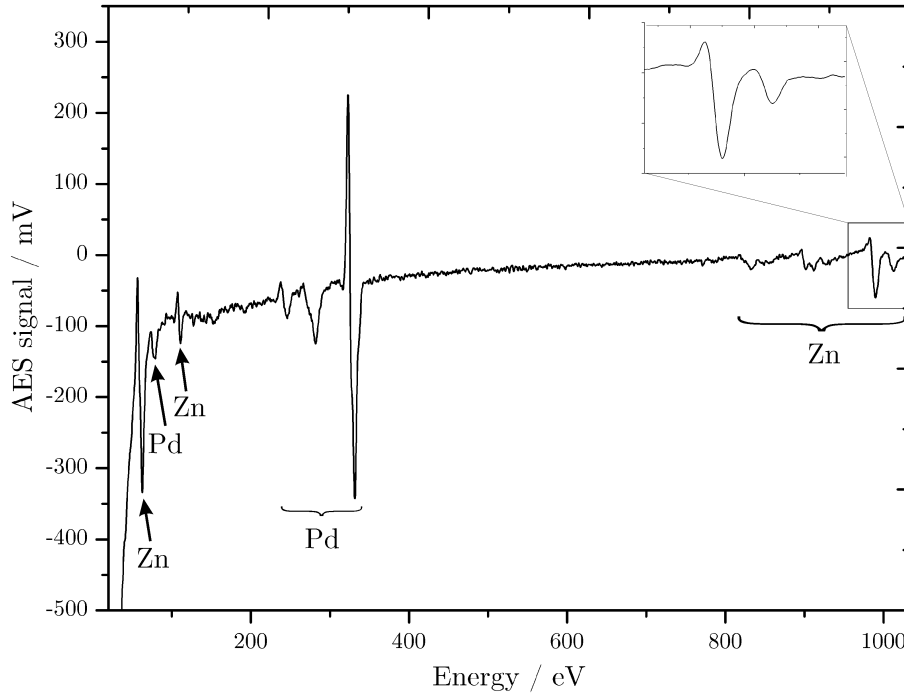


**Figure 3.11.:** AES of Zn evaporated on Pd(111)

The concentration of the element zinc on palladium may be estimated by the ratio of the peak to peak heights  $I_{Zn}$  and  $I_{Pd}$  of the zinc and the palladium peak in the Auger spectrum respectively:

$$c_{Zn} = \frac{I_{Zn}}{S_{(Zn,Pd)} \cdot I_{Pd}} \quad (3.3)$$

where  $S_{(Zn,Pd)}$  is the relative sensitivity between zinc and palladium. This factor is introduced due to the fact that the peak height may differ from peak to peak and from element to element. By obtaining the peak to peak heights  $I_{Zn}^{Std}$  and  $I_{Pd}^{Std}$  of palladium and zinc from a standard Auger spectrum which is found in an AES handbook [55], the relative sensitivity is determined using:

$$S_{(Zn,Pd)} = \frac{I_{Zn}^{Std}}{I_{Pd}^{Std}} \quad (3.4)$$

However, strictly speaking, this formula holds only in case of a Pd/Zn bulk alloy.

### 3.6. Measurement of the Angular Distribution of Desorption

For this measurements the sample with the permeation source was used. The sample is turned in front of the detector chamber and the deuterium valve is opened. The sample temperature is held constant, usually at a temperature of 390 K and after a while, an almost constant deuterium flux permeates through the sample. Whereas the base pressure is  $1 \cdot 10^{-10}$  Torr, the pressure in the main chamber  $p_{mc}$  increases to the low  $10^{-9}$  Torr regime during the permeation experiments.

The angular distribution is then measured by changing the lateral position of the sample from the leftmost to the rightmost position whereas the sample stays parallel to the detector all the time. The shifted way has a length of about 30 mm. During this procedure the deuterium signal in the detector chamber is recorded with the QMS. For this purpose the sample is held for approximately 60 seconds at the same position and then shifted 2mm further in the lateral displacement.

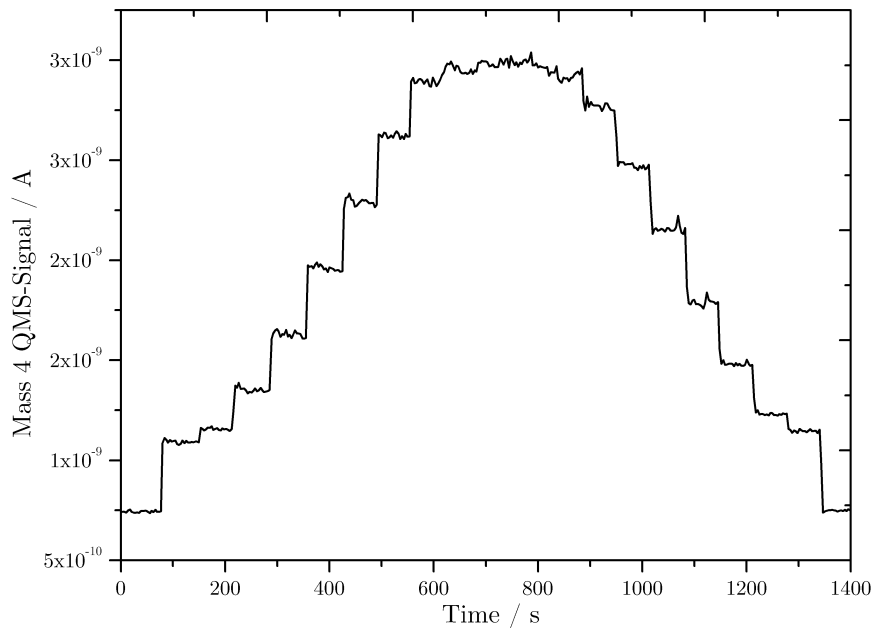


**Figure 3.12.:** Deuterium signal during the translational displacement of the permeation source versus time.  $p_{mc} \approx 1,7 \cdot 10^{-9}$  Torr,  $T_{Pd}=390$  K. The translational displacement was varied by  $\pm 15$  mm.

Figure 3.12 provides the QMS-signal of such a measurement. One can clearly see the steps of the increasing and decreasing deuterium signal after each displacement step. The most crucial point during these measurements is to keep the  $D_2$ -flux through the palladium sample constant over the whole period of time [56].

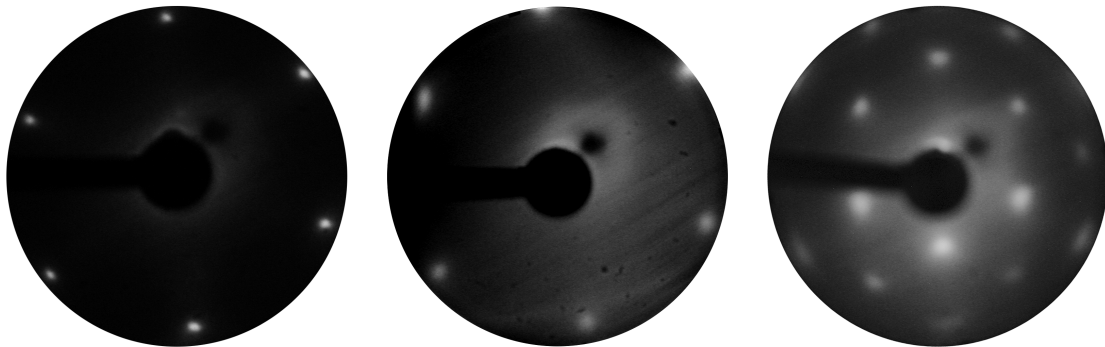
In addition, to determine the background signal, the sample holder is turned  $180^\circ$  away from the detector chamber at the beginning and the end of each measurement. The background is then subtracted in the later analysis.

## 4. Zn and ZnO on Pd(111)

*In this chapter the measurement results of Zn and ZnO on Pd(111) are presented together with proposals of the structures which are formed. The desorption kinetics of zinc on palladium is investigated including the heat of adsorption and fitting and simulation procedures according to the desorption spectra are performed.*

### 4.1. Zn on Pd(111)

To prepare a thick layer of zinc ( $\approx 10$  monolayer) on the Pd(111) surface, zinc was evaporated onto the sample surface at room temperature, whilst the evaporator was held at a temperature of 603 K. After carefully annealing the sample at 350 K, a well defined (1 $\times$ 1) LEED pattern was observed which is shown in figure 4.1(b). Compared to the the LEED pattern of clean Pd(111) (figure 4.1(a)) the spots are somewhat more diffuse but the size of the hexagon stays quite the same. This seems to be plausible, given the fact that the lattice mismatch between the Zn(0001) plane and the Pd(111) plane is just about 3% (see 2.7.2). Therefore the zinc multilayer may correspond to the growth of epitaxial overlayers of pure zinc metal.



(a) (1 $\times$ 1)-pattern of clean Pd(111); 53 eV beam energy    (b) (1 $\times$ 1)-pattern of the Zn multilayer; 53 eV beam energy    (c) (2 $\times$ 2)-pattern of the Zn monolayer; 47 eV beam energy

**Figure 4.1.:** LEED patterns of the prepared Zn layers on Pd(111)

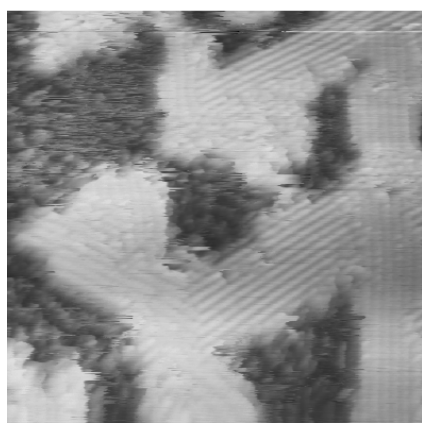
The zinc coverage in the multilayer region may be reduced by thermal desorption. Thus the sample was heated up to 600 K linearly. Since zinc atoms of the underlying layers only start to desorb above 760 K (see figure 3.10) whereupon the multilayer

desorption peak is already observed in the temperature range from 400 to 600 K, it is clear that heating the multilayer up to 600 K must lower the adsorbed amount of Zn.

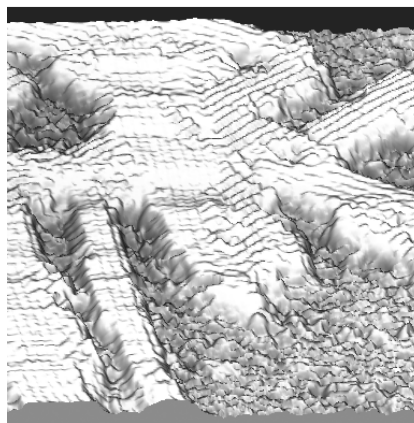
This is due to the fact, that the upper zinc layers provide slightly different environments for zinc binding. Thus the multilayer desorbs at lower temperatures whereas the underlying layers stay on the surface because of the stronger Pd-Zn bonds.

After the desorption of the Zn multilayer the LEED pattern exhibits a  $(2 \times 2)$  superstructure (figure 4.1(c)). This was interpreted by Gabasch et al [57] by means of a  $p(2 \times 2)$ -3Zn surface adlayer with a coverage of 0.75 monolayer. However Bayer et al [38] reported a  $p(2 \times 1)$  superstructure for one monolayer of Zn on Pd(111) due to an obtained Pd:Zn ratio of 1:1 in the topmost layer, measured by XPS.

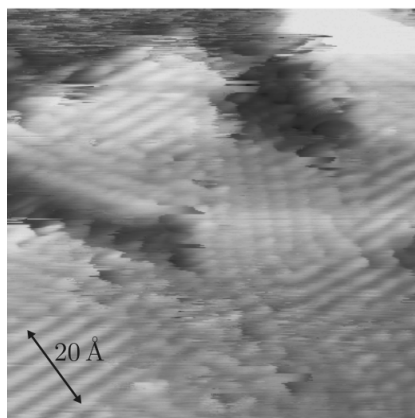
In fact a  $p(2 \times 1)$  superstructure including all three domains gives rise to the same LEED pattern as the  $p(2 \times 2)$  superstructure. Thus the structure may not be distinguished using LEED but new STM pictures obviously favour the  $p(2 \times 1)$  superstructure.



(a)  $200 \times 200 \text{ \AA}$ , +0.14 V, 2 nA



(b) 3D:  $200 \times 200 \text{ \AA}$ , +0.14 V, 2 nA



(c)  $100 \times 100 \text{ \AA}$ , +0.14 V, 2 nA

**Figure 4.2.:** STM images of Zn evaporated on Pd(111), with the friendly permission of DI Gunter Weirum.

The STM pictures of Zn evaporated on Pd(111) at room temperature were obtained by DI Gunter Weirum and are provided in figure 4.2. One can clearly see the bright stripes on the dark background, indicating the zinc rows of the ordered  $(2\times 1)$  superstructure. It is also quite interesting that there seem to be big areas of unordered zinc adsorbates between the ordered structures.

Furthermore, one can see from figure 4.2(c) that the distance between two zinc rows is approximately  $5 \text{ \AA}$  which is in a good agreement to the distance between two next nearest palladium rows ( $\approx 4.75 \text{ \AA}$ ) of the substrate.

There is a strong indication that the  $p(2\times 1)$  superstructure arises due to the formation of a palladium zinc surface alloy. After depositing zinc in the monolayer and submonolayer range at a sample temperature of 150 K no sharp LEED pattern was visible. Annealing this zinc layer at 350 K gives rise to a sharp  $(2\times 2)$  LEED pattern which may be allocated to the  $p(2\times 1)$  superstructure including all three domains as described above. In addition Bayer et al [38] reported the formation of a surface alloy at 310 K and CO adsorption experiments which will be presented later on demonstrate the same.

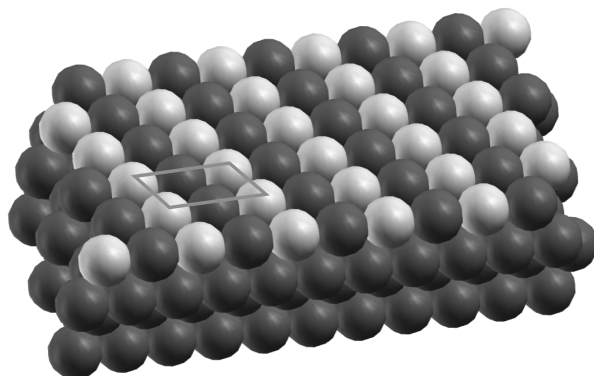


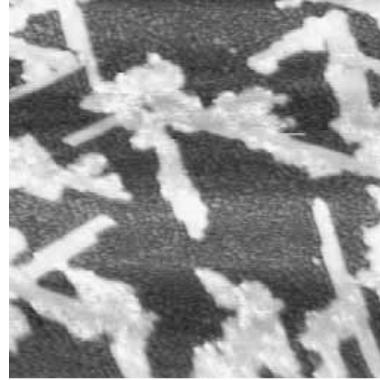
**Figure 4.3.:** Structure model for a  $p(2\times 1)$  Zn superstructure on Pd(111).  
Light spheres: Zn, dark spheres: Pd [36]

Therefore it is likely that the  $p(2\times 1)$  superstructure corresponds to a surface alloy and the proposed structure model is displayed in figure 4.3. From the outlined rhomboid in the figure, one can see that in each unit cell there is one zinc and one palladium atom. Thus the  $(2\times 1)$  superstructure corresponds to a zinc coverage of 0.5 monolayer.

Before proceeding with the TPD spectra of zinc on palladium we want to have a further look at the STM pictures. In figure 4.4 STM pictures of the same sample which was shown in 4.2 are provided, but now with a smaller magnification.



(a)  $1000 \times 1000 \text{ \AA}$ , +1 V, 1 nA



(b)  $500 \times 500 \text{ \AA}$ , +1 V, 1 nA

**Figure 4.4.:** STM images of Zn evaporated on Pd(111), with the friendly permission of DI Gunter Weirum.

The bright areas with the ordered  $(2 \times 1)$  Zn superstructure can easily be distinguished from the dark background, representing the Pd(111) substrate. The pictures reveal a growth of the zinc layer in islands which even exhibit a kind of a dendritical appearance. We want to refer to this particular shapes of the islands later on.

### 4.1.1. Desorption Kinetics of Zn on Pd(111)

To obtain information about the adsorption kinetics of zinc on Pd(111), increasing amounts of zinc were deposited on the sample, followed by TPD. The corresponding TPD spectra are shown in figure 4.5. Therefore the sample was shifted 5 mm towards the entrance slit of the detector chamber which gives rise to a better resolution of the TPD spectra.

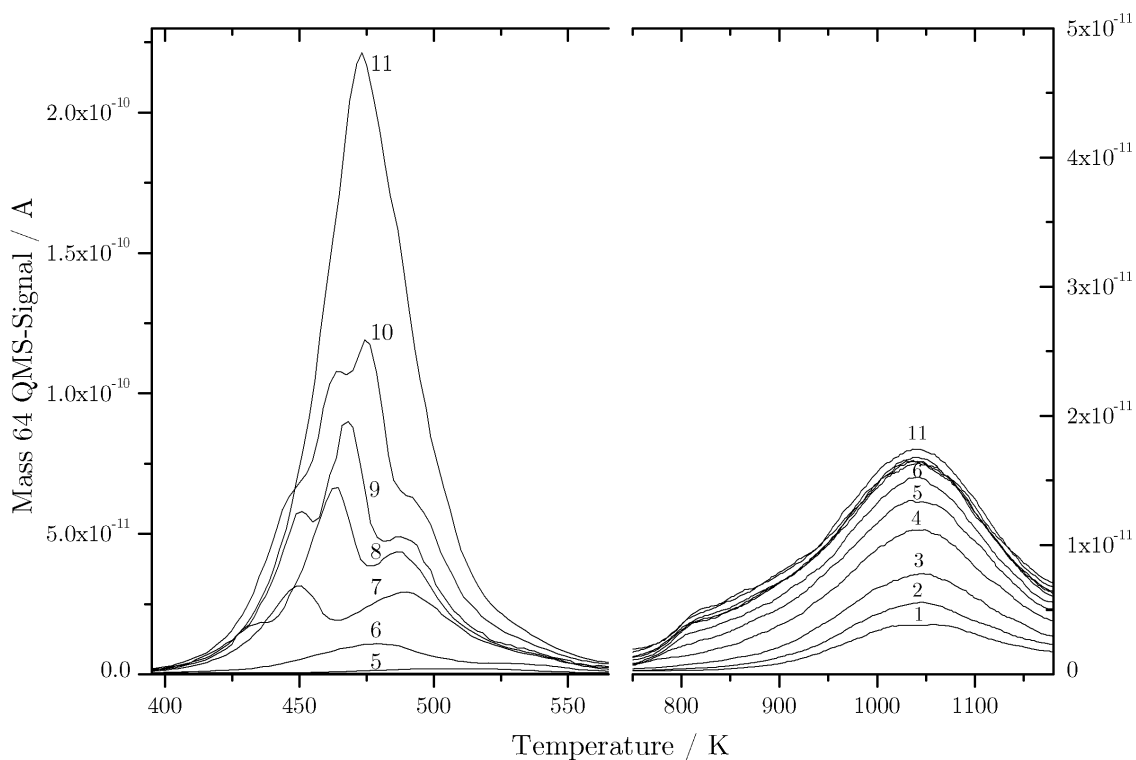


**Figure 4.5.:** Desorption series of Zn on Pd(111) with increasing amounts of deposited Zn. The sample was held at 150 K and Zn was evaporated at  $\approx 600$  K for  $t_{\text{evap}} = 17$  s, 25 s, 35 s, 50 s, 90 s, 120 s, 180 s, 210 s, 240 s, 300 s and 500 s. The high and low temperature peak are shown with different y-scales. Heating rate =  $2 \text{ K} \cdot \text{s}^{-1}$

The high temperature desorption peak with its maximum at 1040 K exhibits an explicit first-order behaviour. Thus it is possible to determine the desorption energy according to the Redhead concept (see section 2.6.1). Equation 2.21 with  $\beta = 2 \text{ K} \cdot \text{s}^{-1}$  and  $\nu = 10^{13} \text{ s}^{-1}$  gives a heat of adsorption of  $281 \pm 5 \text{ kJ mol}^{-1}$  for the zinc monolayer on Pd(111). This is in a good agreement with Bayer et al [57] who reported a value of  $268 \text{ kJ mol}^{-1}$ . It should be mentioned that it is fairly strange that the desorption peak only seems to saturate when the low temperature peak already starts to evolve and that it exhibits a small shoulder at around 800 K.

When the amount of the deposited zinc is increased a second peak at a temperature of 520 K starts to develop in the TDS. With further increasing zinc deposition the

peak grows more and more which is due to the fact that it is attached to the tail of a third evolving peak. To allow a better analysis of this low temperature peaks the measured data is fitted using multiple peaks in a way that the sum of the fitted peaks coincides with the measured curve. To include peak shapes according to zero order and first order kinetics an asymmetric double sigmoidal function was used according to:

$$y = y_0 + A \cdot \frac{1}{1 + \exp\left(-\frac{T-T_c}{w_1}\right)} \cdot \left(1 - \frac{1}{1 + \exp\left(-\frac{T-T_c}{w_2}\right)}\right) \quad (4.1)$$

with the background  $y_0$ , the amplitude  $A$ , the position of the center  $T_c$  and the rise and fall given by  $w_1$  and  $w_2$ . The result of the fitting procedures is shown in figure 4.6. The figure also provides the measured data (circles) together with the cumulative peak after the fitting for curve number 10 of figure 4.5.

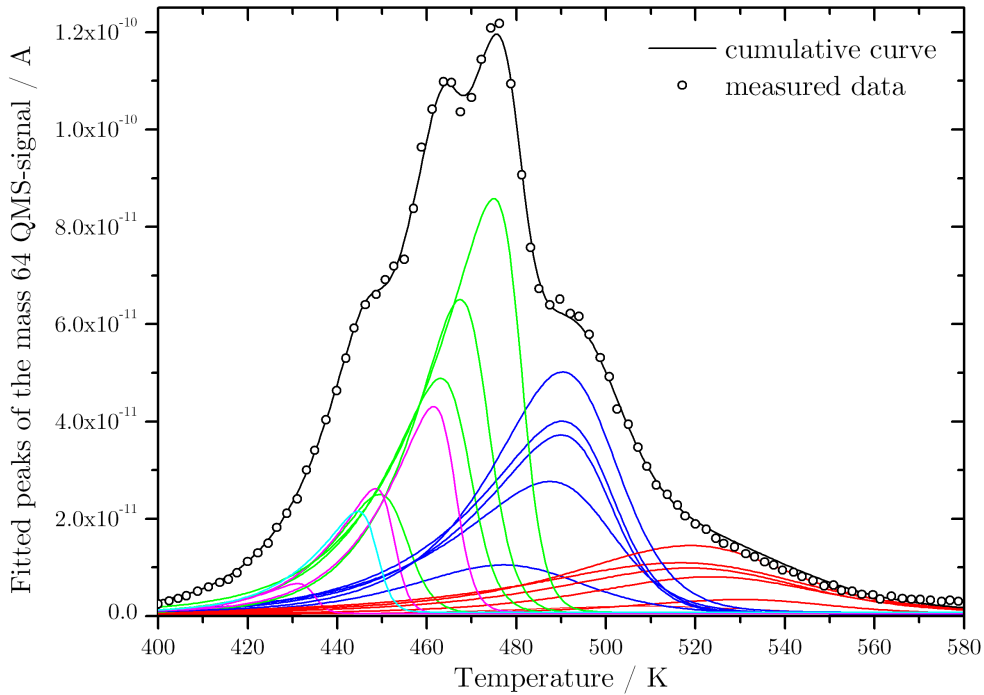


**Figure 4.6.:** Curves 6-10 in the desorption series of figure 4.5 fitted with multiple peaks.

One can see that the desorption maximum of the first low temperature peak (red curves in figure 4.6) stays nearly at the same position, which gives rise to the conclusion that the desorption kinetics is still of first order. Thus the desorption energy is determined to be  $138 \pm 5 \text{ kJ mol}^{-1}$ . By assuming first order desorption for the second low temperature peak (blue peak) which occurs at 490 K, the corresponding heat of desorption equals  $130 \pm 5 \text{ kJ mol}^{-1}$  according to Redhead.

A third peak occurs at 450 K and shifts up to 475 K with increasing amount of

deposited zinc. Due to this behaviour and the fact that the peak is caused by zinc atoms in the multilayer region one may expect zero order kinetics. This is even supported by the peak shapes of the fitted peaks (green curves in figure 4.6). However, there is a deviation from the theoretical TPD spectra (figure 2.5(a)) namely the occurrence of zero order desorption seems to be followed by a transition to first order desorption.

This may be due to the fact that when the reservoir of desorbing particles depletes, the desorption order approaches more and more first order kinetics. The effect might also be explained due to the structure of the adsorbed zinc layer. If we recall the STM pictures of figure 4.4 with the zinc islands, a possible scenario would be a preferred desorption of zinc atoms from the perimeter of the islands due to a smaller binding energy which would give rise to a  $1/2$  order of desorption [58].

The occurrence of both zero and first order desorption may also be explained by a mechanism according to the following scheme (see [58]): During the desorption process there exist both dilute and dense phases whereas the equilibrium between them is maintained. Atoms desorb from the dilute phase which is held constant at the expense of the dense phase. Thus zero order desorption occurs. As the desorption proceeds the dense islands become smaller and smaller. After the dense phase is totally depleted, leaving solely the dilute phase, the desorption becomes coverage dependent. Hence first order kinetics will be observed.

But let us now return to the analysis of the TPD spectra. For zero order kinetics, according to equation 2.20, the logarithm of  $\ln(d\theta/dT)$  plotted versus  $1/T$  gives a straight. The QMS-Signal is direct proportional to the rate of desorption and when taking the logarithm this proportionality constant is only added to the intercept of the straight but does not change the straight's slope.

Thus it is possible to determine  $E_{\text{des}}$  from the QMS-Signal: The resulting slope of the straight equals  $E_{\text{des}}/R$  and the desorption energy of the third low temperature peak (green curves) is determined to be  $118 \pm 5 \text{ kJ mol}^{-1}$ . The same holds for the fourth peak (magenta curves in figure 4.6) and the obtained desorption energy of  $116 \pm 5 \text{ kJ}$  is just slightly smaller.

Finally the desorption energy of the zinc multilayer (peak 11 in figure 4.5 at 475 K) is determined using zero-order desorption kinetics to be  $114 \pm 2 \text{ kJ mol}^{-1}$ . This value is in a good agreement with the heat of vaporization of zinc which is reported to be  $115 \text{ kJ mol}^{-1}$  in the literature [35].

Of course one might argue that the curve according to equation 4.1 which was used in the multiple fitting procedure is not motivated due to a physical equation. Therefore the measured data were also fitted using numerical solutions of the Polanyi Wigner equation (equation 2.19). Multiple curves for a given desorption order were calculated together with the cumulative curve. The parameters  $\theta$ ,  $\nu$  and  $E_{\text{des}}$  of each

single curve were varied to minimize the root mean square of the difference of the cumulative and the measured curve. A precise description of the program is given in the appendix.

In figure 4.7 the result of the fitting procedure for curve number 10 of figure 4.5 is given. Thereby the first three peaks were simulated according to the Polanyi Wigner equation (2.19) with  $n = 0.5$  and the last two peaks with  $n = 1$ .

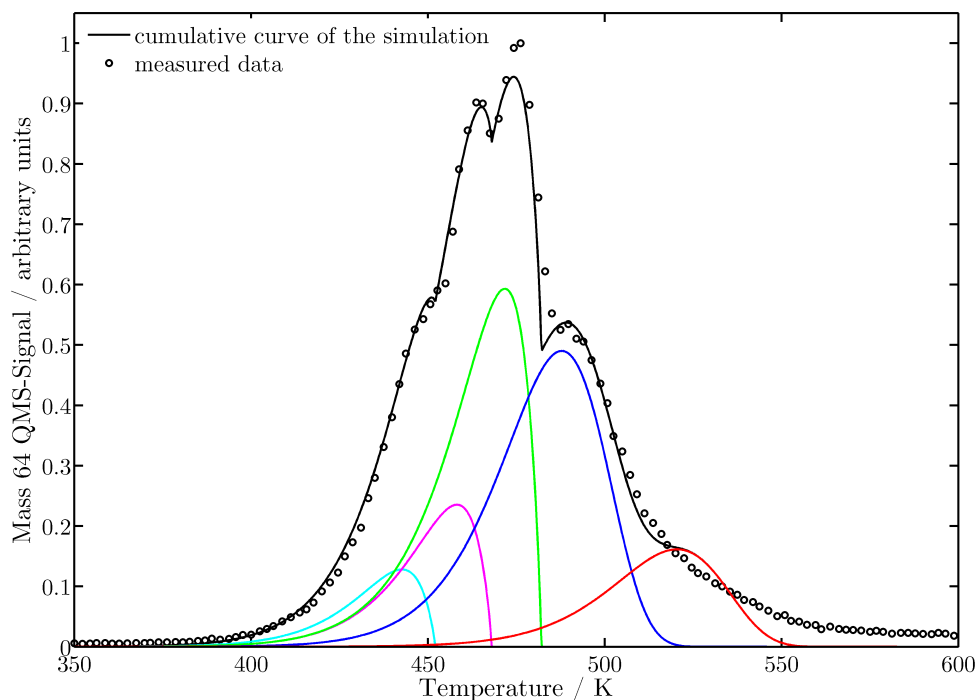


**Figure 4.7.:** Curve 10 of the desorption series of figure 4.5 fitted with multiple peaks whereas each peak was simulated according to the Polanyi Wigner equation.

This was done for the curves 6-10 in figure 4.5. The detailed results for each single curve are given in the appendix. After taking the mean of all simulated curves, the corresponding desorption energies were determined to be  $116 \pm 5 \text{ kJ mol}^{-1}$ ,  $117 \pm 5 \text{ kJ mol}^{-1}$ ,  $119 \pm 5 \text{ kJ mol}^{-1}$ ,  $128 \pm 5 \text{ kJ mol}^{-1}$  and  $139 \pm 5 \text{ kJ mol}^{-1}$ . Hence the simulated values coincide really good with values that have been obtained previously with the multiple peak fitting using the asymmetric double sigmoidal function.

Of course, it is also possible to vary the desorption order in the simulations but it was seen that this does not cause any major changes in the desorption energies.

The same experiments were repeated whereas the palladium sample was now held at 300 K during the evaporation. Figure 4.8 provides the desorption series with increasing amounts of deposited zinc.

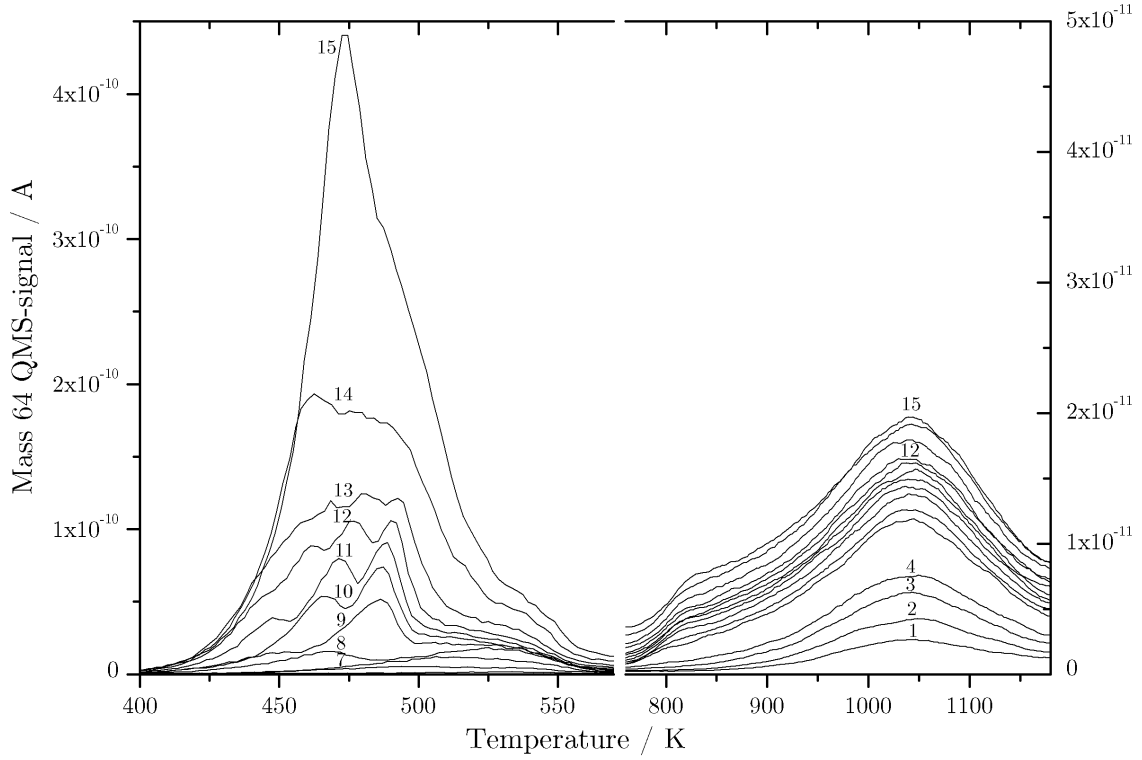


**Figure 4.8.:** Desorption series of Zn on Pd(111) with increasing amounts of deposited Zn. The sample was held at 300 K and Zn was evaporated at  $\approx 600$  K for  $t_{\text{evap}} = 15$  s, 30 s, 45 s, 85 s, 90 s, 100 s, 120 s, 150 s, 180 s, 210 s, 240 s, 300 s, 360 s, 450 s and 720 s. High temperature and low temperature peak are shown with different y-scales. Heating rate =  $2 \text{ K} \cdot \text{s}^{-1}$

The shape and position of the high temperature desorption peak remain the same compared to the TPD spectra which have been obtained after preparing the zinc layer at 150 K. Again, the measured data in the multilayer region were fitted using multiple peaks according to equation 4.1, which is presented in figure 4.9.

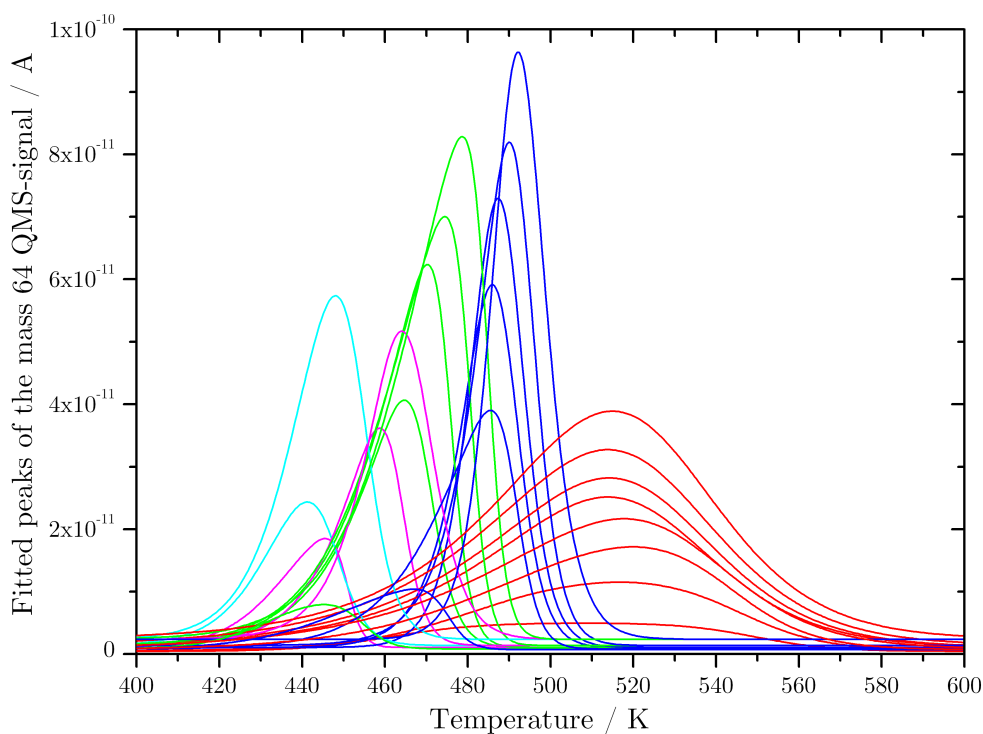


**Figure 4.9.:** Curves 6-13 of the desorption series of figure 4.8 fitted with multiple peaks.

The first low temperature peak (red curves in figure 4.9) with its peak maximum at 513 K obeys the characteristic peak shape of first order desorption kinetics and the desorption energy is determined to be  $136 \pm 5 \text{ kJ mol}^{-1}$ .

The next peaks (green curves in figure 4.9) with their peak maximum shifting from 470 to 492 K correspond to zero order desorption kinetics. The same holds for the third low temperature peak (blue curves in figure 4.9) between 450 and 477 K and the fourth peak (magenta curves in figure 4.9) between 440 and 463 K.

Thus the according desorption energies are calculated to be  $129 \pm 5 \text{ kJ mol}^{-1}$  for the second,  $122 \pm 5 \text{ kJ mol}^{-1}$  for the third and  $121 \pm 5 \text{ kJ mol}^{-1}$  for the fourth low temperature peak. In addition the desorption energy of the zinc multilayer (big single peak at 475 K in figure 4.8) is determined to be  $117 \pm 5 \text{ kJ mol}^{-1}$ .

For the curves 7-13 in figure 4.9 the simulation according to the Polanyi Wigner equation was again carried out and the corresponding desorption energies were determined to be  $119 \pm 5 \text{ kJ mol}^{-1}$ ,  $122 \pm 5 \text{ kJ mol}^{-1}$ ,  $124 \pm 5 \text{ kJ mol}^{-1}$ ,  $128 \pm 5 \text{ kJ mol}^{-1}$  and  $137 \pm 5 \text{ kJ mol}^{-1}$ . For the detailed results it shall be referred to the appendix.

In general one can say that, when increasing the sample temperature at which zinc is deposited from 150 to 300 K, the obtained adsorption energies coincide within the given uncertainty in both cases. However, the first order desorption peak around 520 K is more pronounced in the TDS spectra of zinc deposited at 300 K. Furthermore, the single peaks obtain a smaller width and are more noticeable separated in the latter case.

## 4.2. ZnO on Pd(111)

To achieve a ZnO layer on the Pd(111) sample, a zinc multilayer was prepared followed by flashing away the multilayer as described above. After that, the zinc layer was oxidized by holding the sample at 500 K in the presence of oxygen ( $p_{\text{O}_2} \approx 1 \cdot 10^{-6}$  Torr) for roughly 20 minutes. Finally the sample was heated up to 720K. The LEED pattern of the prepared ZnO layer on Pd(111) is provided in figure 4.10. It may be interpreted in terms of a commensurate  $(6 \times 6)$  superstructure.

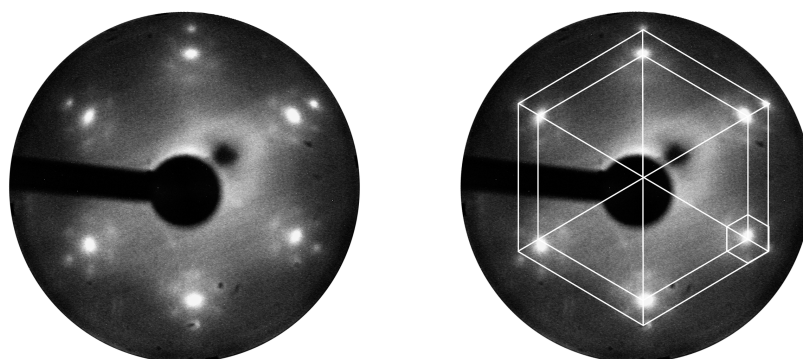
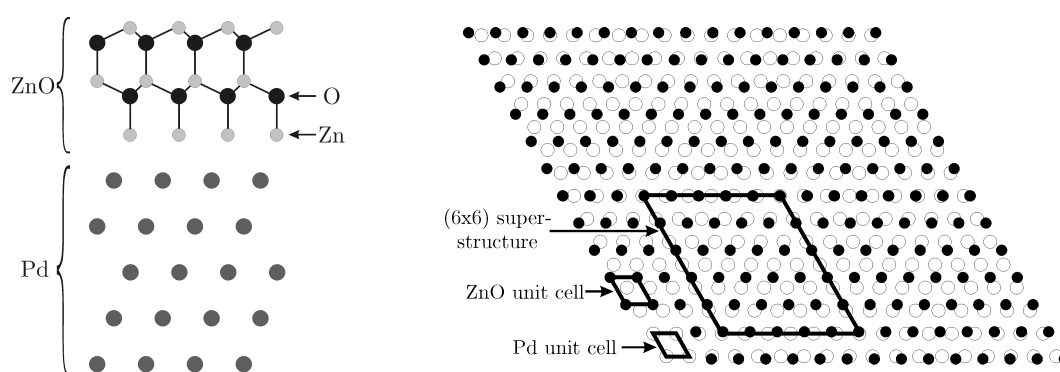


**Figure 4.10.:** LEED pattern of ZnO on Pd(111); beam energy: 69eV

The theoretical calculations of Zaoui [59] showed that the work of separation of ZnO{0001}/Pd(111) interfaces obtains the highest value for Zn-terminated interfaces. According to their calculations the energetically most favourable configuration is those with the Zinc atoms on fcc hollow sites of the Pd(111) bulk which is shown in figure 4.11(a).



(a) Calculated atomistic structure model of ZnO/Pd [59]

(b) Structure model of the  $(6 \times 6)$  ZnO Wurtzite superstructure on Pd(111): Pd: white, ZnO: black circles

**Figure 4.11.:** ZnO structure on Pd(111))

Therefore, the most likely structure model of the  $(6 \times 6)$  ZnO superstructure is an epitaxial overlayer of the hexagonal ZnO Wurtzite (0001) plane which was also

reported by Gabasch et al [57]. A simplified structure model is drawn in figure 4.11(b). It displays the hexagonal structure of the Pd(111) surface (white circles) whereas the length of the unit cell (small outlined rhombus in the bottom-left corner) is  $2.75 \text{ \AA}$ . The ZnO Wurtzite (0001) plane on top of the Pd, represented by the black circles, exhibits a hexagonal structure as well but the unit cell is slightly larger with a length of  $3.29 \text{ \AA}$  according to the literature. Thus the ratio of the unit cell lengths is  $1.196 \approx 6/5$  which gives rise to the  $(6 \times 6)$  superstructure, outlined by the big rhombus in the figure.

In the right picture of figure 4.10 the LEED pattern is shown again whereas the corresponding hexagons are now highlighted. Since the LEED pattern represents the reciprocal lattice, the big outermost hexagon corresponds to the small Pd(111) unit cell the big inner hexagon to the slightly larger ZnO (0001) unit cell and the small hexagon corresponds to the  $(6 \times 6)$  superstructure.

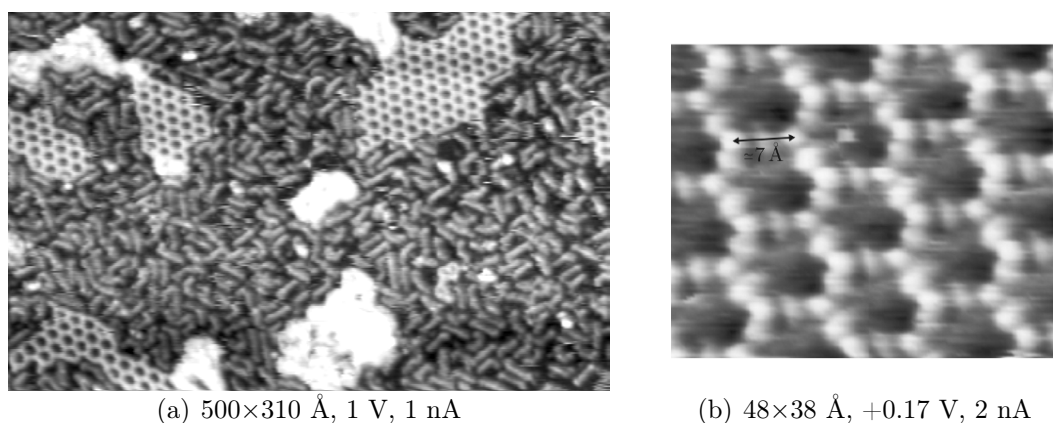


**Figure 4.12.:** STM images of ZnO on Pd(111), with the friendly permission of DI Gunter Weirum.

The proposed structure model is again supported by STM measurements which were done by DI Gunter Weirum. In figure 4.12 STM pictures of ZnO on Pd(111) are shown. One can see from figure 4.12(a) that between areas with an unordered phase there are big ordered areas with a honeycomb-like structure. A detail of the ordered phase is shown in figure 4.12(b) with a higher magnification. Each side of the hexagons consists of three zinc atoms whereas the distance between two atoms is approximately  $3.5 \text{ \AA}$ . This is in a good agreement to the literature where the side length of a unit cell of the ZnO(0001) plane was reported to be  $3.29 \text{ \AA}$ .

## 5. CO on Clean and Zn Modified Pd(111)

*The adsorption and desorption process of CO on Pd(111), Zn modified and ZnO modified Pd(111) have been investigated. The measurement results are shown and discussed. The influence of the surface temperature at which the zinc layer was prepared on the adsorption of CO as well as changes due to different annealing temperatures of the zinc layer are discussed. Furthermore, it is shown that the ZnO layer may be reduced by CO.*

### 5.1. CO on Pd(111)

The adsorption of CO on Pd(111) has been extensively studied before (see [60], [61], [62], [63], [64], [65], [66], [67]).

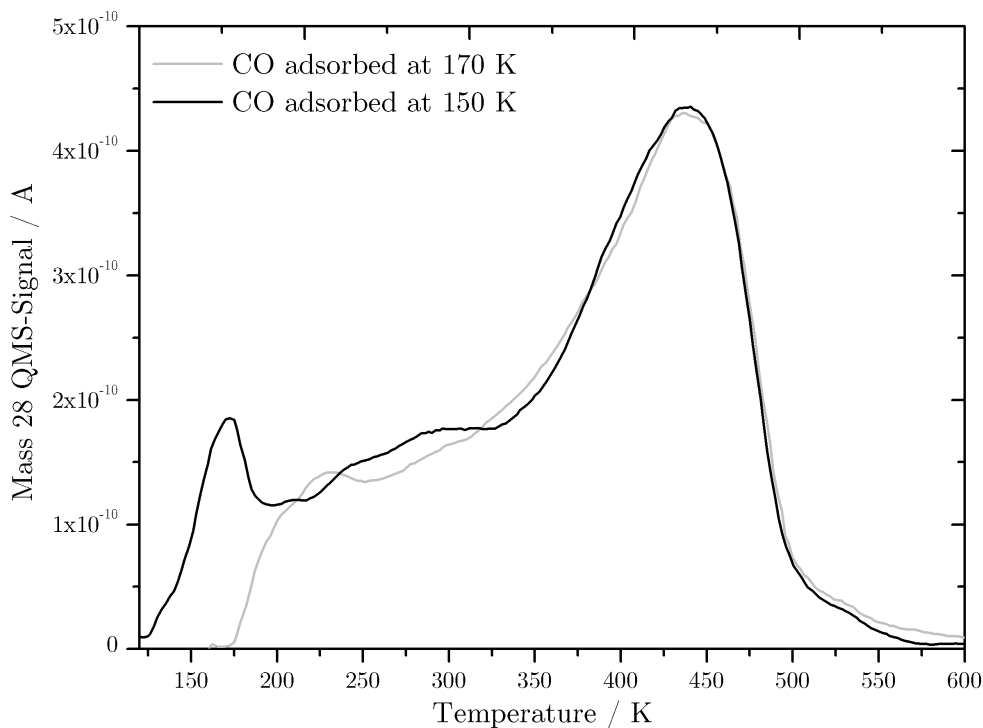


**Figure 5.1.:** TDS of CO (exposure: 85 L) adsorbed on clean Pd(111) at  $T_{Pd} = 170$  K (grey curve) and  $T_{Pd} = 150$  K (black curve); Heating rate: 2K/s;

The grey curve in figure 5.1 shows a TDS of CO that has been adsorbed on clean Pd(111) at a temperature of 170 K. It exhibits a peak maximum at a temperature of 440 K and a broad desorption band extending down to approximately 200 K. At this sample temperature the adsorbed CO gives rise to a  $(2 \times 2)$ -3CO superstructure which corresponds to the saturation coverage of 0.75 monolayer. The structure model (figure 5.2) displays that in each unit cell of the adlayer, highlighted by the rhombus in the figure, one CO molecule occupies an on-top site whereas the two other molecules are bonded to fcc and hcp threefold hollow sites (see [60]).

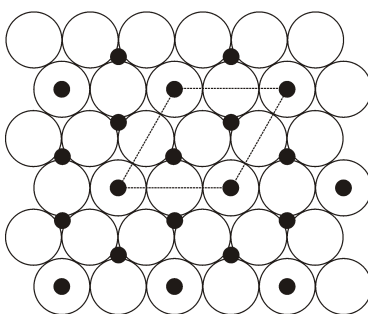


**Figure 5.2.:** Structure model for 0.75 ML CO on Pd(111):

The CO molecules (black circles) form a  $(2 \times 2)$ -3CO superstructure on the Pd surface (white circles).

If the sample temperature is lowered, that is CO is adsorbed on Pd(111) at a temperature of 150 K, a second peak at lower temperature occurs in the TD spectrum (black curve in figure 5.1). This desorption peak with its maximum at 170 K originates from a hollow/on-top to a bridge/on-top phase transition of the adsorbed CO molecules upon desorption (see [61], [66]).

## 5.2. CO on Pd(111)/Zn

First of all a zinc multilayer ( $\approx 10$  monolayer) was prepared on Pd(111) at room temperature. The sample was then exposed to 85 Langmuir CO at 140 K which was followed by thermal desorption. The corresponding TDS is given in figure 5.3

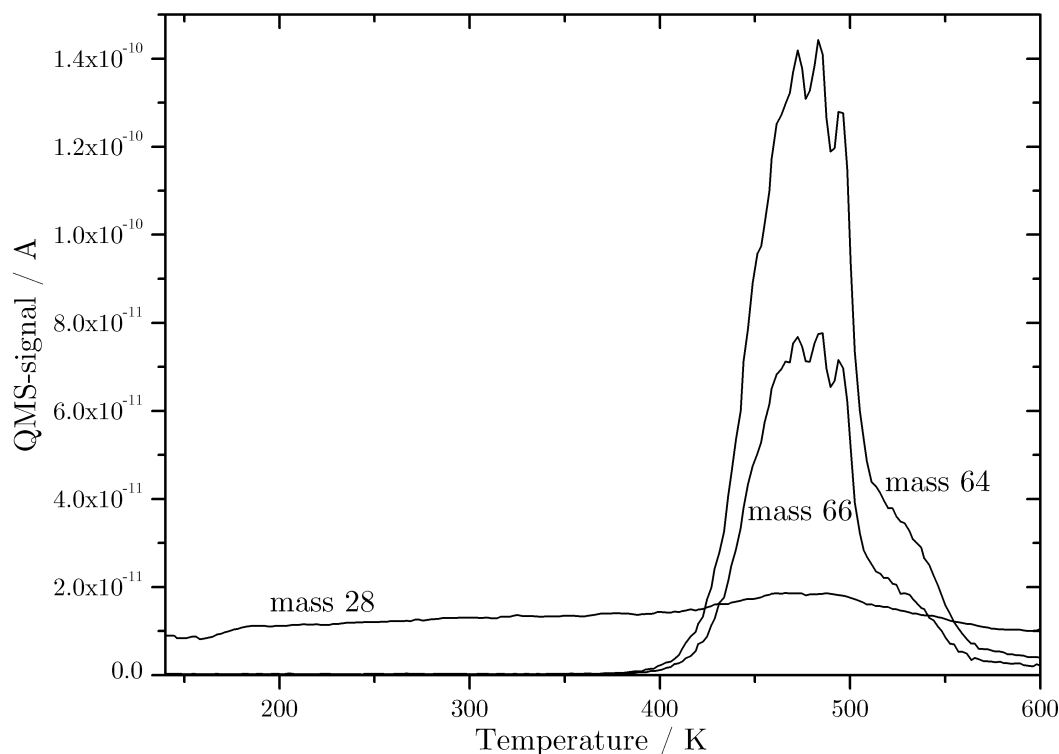


**Figure 5.3.:** TDS of CO (exposure: 85 L) and Zn adsorbed on PdZn with zinc in the multilayer region. Sample temperature  $T_{Pd} = 140$  K; Heating rate: 2K/s;

The QMS-signal shows the desorption of the zinc multilayer (mass isotopes 64 and 66) but there is nearly no evidence for any desorbing CO. The mass 28 signal remains almost constant despite a slight increase at the same temperature at which the multilayer desorbs. Thus the zinc multilayer seems to block completely the adsorption of any CO above 140 K.

Moreover, after desorption of the multilayer, further CO adsorption experiments were carried out. Bayer et al [38] reported that one monolayer of Zn prepared at 373 K is sufficient to block any adsorption of CO at room temperature which could be confirmed in the experiments.

However, when decreasing the adsorption temperature, a new CO desorption peak starts to evolve around 220 K. As was already described in the previous chapter, heating the sample up to 600 K which is necessary to desorb the multilayer, gives rise to the  $(2 \times 1)$  Pd/Zn surface alloy structure. Thus the surface exhibits palladium

sites again but the presence of the zinc atoms obviously lowers the heat of adsorption of CO. Therefore no CO adsorption is observed at room temperature and the CO desorption peak is shifted down to 220 K.

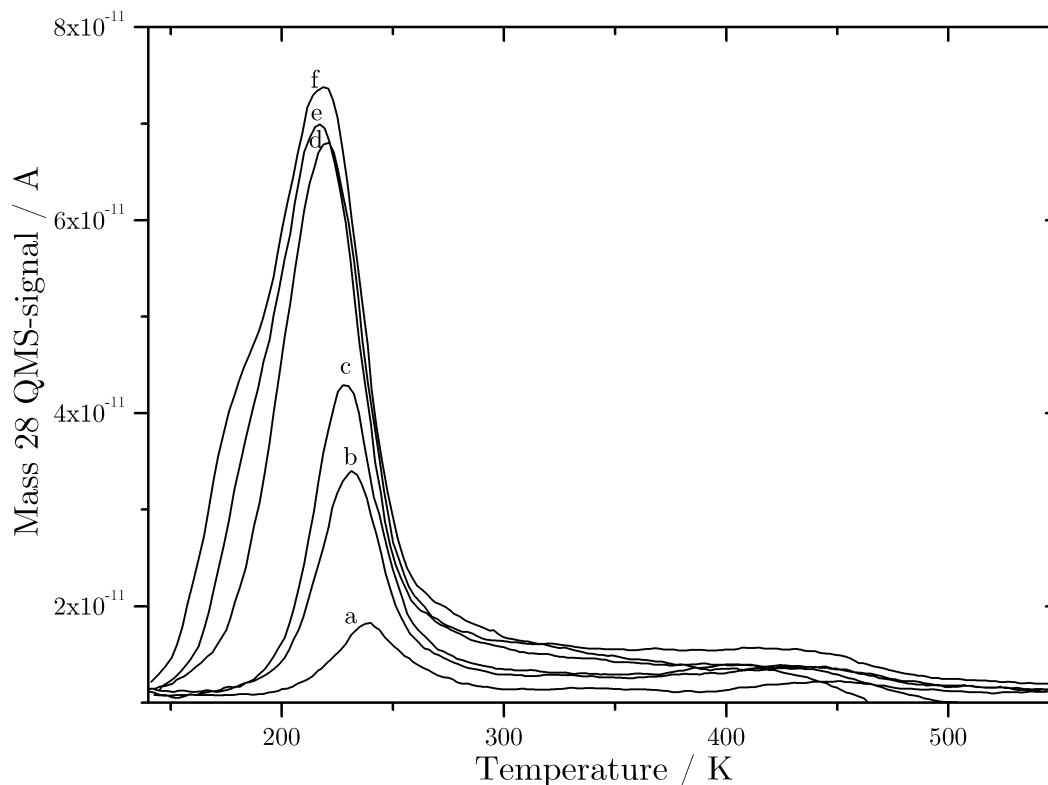


**Figure 5.4.:** Desorption series of CO adsorbed on the Pd/Zn surface alloy using different exposures. Sample temperature  $T_{Pd} \approx 150$  K; Heating rate: 2K/s; Exposures are: (a) 0.05, (b) 0.11, (c) 0.20, (d) 0.34, (e) 0.72, (f) 3.60 L.

In figure 5.4 a desorption series of CO adsorbed on the Pd/Zn surface alloy at a temperature of 150 K is shown. The TDS features a single peak with its maximum shifting from 240 K down to 220 K with increasing CO exposure. Thus the peak may also be distinguished from the low temperature peak at 170 K on clean Pd(111) (figure 5.1).

Figure 5.5 provides the CO coverages obtained by total integration of the TD spectra of figure 5.4 plotted versus the exposure. The peak area is given in terms of monolayer, calculated by comparing the TDS area with those for CO on clean Pd(111) which is known to be 0.75 monolayer.

One can see that the CO coverage increases linearly at the beginning but drops then drastically above a coverage of 0.25 monolayer with increasing exposure. This drop is caused due to the repulsive interaction between the CO ad molecules which comes into play with increasing amount of adsorbed CO. Thus also the decrease in the slope of the curve around a coverage of 0.25 monolayer is plausible: Since the CO molecules are preferably bonded to the Pd on-top sites one can imagine that on

each second Pd atom in a row a CO molecule is bond on top, leaving one Pd atom vacant between two neighbouring CO molecules due to the repulsive interaction of the adatoms. On the Pd/Zn surface alloy this corresponds to a total coverage of 0.25 monolayer.

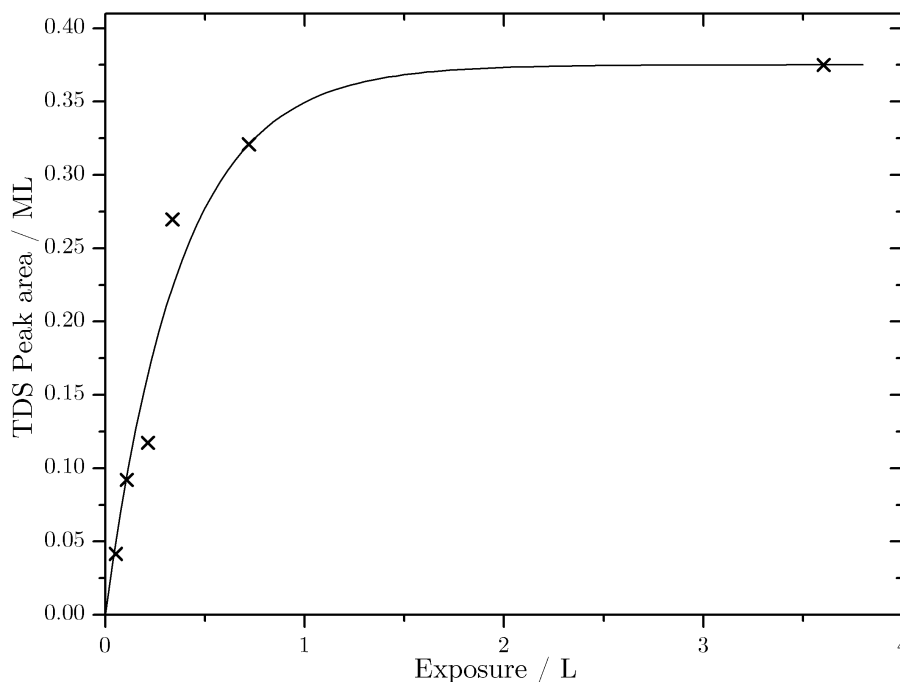


**Figure 5.5.:** TDS peak area of CO adsorbed on the Pd/Zn surface alloy versus exposure.

However, the saturation coverage of adsorbed CO is somewhat larger at about 0.37 monolayer (see figure 5.5). A possible explanation for this could be the following: One CO molecule is bond on top at each third Pd atom of the Pd rows whereas between the two vacant Pd atoms one further CO molecule is bond on a bridge-site which still allows a rather large distance between the neighbouring CO molecules. Thus each Pd-row of the surface alloy is occupied with CO molecules by 2/3 giving rise to a total coverage of 1/3 on the surface.

Since the adsorption of CO was shown to be non-dissociative a desorption according to first order may be assumed. The adsorption energy may then be calculated according to the Redhead concept (equation 2.21) with  $\beta = 2 \text{ K}\cdot\text{s}^{-1}$  and  $\nu = 10^{13} \text{ s}^{-1}$ . The obtained desorption energies are plotted in figure 5.6 versus the coverage.

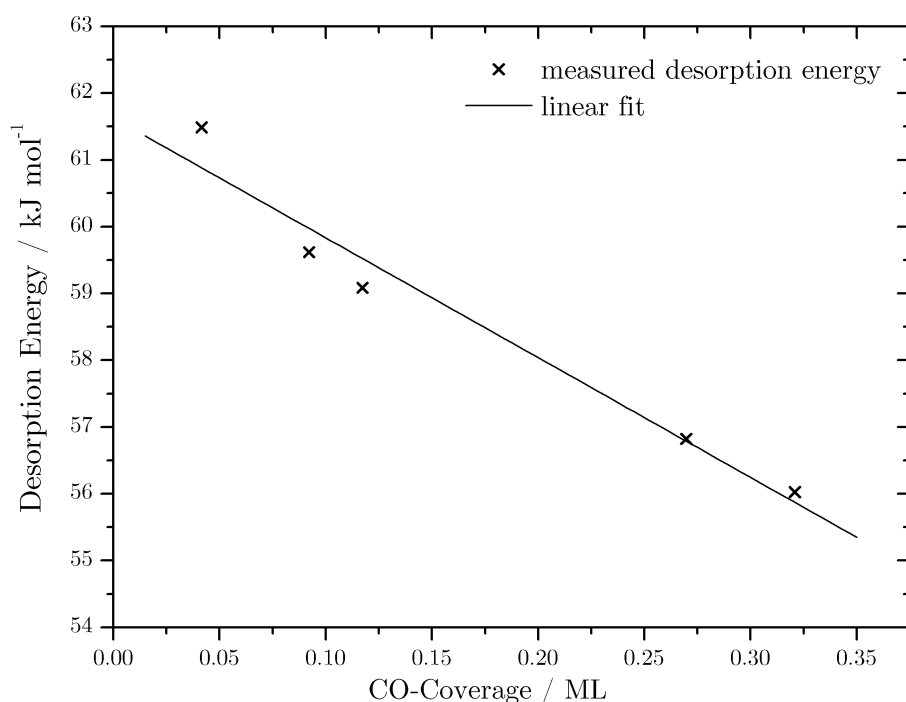


**Figure 5.6.:** Desorption energy of CO on the Pd/Zn surface alloy versus coverage.

There is a linear decrease in the desorption energy with increasing coverage which is again caused by the repulsive interaction between the CO admolecules. Thus the desorption energy is no longer independent of the coverage.

At low coverages the desorption energy equals  $62 \pm 2 \text{ kJ mol}^{-1}$ . As already described in the theory section 2.9, the Pd-Zn interaction weakens the strength of the Pd-CO bonding which gives rise to a reduction in the adsorption energy of CO. Furthermore, theoretical calculations indicated that the palladium density of states (DOS) in the PdZn alloys is similar to the DOS of copper (see section 2.7.3).

This is supported by the CO experiments, because TD spectra of CO adsorbed on copper showed similar desorption energies. For instance Harendt et al [68] reported a desorption energy of  $53 \text{ kJ mol}^{-1}$  for CO on Cu(110) and Vollmer et al [69] a desorption energy of  $47 \text{ kJ mol}^{-1}$  for CO on Cu(111) at lower coverages.

### 5.2.1. Influence of different Zn Layer Preparation Methods on the CO Adsorption

To get further information about the growth of the zinc layer and especially about the influence of the surface temperature when depositing zinc further CO adsorption experiments were carried out whereas the zinc layer was prepared at different temperatures.

In figure 5.7 TD spectra of CO adsorbed on Pd/Zn which was prepared at 150 K are shown with increasing amount of deposited zinc. Each TDS was obtained after 34 L of CO had been adsorbed at 150 K on the Pd/Zn surface. The corresponding zinc coverages are given in the figure.

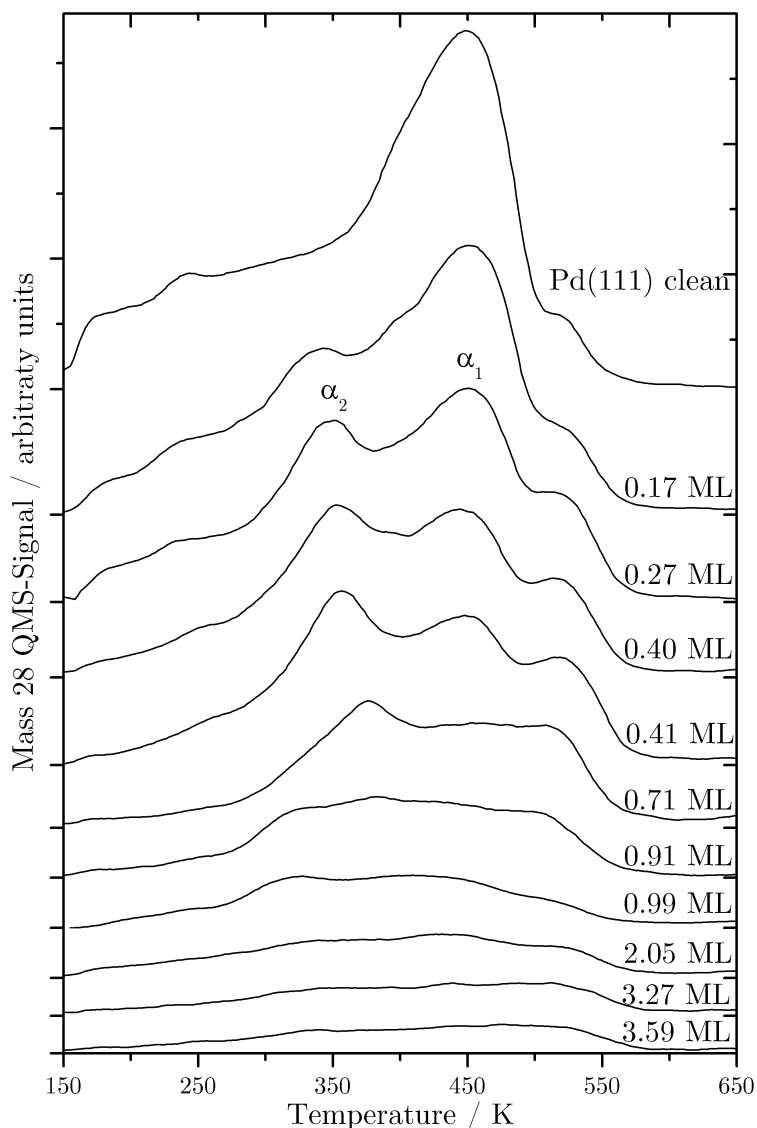


**Figure 5.7.:** Desorption series of CO (exposure: 34 L,  $T_{Pd} = 150$  K) adsorbed on Pd/Zn with increasing zinc coverage. The zinc layer was prepared at  $T_{Pd} = 150$  K. Heating rate: 2K/s

One sees that the desorption maximum (peak  $\alpha_1$ ) which occurs at 440 K on clean Pd remains at this temperature but becomes smaller and smaller with increasing zinc coverage. At low amounts of deposited zinc a second peak around 350 K ( $\alpha_2$ ) starts to evolve which gets then smaller again with further increasing zinc coverage. At a coverage of approximately 1 ML the amount of adsorbed CO becomes very small. Above this coverage there are hardly any changes in the CO TDS spectra.

Interestingly there appears a shoulder in the CO spectrum on clean palladium at about 520 K which always remains there even in the TDS with high zinc coverages. Due to the fact that the area of the CO QMS-signal in the main chamber, which was obtained during the TDS measurements, is up to 20% of the area of the line of sight signal this shoulder may be caused by mixing with the offline signal. This would also explain the effect that the CO signal does not go completely down to zero at high zinc coverages.

The same experiments were performed again, whereby the zinc layer was now prepared at 300 K. The obtained TDS are provided in figure 5.8.

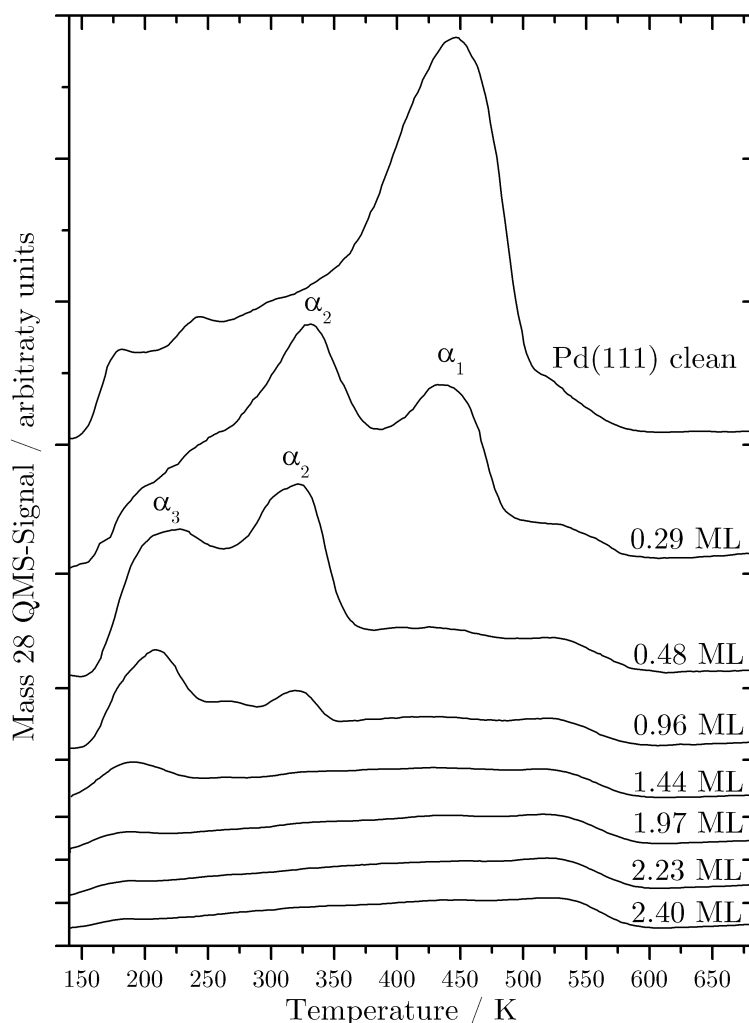


**Figure 5.8.:** Desorption series of CO (exposure: 34 L,  $T_{\text{Pd}} = 150$  K) adsorbed on Pd/Zn with increasing zinc coverage. The zinc layer was prepared at  $T_{\text{Pd}} = 300$  K. Heating rate: 2K/s

Compared to the spectra where the zinc layer was prepared at 150 K (figure 5.7) the  $\alpha_1$ -peak is now already suppressed at lower zinc coverages. At the same time two further peaks develop: Peak  $\alpha_2$  which was already observed at 150 K and a new one around 210 K which will be referred as  $\alpha_3$ . Again there is hardly any CO adsorption

above a Zn coverage of approximately 1 ML mainly leaving the above mentioned shoulder around 520 K

Furthermore, the CO adsorption experiments were carried out once more with the zinc layer prepared at 350 K which is believed to be a high enough temperature to give rise to the Pd/Zn surface alloy. Figure 5.9 displays the corresponding TDS.

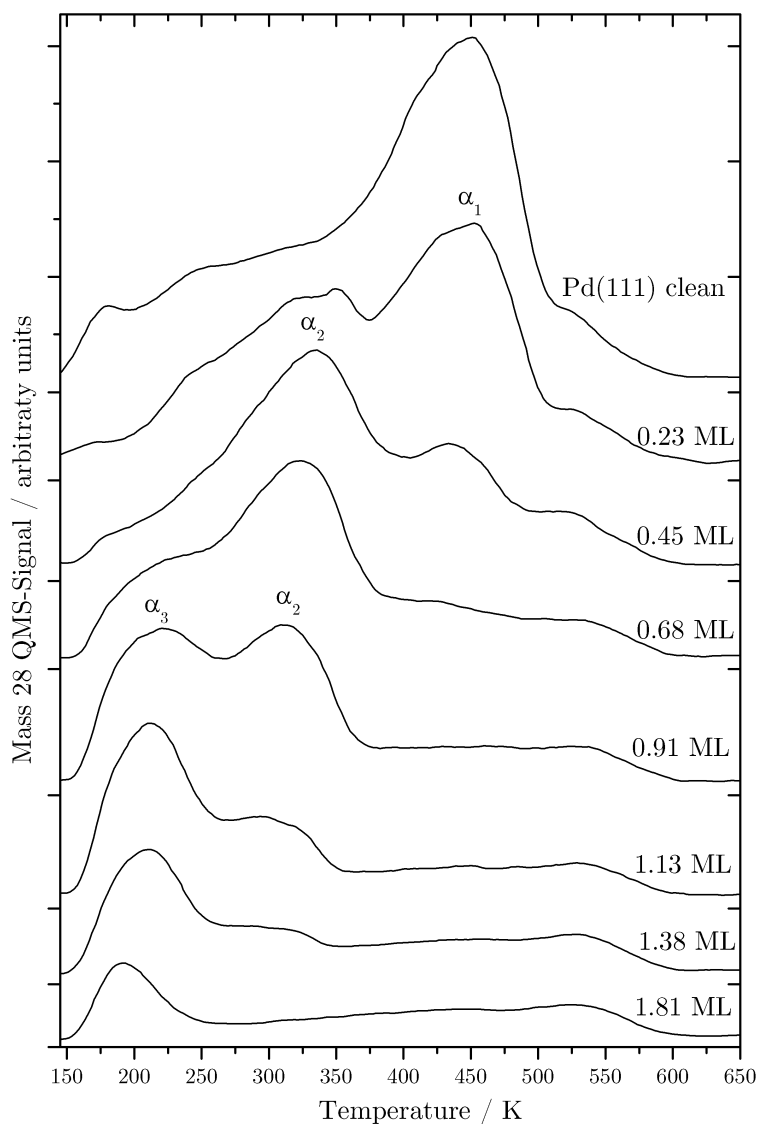


**Figure 5.9.:** Desorption series of CO (exposure: 34 L,  $T_{Pd} = 150$  K) adsorbed on Pd/Zn with increasing zinc coverage. The zinc layer was prepared at  $T_{Pd} = 350$  K. Heating rate: 2K/s

The peak maximum of CO on clean Pd(111),  $\alpha_1$ , is again suppressed at rather low zinc coverages. The two peaks  $\alpha_2$  at 330 K and  $\alpha_3$  at 210 K appear once more. However the  $\alpha_2$ -peak remains even at zinc coverages above 1 ML. Due to the desorption temperature it may be allocated to the low temperature CO peak which was observed on Pd/Zn after the zinc multilayer had been flashed away (figure 5.4).

Obviously the different CO desorption peaks are due to CO adsorbed on different sites. Let us now summarize the results of the above mentioned desorption spectra. A possible explanation model is drawn in figure 5.10.

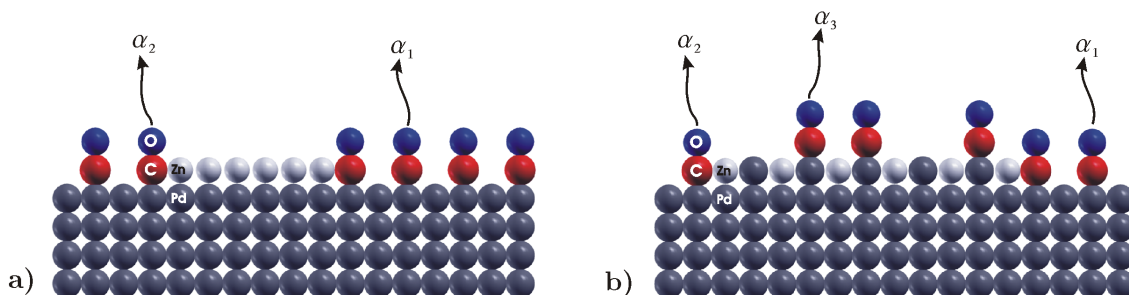


**Figure 5.10.:** Structure model for CO adsorption and desorption on differently prepared zinc layers:

- Pd/Zn prepared at 150 K: Zn islands are formed, CO adsorbed on "normal" Pd sites (desorption  $\alpha_1$ ) and on Pd sites at the islands edges (desorption  $\alpha_2$ )
- Pd/Zn prepared at 350 K: Formation of the Pd/Zn surface alloy, CO adsorbed on "normal" Pd sites (desorption  $\alpha_1$ ), on Pd sites at islands edges (desorption  $\alpha_2$ ) and on the Pd sites of the surface alloy (desorption  $\alpha_3$ )

When the zinc layer is prepared at 150 K (figure 5.10a) zinc islands are formed at lower coverages. Thus the CO adsorption is possible on the "normal" Pd sites on the uncovered surface regions which causes the  $\alpha_1$ -peak in the TDS. Despite that the CO molecules may adsorb on Pd sites which are at the edge of a zinc island. Due to the present zinc and its change on the electronic structure of the palladium atoms (section 2.9) the CO molecules are less strongly bond and they desorb at lower temperatures (desorption peak  $\alpha_2$ ).

If the zinc layer is prepared at 350 K the Pd/Zn surface alloy will be formed. At low coverages (figure 5.10b) the same CO adsorption sites as in the before mentioned case are present giving rise to the  $\alpha_1$ - and  $\alpha_2$ -peak in the TDS. In addition there is also the possibility for the CO molecules to adsorb on Pd atoms of the Pd/Zn surface alloy. In this case the CO molecules are weakest bond and thus desorb at even lower temperatures (desorption peak  $\alpha_3$ ) than the molecules at the edges.

It is also clearly seen in the picture why the  $\alpha_1$  peak is already suppressed at lower coverages when the zinc layer is prepared at 350 K: Due to the surface alloy formation less "normal" Pd sites are available than compared to a zinc layer with the same coverage that was prepared at 150 K. This also explains why the  $\alpha_2$  peak is more enhanced on the layer prepared at 350 K. The edges between the surface alloy region and the palladium substrate are longer than the zinc island edges (at 150 K) given the same zinc coverage.

Finally in figure 5.11 the amount of adsorbed CO as a function of the zinc coverage for the different temperatures at which the zinc layer were prepared are shown.

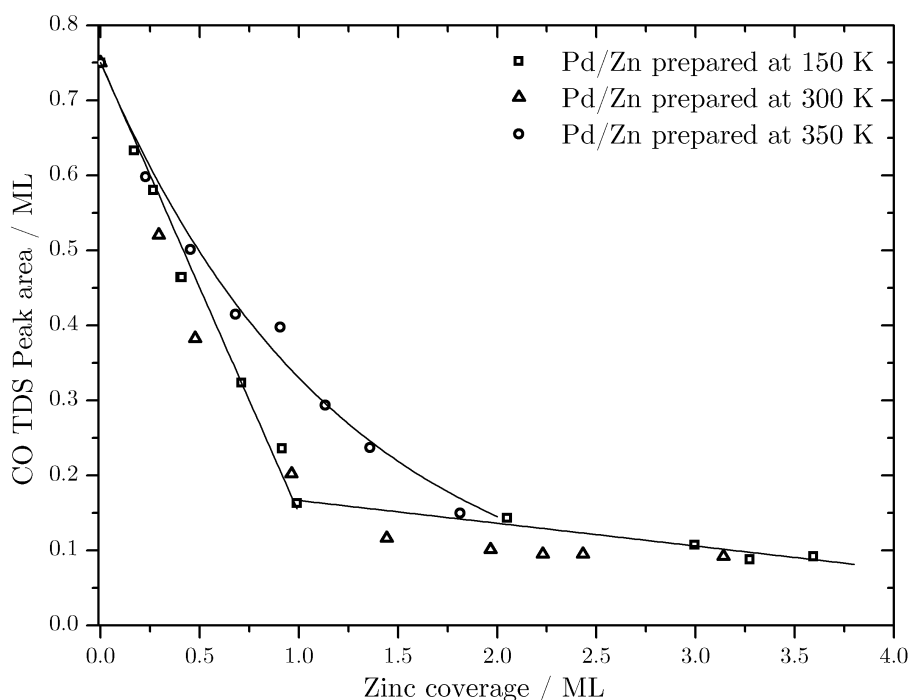


**Figure 5.11.:** TDS peak area of CO (exposure: 34 L) adsorbed on PdZn versus zinc coverage. The zinc adlayer were prepared at 150 K, 300 K and 350 K respectively.

The curves of the zinc layer prepared at 150 and 300 K indicate a strong linear descent in the beginning but drop then suddenly to a much smaller linear decrease at a zinc coverage of about 1 monolayer. The Zn layer which was prepared at 350 K exhibits a different behaviour, so the curve does not show a kink. The amount of adsorbed CO decreases according to an exponential decay.

It is clear that the difference in the curves is caused due to the morphology of the zinc layers. Thus at 350 K the temperature is high enough to allow the formation of the Pd/Zn surface alloy. Hence the adsorption of CO is possible on free Pd sites outside the alloy phase as well as on the Pd sites of the  $(2 \times 1)$  surface alloy. On the other hand, at 150 K zinc islands are formed which block the adsorption of CO molecules and CO may only adsorb outside the islands on free Pd sites of the substrate.

So far we have looked at the formation of the Pd/Zn surface alloy and surface temperatures up to 350 K but we want to treat now the influence of higher temperatures on the zinc layer. Figure 5.12 provides CO TPD spectra on Pd/Zn whereas the zinc layer was annealed at different temperatures.

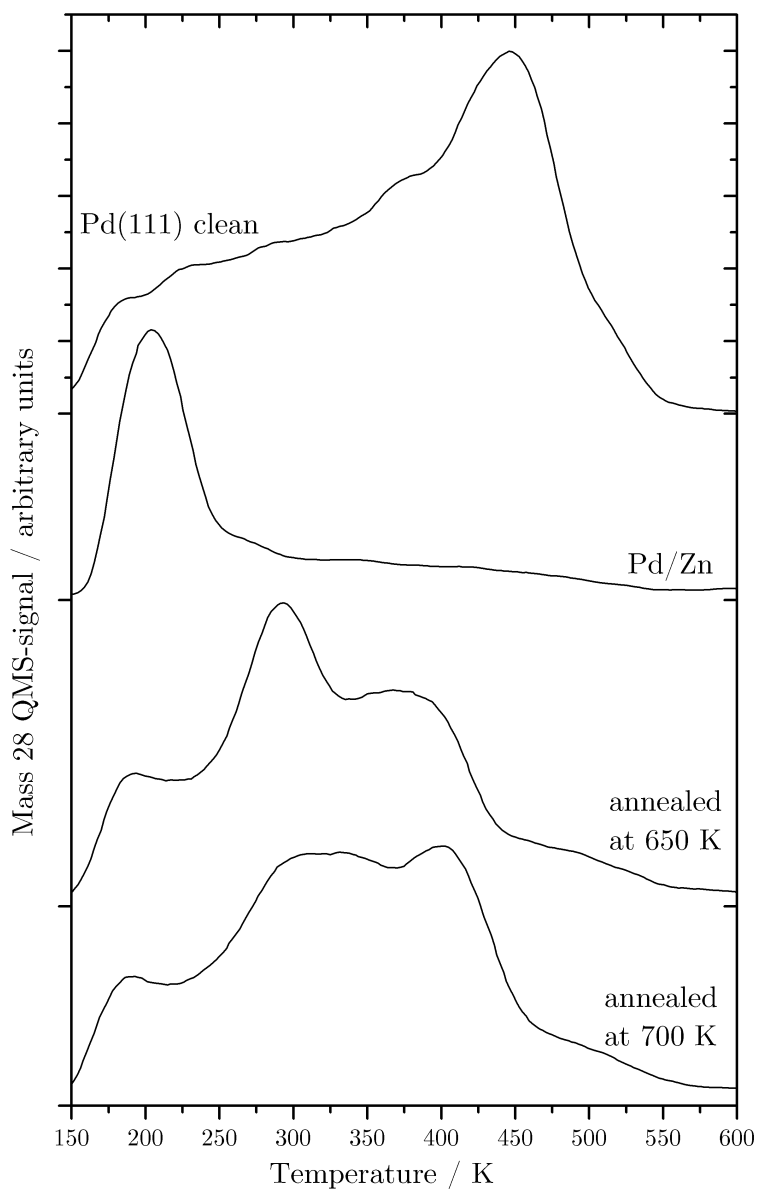


**Figure 5.12.:** CO TDS after annealing the zinc adlayer at different temperatures. CO exposure: 85 L at  $T_{Pd} = 150$  K; Heating rate: 2K/s

The second TDS was obtained after a zinc multilayer had been flashed away by heating up to 600 K and it exhibits the typical low temperature CO desorption peak. Annealing of this prepared zinc layer at 650 K for 10 minutes gives rise to a change in the CO TD spectrum (third curve). The desorption peaks differ from those on zinc layers that had been prepared at lower temperatures (figures 5.7-5.9). Moreover, a decrease of the Zn/Pd ratio in the Auger signal by approximately 12%

was observed after the annealing.

The fact that this drop in the AES signal comes along with the changes in the CO TDS is an evidence that zinc atoms start to migrate in the subsurface region. Thus the surface holds more Pd sites again after the annealing which gives rise to stronger Pd-CO bonds and a shift of the TDS peak maximum to higher temperatures. However, it is also possible that the diffusing Pd atoms segregate on top of the zinc.

Further annealing of the surface at a temperature of 700 K for 10 minutes causes again migration of zinc atoms in the subsurface region. This is indicated by an additional decrease of 8% in the Zn/Pd ratio of the Auger signal and changes in the CO TDS (fourth curve in figure 5.12).

### 5.3. CO on Pd(111)/ZnO

It has already been described in chapter 4 that the preparation of a ZnO layer on Pd(111) gives rise to a  $(6 \times 6)$  superstructure. This ZnO layer may be reduced by sequential dosing and desorbing CO via the formation of  $\text{CO}_2$ . The obtained TD spectra of CO and  $\text{CO}_2$  after adsorbing CO on Pd/ZnO are shown in figure 5.13. Therefore CO was adsorbed on the sample (sample temperature  $T_{\text{Pd}} \approx 130$  K, exposures are given in the figure) and then desorbed again by heating the sample up to 640 K with a heating rate of 2 K/s.

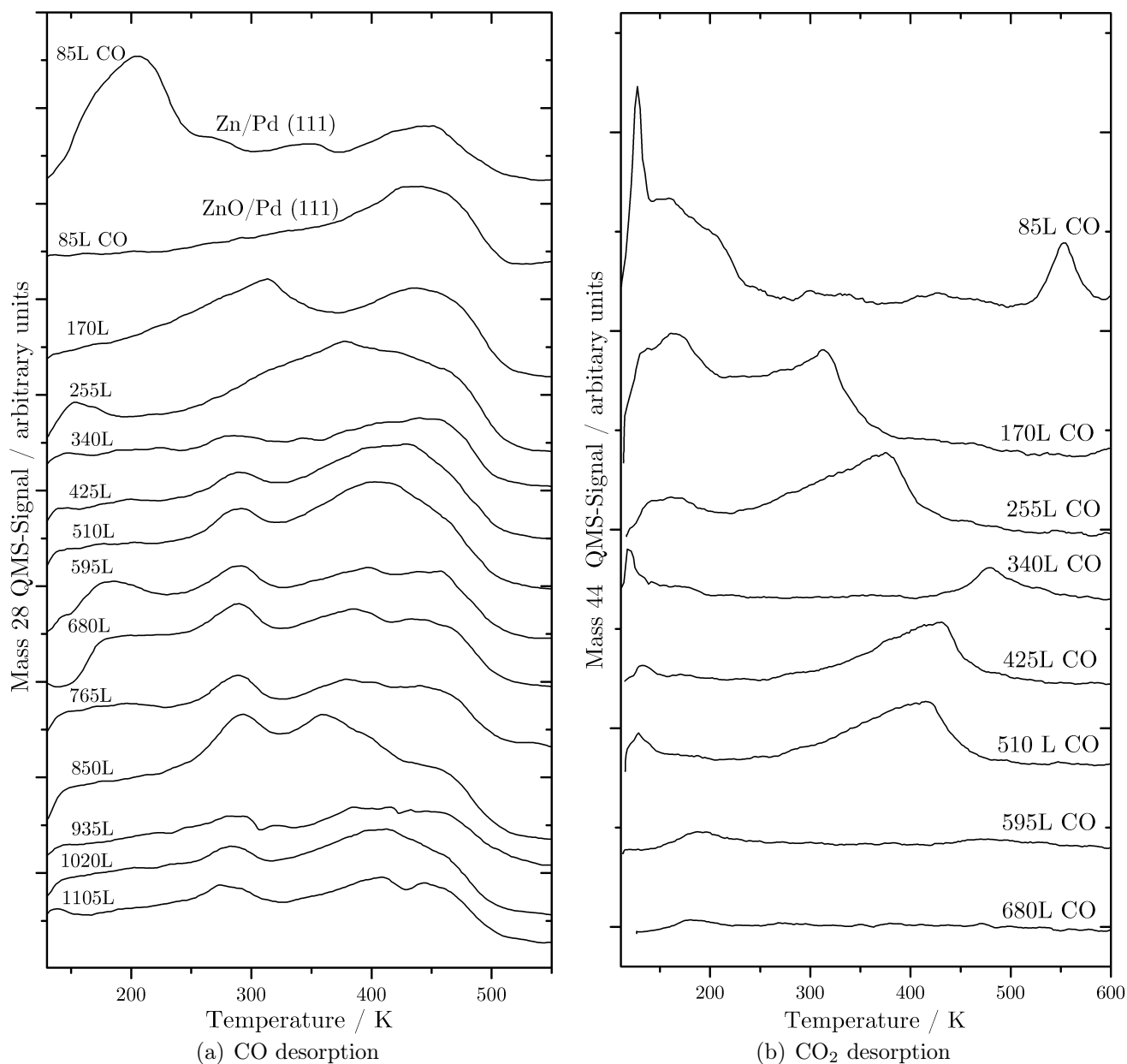


**Figure 5.13.:** Change of the CO and  $\text{CO}_2$  TD spectra with the CO adsorption cycles. Note that the scale of the  $\text{CO}_2$  signal is about 6 times smaller!

The topmost TD spectrum in figure 5.13(a) displays the desorption of CO adsorbed on a Pd(111) sample which was partially covered by Zn. It features again the low temperature peak at a temperature of 205 K. Since the Pd surface is not fully covered with zinc, the peak at 440 K is still present but much smaller than on clean palladium (figure 5.1). After oxidizing and preparing the ZnO layer, the low temperature peak in the TDS (spectrum 2) has completely vanished, whereas the peak at 440 K is more enhanced which gives rise to a spectrum that is rather similar to the one of CO adsorbed on clean Pd(111).

The topmost spectrum in figure 5.13(b) shows the corresponding CO<sub>2</sub>-signal which was recorded at the same time. It exhibits a very sharp peak at 130 K and a second peak at 550 K. Since no preadsorption of CO<sub>2</sub> was carried out, it is rather likely, that the ZnO on the surface is reduced, supporting a second oxygen atom to the adsorbed CO molecule, which is then desorbing as CO<sub>2</sub>.

With increasing number of CO desorption cycles the TDS undergo a change. A second peak around 290 K evolves and the high temperature peak starts to shift from 450 K down to 400 K. Due to the successive heating of the sample up to 650 K in each desorption cycle, Zn starts to migrate into the Pd substrate giving rise to the formation of a subsurface alloy and further changes in the TD spectra (see [40], [70], [67]). In fact the last CO desorption spectra of figure 5.13(b) look kind of similar to the desorption spectra on the annealed Pd/Zn sample (figure 5.12).

In the CO<sub>2</sub> spectra first the high and then the low temperature peak start to disappear but a new single peak around 420 K starts to evolve. After 7 to 8 CO desorption cycles the CO<sub>2</sub> signal has completely vanished which indicates that the ZnO layer has been fully reduced by CO, leaving solely Zn on the surface.

This is further approved by the Auger data which are shown in figure 5.14. The figure provides the peak to peak ratios in the AES spectra of Zn/Pd, O/Pd and O/Zn.

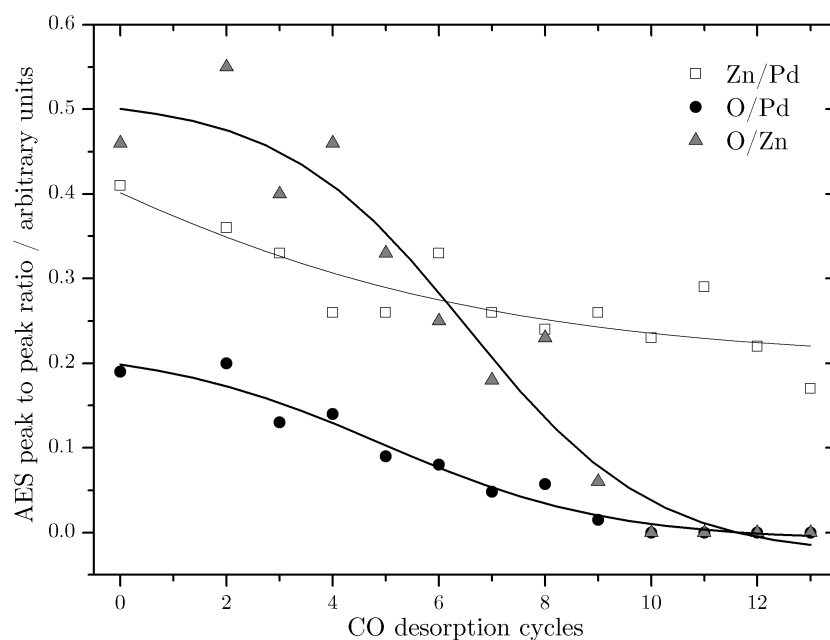
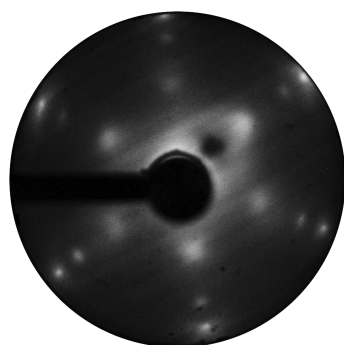
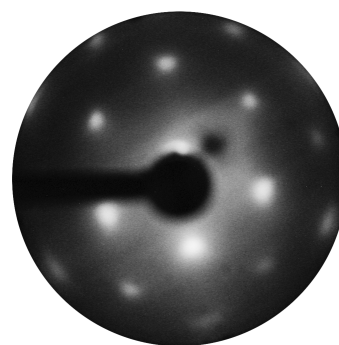


**Figure 5.14.:** Change of the peak to peak ratios in the AES with increasing number of CO desorption cycles. The plotted ratios are based on the heights of the Auger-signals of Zn at 59 eV, Pd at 330 eV and O at 510 eV.

The rather step decay in the O/Pd and O/Zn peak to peak ratios with increasing desorption cycles indicates a loss of oxygen which is due to the formation of  $\text{CO}_2$ . After 9 CO desorption cycles there is no evidence for the presence of oxygen in the Auger-spectra any more. The curve of the Zn/Pd ratio exhibits a decay as well, though it is much smoother. Thus it verifies the migration of Zn atoms into the bulk due to the high desorption temperatures.



(a) After 3 CO desorption cycles  
beam energy: 55eV



(b) After 8 CO desorption cycles  
beam energy: 62eV

**Figure 5.15.:** Change of the Pd/ZnO LEED pattern after several CO desorption cycles

The gradual change of the surface structure during this procedure is further in-

indicated by the LEED pictures. Starting from the  $(6\times 6)$  superstructure the LEED pattern starts to change and after 3 CO desorption cycles figure 5.15(a) is observed. After 8 CO desorption cycles the LEED pattern shows a clear  $(2\times 2)$  pattern (figure 5.15(b)) corresponding to the earlier described  $p(2\times 1)$  superstructure of the Pd/Zn surface alloy including the domains.

The processes that take place on the surface are summarized and illustrated in figure 5.16.

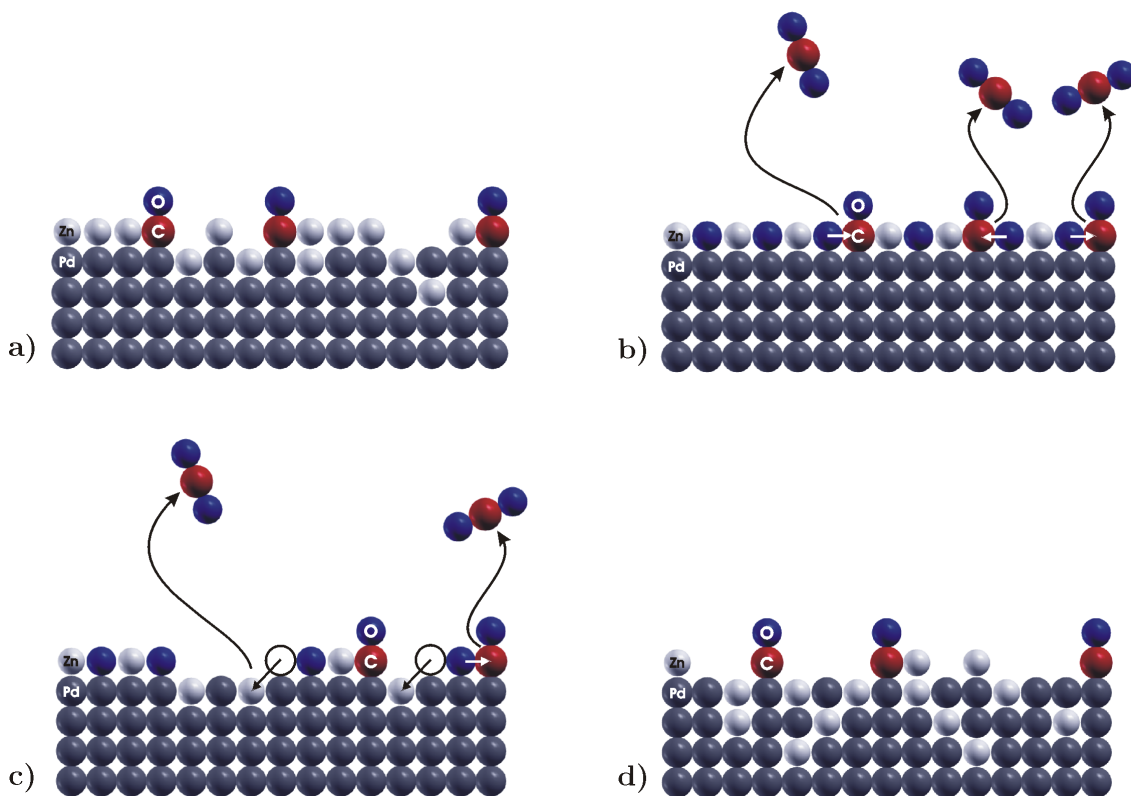


**Figure 5.16.:** Structure model of the reduction of Pd/ZnO by CO:

- Zn on Pd(111): The CO adsorption on free Pd sites is still possible.
- ZnO on Pd(111): Reduction of ZnO by CO due to formation of  $\text{CO}_2$ .
- After several CO desorption cycles: Further ZnO reduction and formation of a Pd/Zn subsurface alloy.
- After 10 CO desorption cycles: The ZnO is fully reduced and the Pd/Zn alloy formation is further enhanced.

## 6. Adsorption and Desorption of $H_2$ on Clean and Zn Modified Pd(111)

*This chapter provides the adsorption of  $H_2$  on Pd(111) and Zn modified Pd(111). The change of the  $H_2$  TDS after depositing zinc on the surface is described. In addition it is shown that the ZnO layer may be reduced by  $H_2$  via the formation of  $H_2O$ .*

### 6.1. Hydrogen on Clean Pd(111)

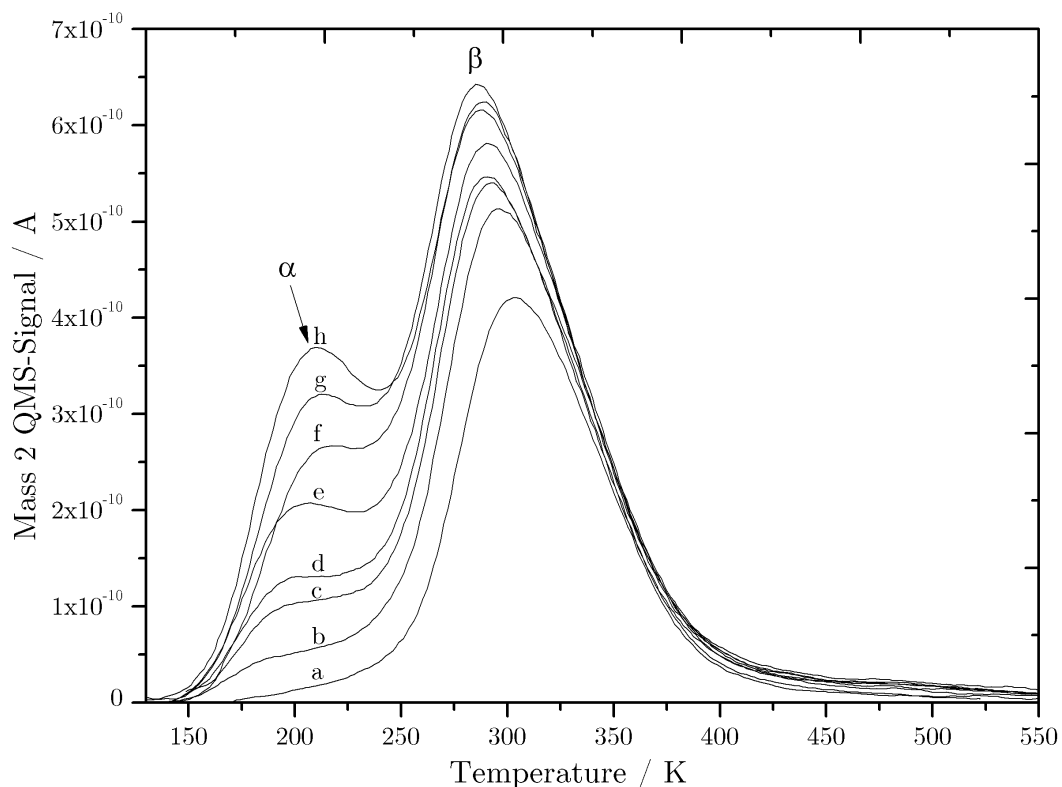


**Figure 6.1.:** TDS of  $H_2$  adsorbed on clean Pd(111) using different exposures; Sample temperature  $T_{Pd} \approx 150K$ ; Heating rate:  $2K/s$ ; Exposures are: (a) 1, (b) 11, (c) 38, (d) 54, (e) 108, (f) 173, (g) 345, (h) 518 L.

The H<sub>2</sub> TPD spectra were obtained after subsequent dosing of H<sub>2</sub> onto the clean Pd(111) surface whereas the palladium sample was held at 150K. The TPD spectra for different exposures of H<sub>2</sub> are shown in figure 6.1.

For low exposures the hydrogen exposure leads only to a saturation of the chemisorbed surface layer without any penetration into the bulk material. Thereby the hydrogen is absorbed in the atomic state forming a true (1×1) structure. During the desorption the chemisorbed atomic hydrogen forms a molecular transition state H<sub>2(ad)</sub> which then desorbs immediately into the gas phase H<sub>2</sub> due to the small binding energy (see [45], [43]). The corresponding desorption peak appears with the peak maximum at 305 K and is referred as  $\beta$ -peak in the literature.

Increasing exposures give rise to a second TPD peak,  $\alpha$ , with the peak maximum at temperatures around 200 K which is below the desorption temperature of chemisorbed hydrogen. The more the exposure is increased, the more the  $\alpha$ -peak grows (curve b-h in figure 6.1) without the appearance of any saturation, indicating the diffusion of hydrogen into the bulk. Thus the  $\alpha$ -peak originates from the desorption of hydrogen in the near surface region (see [71]).

In addition the temperature of the  $\beta$ -peak shifts with increasing exposure towards lower temperatures from 305 K to 285 K which is due to the second order kinetics of associative molecular desorption. Furthermore the desorption of  $\beta$  is slightly enhanced as  $\alpha$  develops, which might be due to an overlap with the increasing  $\alpha$ -peak.

## 6.2. Hydrogen on Pd(111)/Zn

Starting once more with the preparation of a thick zinc multilayer ( $\approx 10$  ML) on Pd(111) this layer is sufficient to block the adsorption of hydrogen. If the multilayer is flashed away, which causes the formation of the Pd/Zn surface alloy, the situation is different. In figure 6.2 the corresponding series of TPD for different exposures of H<sub>2</sub> are provided.

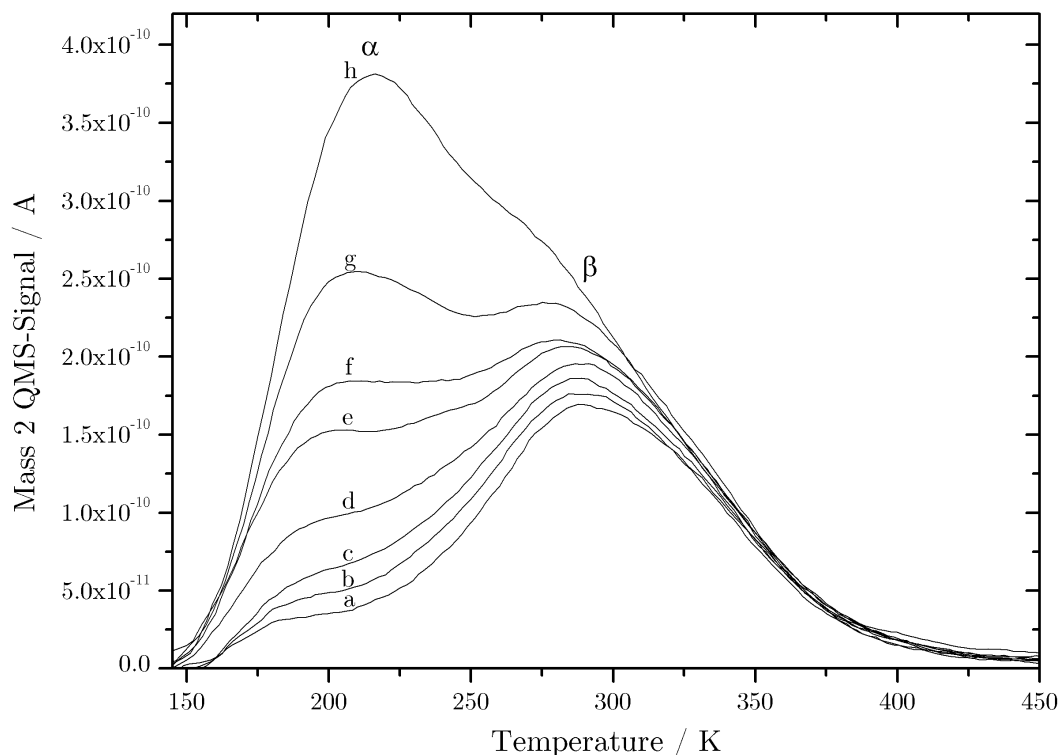


**Figure 6.2.:** TDS of H<sub>2</sub> adsorbed on Pd/Zn (flashed up to 600 K) with different exposures;  $T_{Pd} \approx 150$ K; Heating rate: 2K/s; Exposures are: (a) 2, (b) 7, (c) 11, (d) 35, (e) 85, (f) 108, (g) 216, (h) 864 L.

One sees that both the surface and the subsurface peak still exist and occur at the same temperature as on clean Pd (figure 6.1). However, the surface peak is much smaller whereas the subsurface peak does not seem to be influenced. This indicates that the Zn on the surface does not give rise to any energetic changes but to a change in the number of adsorption sites.

This seems to be plausible since on the Pd/Zn surface alloy less Pd sites are available to the hydrogen atoms than compared to the clean Pd surface which causes the smaller  $\beta$ -peak. In fact half of the surface is covered with zinc due to the  $(2 \times 1)$  superstructure of the surface alloy. This is confirmed by the fact that the area of the  $\beta$ -peak in the TD spectra and thus the amount of adsorbed hydrogen on the Pd/Zn surface alloy is 45% of the amount adsorbed on clean Pd(111). At the same time diffusion of hydrogen in the Pd bulk is still possible and hence the  $\alpha$ -peak grows with increasing exposure.

### 6.3. Hydrogen on Pd(111)/ZnO

The prepared ZnO layer (see chapter 4) may be reduced by sequential dosing and desorbing H<sub>2</sub> via the formation of H<sub>2</sub>O. Figure 6.3 displays the obtained TD spectrum of H<sub>2</sub> and H<sub>2</sub>O after H<sub>2</sub> with an exposure of 1000 L had been adsorbed on Pd/ZnO. The TDS exhibits a clear water desorption peak at a temperature of 170 K. The peak area is in fact too big to be just due to the formation of H<sub>2</sub>O with the adsorbed H<sub>2</sub>, nevertheless the Auger and LEED data verify that the desorbing H<sub>2</sub> forms H<sub>2</sub>O thus reducing the ZnO on the surface.

In the H<sub>2</sub> signal itself a peak at 280 K occurs which is rather similar to the surface peak on clean Pd(111). The second peak which occurs together with the water desorption peak at 170 K is caused by water which is cracked when entering the ion source of the QMS. The shoulder at 200 K is due to adsorbed H<sub>2</sub>O of the residual gas.

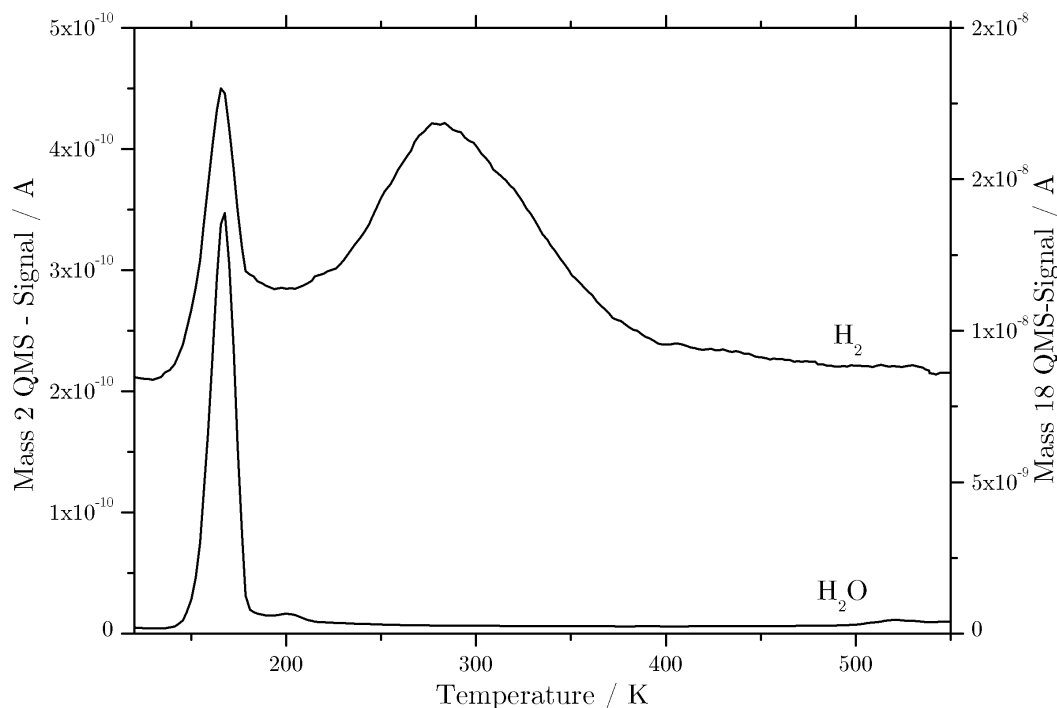


**Figure 6.3.:** TD spectrum of hydrogen adsorbed on Pd/ZnO:

H<sub>2</sub> exposure: 1000 L, sample temperature  $T_{Pd}$ =130K, heating rate = 2 K/s

The gradual change of the surface may be followed by sequential dosing and desorption of hydrogen in several cycles. Thus H<sub>2</sub> with an exposure of 216 L is adsorbed at 130 K and then desorbed by heating the sample up to 600 K in each cycle. After each desorption cycle a LEED and an Auger-spectrum were taken. Both attest clearly that the ZnO layer is reduced. The (6×6) superstructure in the LEED pattern vanishes slowly (see figure 6.4) and is then replaced by a (2×2) pattern after 5 desorption cycles, which is a strong indication for the (2×1) Pd/Zn surface alloy.

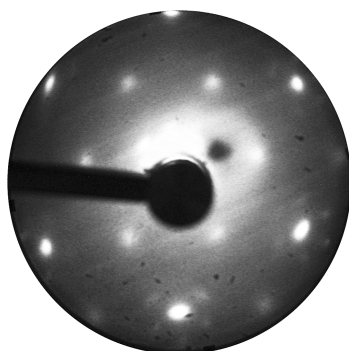


**Figure 6.4.:** ZnO after 2 H<sub>2</sub> desorption cycles, beam energy: 42eV

The corresponding AES peak to peak ratios of Zn/Pd, O/Pd and O/Zn which were obtained after each desorption H<sub>2</sub> cycle are provided in figure 6.5.

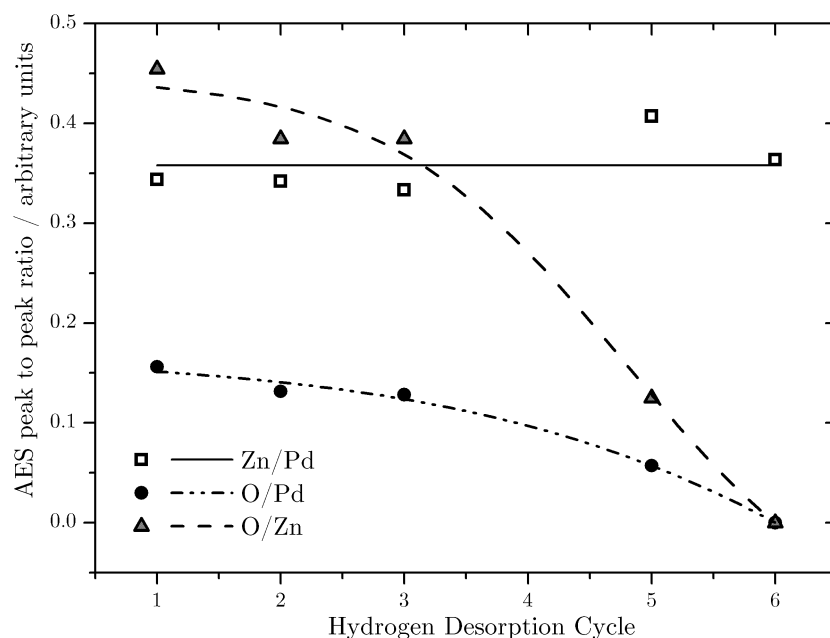


**Figure 6.5.:** Change of the peak to peak ratios in the AES with increasing number of H<sub>2</sub> desorption cycles (exposure: 216 L). The plotted ratios are based on the heights of the Auger-signals of Zn at 59 eV, Pd at 330 eV and O at 510 eV.

The O/Pd and O/Zn peak to peak ratios show a decay with increasing number of H<sub>2</sub> desorption cycles. This indicates a loss of oxygen which is due to the formation of H<sub>2</sub>O. After 6 H<sub>2</sub> desorption cycles the oxygen is not detectable in the Auger-spectra anymore. The ratio of Zn/Pd stays constant, verifying that the zinc atoms stay on the surface and do not migrate into the bulk. Thus the temperature when desorbing hydrogen is not high enough to allow the formation of a Pd/Zn alloy.

# 7. Adsorption and Desorption of Sequentially Dosed H<sub>2</sub> and CO on Pd(111)

*In this chapter the adsorption and desorption process of sequentially dosed H<sub>2</sub> and CO on Pd(111) are described. It is shown that preadsorbed CO impedes the adsorption of H<sub>2</sub>. In addition CO adsorbed after dosing H<sub>2</sub> hinders the hydrogen desorption at low temperatures.*

## 7.1. CO Followed by H<sub>2</sub>

The Pd(111) surface was saturated with CO by cooling the sample in  $1.4 \times 10^{-7}$  Torr from 300 to 115 K, corresponding to a total exposure of 145 L. This was followed by a H<sub>2</sub> exposure of 216 L whilst the sample was held at 115 K.

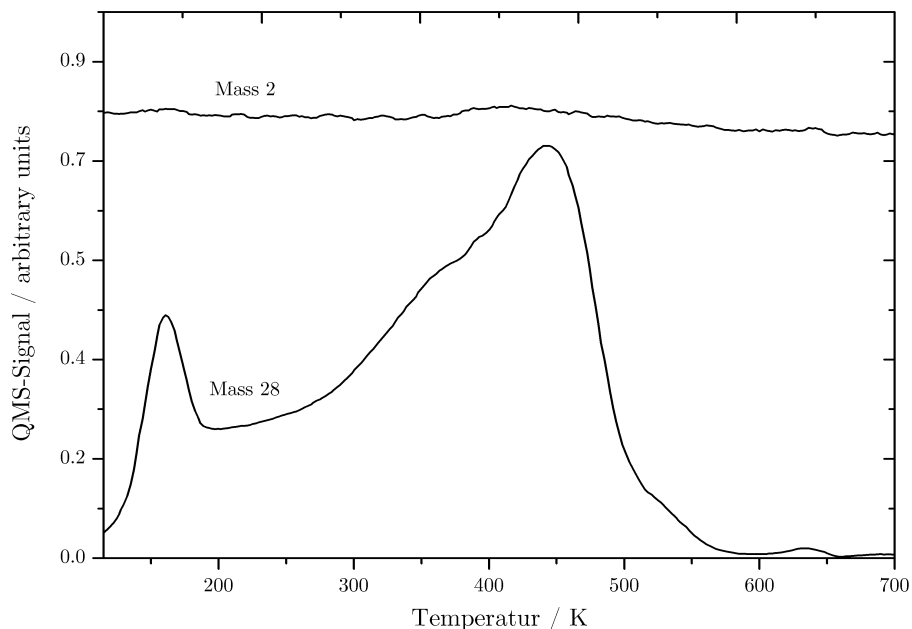


**Figure 7.1.:** TDS of adsorbed H<sub>2</sub> after preadsorption of CO on clean Pd(111): Adsorption of CO with an exposure of 145 L whilst cooling down the sample from 300 K to 115 K; followed by adsorption of H<sub>2</sub> with an exposure of 216 L at  $T_{Pd} = 115$  K

The TPD spectrum in figure 7.1 shows that the CO-precovered surface obviously prevents the adsorption of hydrogen giving rise to a flat mass 2 signal in the TDS. The CO-signal however looks fairly the same as in the TDS for solely adsorbed CO on Pd(111) (see figure 5.1).

Thus the surface sites for dissociative hydrogen adsorption are blocked by the preadsorbed CO. The site blocking may either be caused by the fact that the adsorption site is already occupied by CO, or by the fact that vacant adsorption sites are inaccessible due to the presence of neighbouring CO molecules.

As already described in chapter 5 the CO molecules form a (2×2) superstructure with three CO molecules in the unit cell, which corresponds to a saturation coverage of 0.75 monolayer. This gives rise to a dense structure whereas two molecules occupy hollow sites and one is bond on-top. Thus there are still several vacant Pd sites available allowing hydrogen to adsorb, but the preadsorbed CO modifies the electronic structure of the substrate, that is the barrier for hydrogen adsorption is increased (see [66]).

## 7.2. H<sub>2</sub> Followed by CO

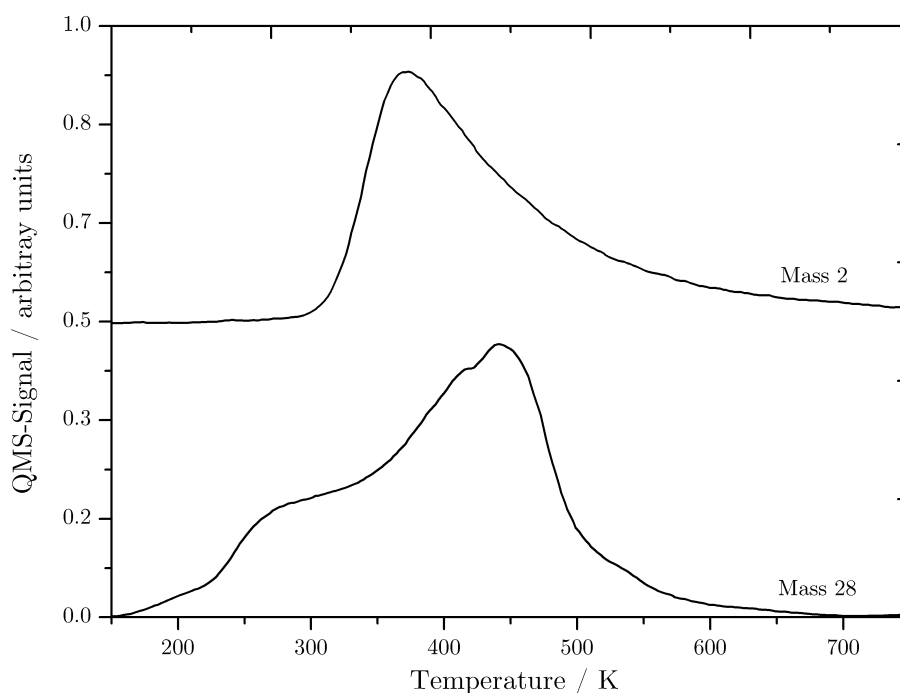


**Figure 7.2.:** TDS of adsorbed CO after preadsorption of H<sub>2</sub> on clean Pd(111): Adsorption of H<sub>2</sub> with an exposure of 216 L followed by adsorption of CO with an exposure of 85 L, Sample temperature  $T_{Pd} = 250$  K

First hydrogen was adsorbed on the Pd surface (H<sub>2</sub> exposure: 216 L) but now at a sample temperature of 250 K to avoid the adsorption of water on the sample surface. Then CO with an exposure of 85 L was adsorbed. The following TDS with a heating rate of 2 K/s is shown in figure 7.2.

Again the CO signal looks fairly the same as the TDS of solely adsorbed CO (figure 5.1). But the mass 2 QMS-signal provides now a clear evidence for adsorbed hydrogen with the peak maximum at 370 K. Compared to the TDS of adsorbed hydrogen without CO (figure 6.1) the peak maximum has shifted about 80 K up. Due to this shift of the hydrogen peak it is clear, that CO and H<sub>2</sub> cannot be present as separate islands on the surface, because in that case hydrogen should still desorb around a temperature of 290 K. Furthermore, the TDS area is about three times larger than the area of the surface peak (figure 6.1) for hydrogen on clean Pd(111).

H<sub>2</sub> desorption spectra with similar peak shapes including a sloping high temperature tail have been observed before by Kiskinova et al [72] which was explained by contribution of hydrogen penetrated into the bulk. In our case this indicates that the CO molecules replace the preadsorbed hydrogen on the surface, pushing the hydrogen atoms below the surface. Due to the fact that hydrogen is soluble at 250 K in palladium this gives rise to the dissolution of hydrogen in the bulk material.

But since hydrogen can only recombine to H<sub>2</sub> followed by desorption on a sufficiently free Pd surface, hydrogen desorption is hindered by the presence of CO on the surface at low temperatures. Only after CO is partially desorbed from the Pd surface, hydrogen that is located in the bulk can migrate to the CO-free surface sites and desorb then recombinatively which causes the shift of the hydrogen peak to higher temperatures (see also [66]).

## 8. Adsorption and Desorption of $O_2$ on Pd(111)

*The measurement results for adsorption of  $O_2$  on Pd(111) and the structure of the chemisorbed oxygen layer are presented. Moreover, the exposure of palladium to oxygen at higher temperatures gives rise to the formation of an palladium-oxide which is described.*

To obtain an adsorbate-free Pd(111) surface the sample was pretreated by holding the sample at 800 K in the presence of  $O_2$ . Then oxygen was adsorbed whereas the sample was held at 375 K. Thus the sample was held at a temperature above the desorption peak maximum of hydrogen, to avoid the adsorption of hydrogen which is always present in the residual gas. The following TDS after an exposure of 40 L  $O_2$  is shown in figure 8.1. It exhibits a single symmetric peak with the maximum located at a temperature of 710 K, an obvious second-order process [73].

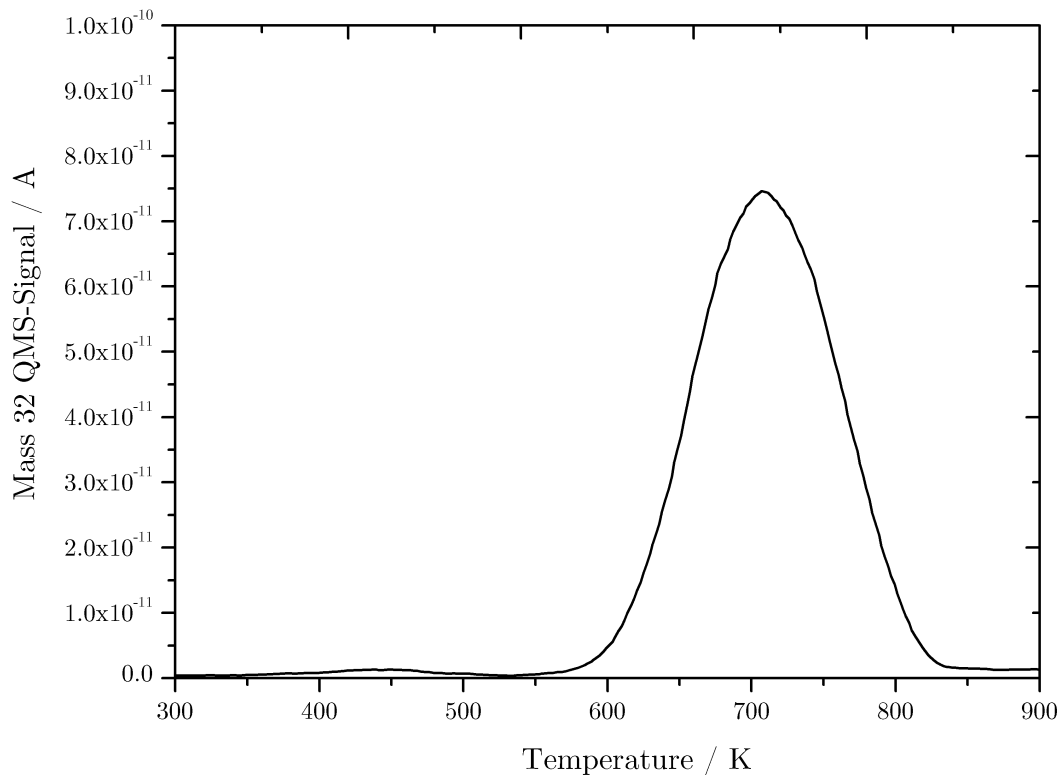


**Figure 8.1.:** TDS of  $O_2$  (exposure: 40 L) adsorbed on clean Pd(111)  
Sample temperature  $T_{Pd} = 375$  K; Heating rate: 2K/s;

In addition to TDS, LEED experiments were carried out. Figure 8.2(a) displays the LEED-pattern after dosing 40 L oxygen at room temperature, taken at a beam energy of 51 eV. It is clearly seen that the chemisorbed oxygen on Pd(111) gives rise to a primitive (2×2) superstructure. The big highlighted hexagon in the LEED pattern corresponds to the (1×1) structure of the Pd substrate whereas the reflexes half way between the outer hexagon sides and the reflexes highlighted by the inner hexagon are caused by the oxygen (2×2) superstructure.

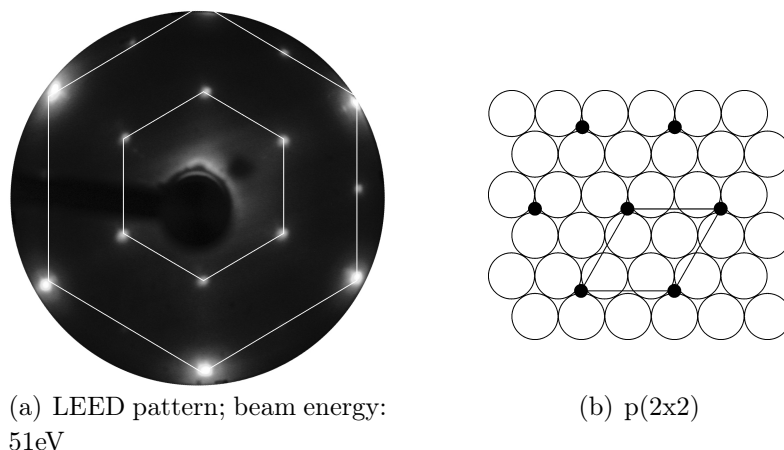


**Figure 8.2.:** p(2×2) superstructure of oxygen adsorbed on Pd(111)

According to this the adsorption of O<sub>2</sub> on Pd(111) at room temperature gives rise to a p(2×2) superstructure with the oxygen chemisorbed in the three-fold hollow sites (see [74], [75]). The structure model is shown in figure 8.2(b). This superstructure implies a surface coverage of 25% and thus a saturation coverage of 0.25 ML for oxygen at room temperature.

## 8.1. Formation of a Palladium-Oxide

Exposure of Pd(111) to O<sub>2</sub> at room temperature gives rise to the chemisorption of atomic oxygen in a simple (2×2) overlayer which was described above, but the oxygen uptake does not proceed beyond this point. Increasing the temperature of the palladium sample during the exposure above 500 K causes diffusion of oxygen atoms into the surface layer and the formation of a surface oxide.

By increasing the coverage of the adsorbed layer beyond 0.25 monolayer, repulsive adsorbate-adsorbate interactions reduce the heat of adsorption below the heat of formation of the oxide. Therefore at higher coverages the oxide formation is favoured. Figure 8.3 provides LEED patterns of the oxide after the Palladium sample, held at a temperature of 700 K, had been exposed to O<sub>2</sub> at a pressure of  $5 \cdot 10^{-8}$  Torr for 10 minutes.

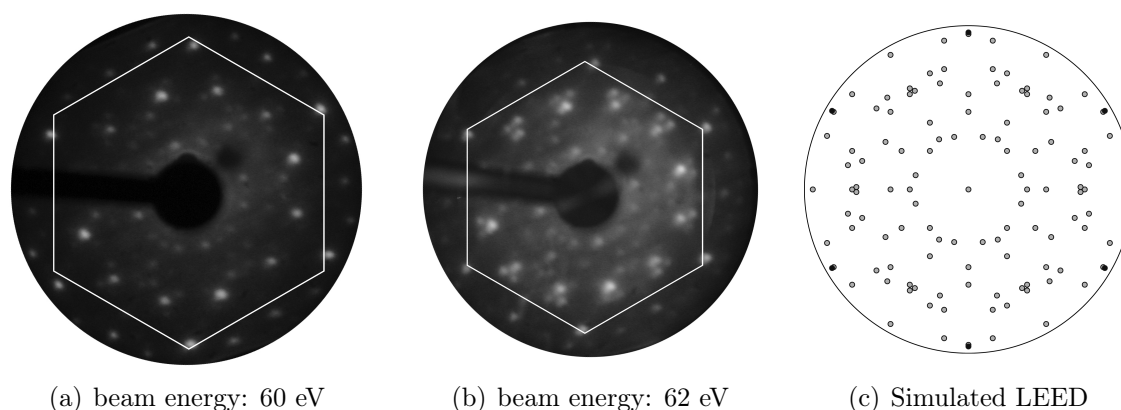


**Figure 8.3.:** LEED patterns of the PdO superstructure on Pd(111)

Surface oxides of Pd(111) have been reported by Voigt et al [76], Gabasch et al [77] and Klikovits et al [78]. Zheng et al [79] were also able to prepare a palladium-oxide and presented several LEED patterns. Compared to them, our LEED patterns show the same distinctive features including an inner ring of 18 spots, a second ring of 12 spots and then groups of three spots (figure 8.3(b)).

With the aid of STM Zheng et al were able to show that this pattern is caused by three equivalent domains of two different structures: a rectangular structure (figure 8.4(b)) and islands and peninsulas with a square structure (figure 8.4(a)). These LEED patterns of figure 8.4 were simulated by using a computer programme called LEEDSIM by Stefan Mannsfeld.

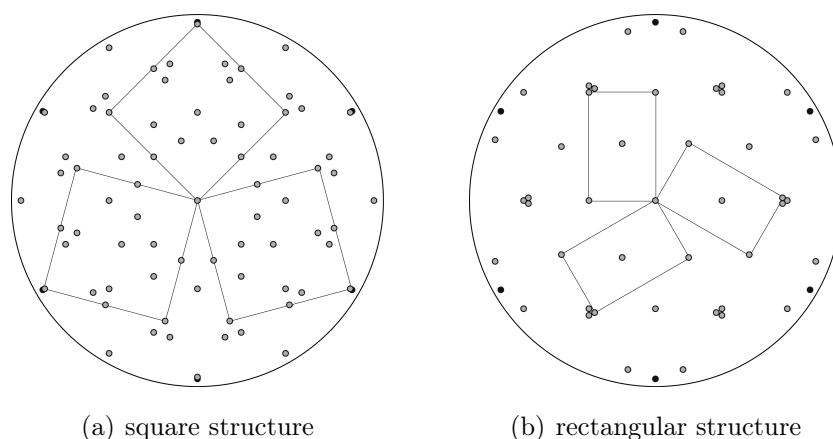


**Figure 8.4.:** LEED schematics of the PdO superstructure for:  
 (a) three equivalent domains of the square structure with highlighted unit cells;  
 (b) three equivalent domains of the rectangular structure with highlighted unit cells. The black solid circles represent spots due to the Pd(111) substrate.

The rectangular PdO structure is characterized by lattice constants equal to 3.9 and 6.4 Å whereas the short sides of the rectangles run parallel to Pd(110). Besides

this rectangular structure there grow islands and peninsulas which exhibit a square structure with a lattice constant of 6.8 Å. The  $\langle 10 \rangle$  direction of the squares is rotated 15° with respect to the Pd $\langle 110 \rangle$  directions [79].

Figure 8.3(c) shows a simulated LEED pattern (again LEEDSIM was used) obtained by superimposing the LEED patterns of the rectangular and the square structure each one including the three equivalent domains.

## 9. Angular Distribution of $D_2$ Desorbing from Pd(111) and Pd/Zn

*This chapter provides the measured angular distributions of deuterium desorbing from the clean and the Zn-modified Pd surface. The measured data are compared with simulated results to give an estimation of the corresponding  $\cos^n\vartheta$ -distribution. Thus the angular distribution from clean Pd(111) is due to a  $\cos\vartheta$  distribution whereas it is much sharper for Pd/Zn.*

The measurement procedure to obtain the angular distribution of desorbing particles by permeation has already been described in section 3.6 and the theory was given in section 2.5.

Since we do not have a real angular dependent detector the angular dependence is measured by shifting the sample in one direction parallel to the detector, while the normal distance between detector plane and emitter plane  $d$  remains the same. The experimental setup during this measurement is provided in figure 9.1.

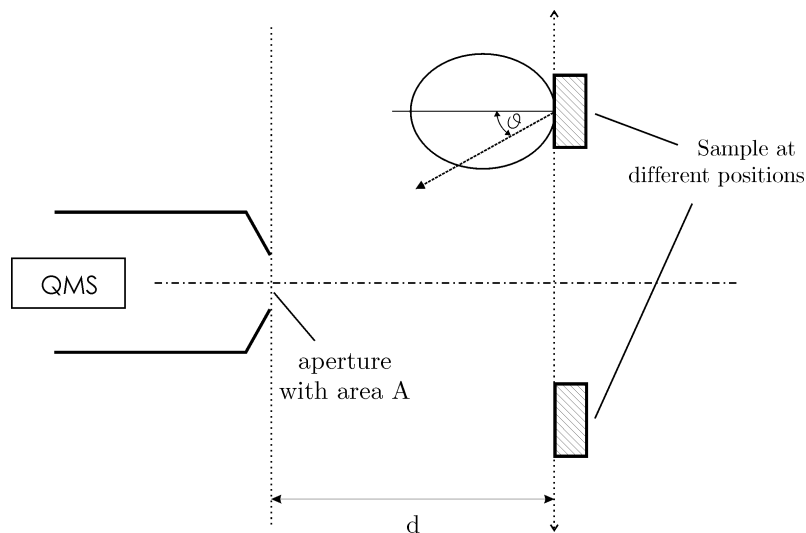


**Figure 9.1.:** Sample arrangement during the angular distribution measurements: The sample is displaced in front of the detector. Geometrical parameters: radius of the sample:  $r_s = 5$  mm, radius of the aperture of the detector  $r_d = 4$  mm, distance between sample and aperture:  $d = 8.5$  mm

Due to this measurement and the experimental geometry it is not possible to compare the measured intensity directly with a  $\cos^n \vartheta$  but rather by simulating the measurement. In the simulation the particles are desorbed according to a  $\cos^n \vartheta$  whereupon the experimental geometry is now taken into account.

## 9.1. The Simulation Program

The simulation program was essentially implemented by DI Johanna Stettner (see [56]) and only slightly modified to include cosine-distributions with a fractional exponent later on. The steps during the simulation are the following:

1.
  - Select a random starting point on the sample and let a particle desorb from this point with a random angle  $\varphi$  and  $\vartheta$  according to the  $\cos^n \vartheta$  distribution.
  - Calculate the arrival point of the desorbing particle at the detector plane.
  - If the arrival point is inside the area of the detector, the particle will be detected and the number of detected particles is increased by 1.
2. Repeat this procedure for a preferable large number of particles  $N$ .
3. Shift the lateral position of the detector and repeat the same procedure for  $N$  particles.

Thus one obtains the number of detected particles for different lateral positions of the sample whereas each particle desorbs according to a  $\cos^n \vartheta$  distribution. By normalizing the simulated data and plotting it versus the lateral displacement it may be compared to the normalized measured intensity. In case of a large number  $N$  of desorbing particles the simulated ratio is a good approximation to the real value of the intensity ratio.

## 9.2. Comparison of Simulated and Measured Results

### 9.2.1. Angular Distribution of D<sub>2</sub> Desorbing from Pd(111)

In figure 9.2 the normalized intensity of D<sub>2</sub> desorbing from Pd(111) with a temperature of 390 K is shown. The simulation yielded the best coinciding results compared to the measured data for a  $\cos^{1.2} \vartheta$ -distribution (solid line in figure 9.2).

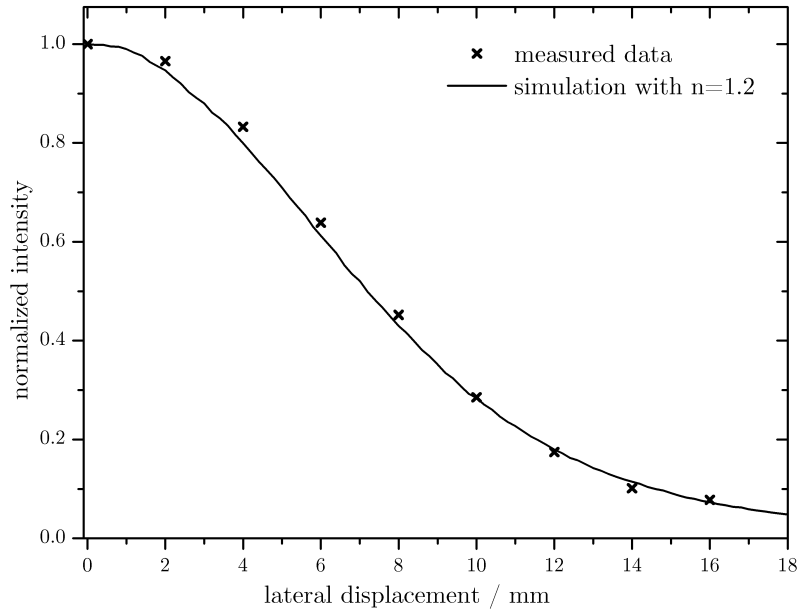


**Figure 9.2.:** Angular distribution of Deuterium desorbing from clean Pd(111) achieved by permeation of D<sub>2</sub> through the sample with  $T_{\text{Pd}}=390$  K, distance between sample and aperture:  $d = 8.5$  mm

Hence it seems that the angular distribution of D<sub>2</sub> desorbing from clean Pd(111) at 390 K is quite close to a cosine-distribution. This is in a good agreement with earlier performed measurements which are described in [42] and [56].

### 9.2.2. Angular Distribution of D<sub>2</sub> Desorbing from Pd/Zn

The same angular distribution measurements were performed with zinc-covered palladium in the submonolayer region. The obtained normalized intensity of D<sub>2</sub> desorbing from Pd/Zn with a temperature of 390 K is provided in figure 9.3.

Compared to the simulated curve for clean palladium (grey solid curve in figure 9.3) the angular distribution for Pd/Zn is much sharper than a cosine-distribution for small angles or a small lateral displacement, respectively. However at rather large angles the distribution becomes broader again.

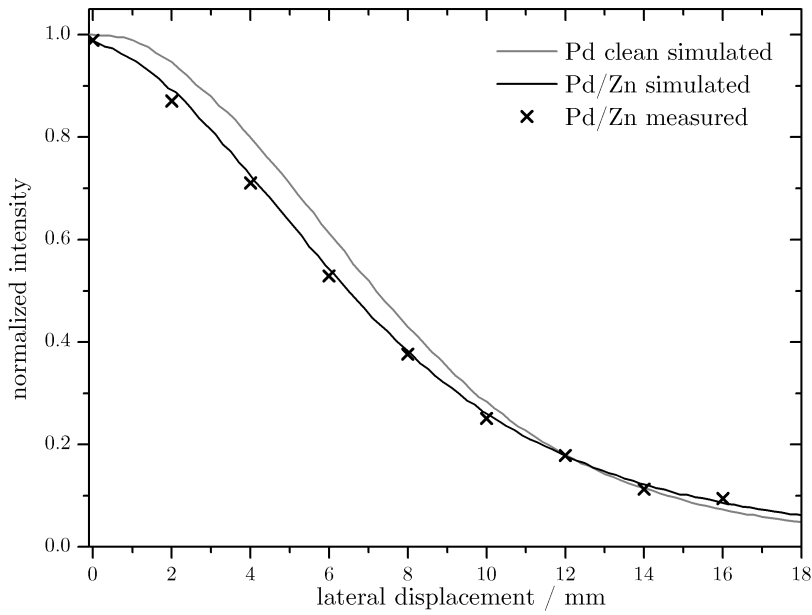


**Figure 9.3.:** Angular distribution of Deuterium desorbing from Pd/Zn achieved by permeation of D<sub>2</sub> through the sample with  $T_{Pd}=390$  K, distance between sample and aperture:  $d = 8.5$  mm

This behaviour has been observed before and was described by a distribution composed of two components, a cosine law component and a component peaked around the surface normal (see [18]). Therefore trying several combinations of  $\cos^n \vartheta$  the best coincidence with the measured data was achieved by a simulated angular distribution according to:

$$I_{D_2}(\vartheta) = a \cdot \cos \vartheta + (1 - a) \cdot \cos^6 \vartheta \quad (9.1)$$

with  $a = 0.9$ . The simulated curve is also shown in figure 9.3 (black solid curve). Thus the recorded angular distribution can be described with about 90% of the molecules coming off the surface with a cosine distribution and 10% according to a  $\cos^6$  distribution. Segner et al [80] assigned the effect that molecules according to two different angular distributions are desorbing to surface defects. Therefore one can imagine that this is also caused by the morphology of the zinc layer.

Hence we can conclude by saying that the angular distribution of D<sub>2</sub> desorbing from clean Pd(111) is due to a  $\cos^{1.2} \vartheta$  distribution whereupon the distribution of zinc covered palladium is much sharper and may be described according to equation 9.1.

## 10. Summary

The present work handles the interaction of hydrogen/deuterium, carbon monoxide and oxygen with clean and zinc covered palladium (111) surfaces. The main results are summarized below.

### Zn and ZnO on Pd(111)

#### Zn on Pd(111)

The morphology of the prepared zinc layer depends strongly on the surface temperature at which it is evaporated on the substrate. LEED patterns and STM images show that at low temperatures (150 K) zinc forms an epitaxial overlayer which starts to grow in islands at low coverages. With increasing temperature (above 300 K) the zinc layer forms a Pd/Zn surface alloy with a  $(2\times 1)$  superstructure according to alternating rows of zinc and palladium atoms.

The thermal desorption of zinc layers with high coverages leads to a low temperature peak (400-600 K) arising from upper zinc layers and a second peak (above 800 K) originating from the lower zinc layers which are more strongly bound. The latter peak exhibits its maximum at 1040 K. Thus the heat of adsorption for the zinc monolayer on Pd(111) was determined to be  $281\pm 5$  kJ mol<sup>-1</sup>.

The low temperature peak features several peaks at slightly different temperatures which are difficult to separate due to their overlap. Therefore the TD spectra were fitted according to simulated desorption rates to allow a better analysis. This was done for desorption series with different zinc coverages and for zinc layers which were prepared at 150 K and at 300 K. Hence the corresponding desorption energies of the single low temperature peaks were determined to be  $118\pm 5$  kJ mol<sup>-1</sup>,  $120\pm 5$  kJ mol<sup>-1</sup>,  $128\pm 5$  kJ mol<sup>-1</sup> and  $139\pm 5$  kJ mol<sup>-1</sup>. In addition the desorption energy of a zinc multilayer ( $\approx 20$  ML) was evaluated to be  $116\pm 5$  kJ mol<sup>-1</sup> which matches the literature value for the heat of vaporization of zinc.

Interestingly the single low temperature peaks indicate a typical zero order desorption followed by a transition to first order desorption. This may be explained by desorption of atoms from a dilute phase whereupon the dilute phase maintains equilibrium with a dense phase, thus it is held constant at the expense of the dense phase.

## ZnO on Pd(111)

The ZnO layer was prepared by oxidation of the Zn layer. The prepared ZnO forms an overlayer of the hexagonal ZnO Wurtzite (0001) plane on Pd(111) which causes a (6×6) superstructure. This is supported by STM images and the (6×6) pattern which is visible in the LEED.

The prepared ZnO layer may be reduced by CO via the formation of CO<sub>2</sub> as well as by H<sub>2</sub> via the formation of H<sub>2</sub>O. This is done by sequential dosing and desorbing CO and H<sub>2</sub> in several cycles respectively. The gradual change of the surface is seen in the LEED pattern and the Auger-signal. In addition, due to the higher temperature at which CO desorbs, the zinc atoms start to migrate into the subsurface region causing a Pd/Zn alloy after several CO desorption cycles.

## CO on Pd and Pd/Zn

- **CO on Pd(111):**

CO adsorbed on Pd(111) at 170 K gives rise to a (2×2)-3CO superstructure which corresponds to a saturation coverage of 0.75 monolayer. The peak maximum appears at a temperature of 440 K in the TDS.

- **CO on Pd/Zn:**

A thick zinc layer ( $\approx 10$  ML) blocks the adsorption of CO. On the Pd/Zn surface alloy the heat of adsorption for CO is shifted to much lower values than compared to Pd(111). Therefore no CO adsorption occurs at room temperature but adsorption at lower temperatures gives rise to a new desorption peak at 220 K. At low CO coverages this corresponds to a desorption energy of  $62 \pm 2$  kJ mol<sup>-1</sup>. The reduction in the adsorption energy of CO is caused by the Pd-Zn interactions in the surface alloy which alters the electronic structure of the Pd atoms and thus weakens the strength of the Pd-CO bonds.

Due to the repulsive interaction between the CO admolecules the coverage does not grow linearly with increasing exposure and the desorption energy decreases with increasing coverage. The saturation coverage of adsorbed CO is at 0.37 monolayer which means that each Pd row is occupied with CO molecules by about 2/3.

Furthermore, the CO adsorption on Pd/Zn with the zinc layers prepared at different temperatures and with varying coverages was investigated. Depending on the morphology of the zinc layer three possible adsorption sites are available: The CO molecule may adsorb on the "normal" Pd sites of an uncovered substrate region, on the Pd sites at the edge of a zinc island and on the Pd sites of the Pd/Zn surface alloy. When the zinc layer is prepared at 150 K the amount of adsorbed CO becomes very small at coverage of approximately 1 ML but not exactly zero due to a mixing with the offline signal. On the surface alloy which forms at 350 K the amount of adsorbed CO decreases

slower with increasing coverage. Above a Zn coverage of one monolayer the adsorption on the Pd sites of the surface alloy is still possible.

Annealing of the prepared zinc layer at 650 K and 700 K gives rise to further changes in the CO TD spectrum. This change in the TDS comes along with a decrease of the Zn/Pd ratio in the Auger signal which is an evidence that either zinc atoms start to migrate into the subsurface region or Pd atoms segregate on top of the zinc.

## Hydrogen on Pd and Pd/Zn

- **Hydrogen on Pd:**

At low exposures  $H_2$  is adsorbed dissociatively on the surface without any penetration into the bulk material. With increasing exposure a second peak occurs in the TDS at a temperature below the desorption of the chemisorbed hydrogen. This peak indicates the diffusion of hydrogen into the subsurface region.

- **Hydrogen on PdZn:**

On the Pd/Zn surface alloy the adsorption of hydrogen on surface sites is reduced by about 1/2 whereupon it still desorbs at the same temperature. Thus the zinc atoms on the surface do not give rise to any energetic changes but to a change in the number of adsorption sites. However, the diffusion of hydrogen into the subsurface region is not influenced.

## Sequentially dosed $H_2$ and CO on Pd(111)

- **CO followed by  $H_2$ :**

If the Pd(111) crystal is precovered by adsorbed CO, the surface sites for dissociative hydrogen adsorption will be blocked by the preadsorbed CO molecules. Therefore the adsorption of hydrogen is hindered whereupon the CO signal remains the same in the TDS.

- **$H_2$  followed by CO:**

In this case the CO molecules replace the preadsorbed hydrogen on the surface, pushing the hydrogen atoms below the surface. Despite the unchanged CO signal there is also a  $H_2$  signal in the TDS but with the peak maximum shifted to higher temperatures. This is due to the fact that hydrogen can only recombine to  $H_2$  followed by desorption on a sufficiently free Pd surface. Hence only at higher temperatures, after CO has partially desorbed from the Pd surface, hydrogen that is located in the bulk can migrate to the CO-free surface sites and desorb then recombinatively.

## O<sub>2</sub> on Pd(111)

The adsorption of O<sub>2</sub> on Pd(111) at room temperature gives rise to a p(2×2) superstructure with the oxygen chemisorbed in the three-fold hollow sites. This corresponds to a saturation coverage of 0.25 ML beyond which the oxygen uptake does not proceed at room temperature.

Increasing the temperature of the palladium sample during the O<sub>2</sub> exposure above 500 K causes diffusion of oxygen atoms into the surface layer and the formation of a surface oxide. In the LEED a rather complex pattern is observed which may be described by three equivalent domains of a rectangular structure together with islands and peninsulas with a square structure.

## Angular Distribution of D<sub>2</sub> desorbing from Pd and Pd/Zn

For this measurements the Pd(111) crystal as part of a permeation source was used. Thus the deuterium exposure was performed by permeation through the bulk. In general, angular distributions of desorbing particles are assumed to have the form  $\cos^n \vartheta$ . Since the angular distribution was not measured by an angular dependent detector but simply by a lateral shift of the sample, simulations were performed to determine the value of n. The main results concerning the angular distributions for deuterium are the following:

- **Clean Pd(111):**

At a surface temperature of 390 K the distribution is close to a cosine function. The results are in a good agreement with previous results about the desorption of deuterium.

- **Pd/Zn:**

The angular distribution is much sharper than a cosine-distribution for small angles but at large angles the distribution becomes broader again. The recorded angular distribution may be described by a fraction of the molecules coming off the surface with a cosine distribution and a fraction according to a  $\cos^6 \vartheta$  distribution.

# 11. Bibliography

- [1] S. Ahmed and M. Krumpelt. Hydrogen from hydrocarbon fuels for fuel cells. *International Journal of Hydrogen Energy*, 26(4):291–301, April 2001.
- [2] N. Takezawa and N. Iwasa. Steam reforming and dehydrogenation of methanol: Difference in the catalytic functions of copper and group VIII metals. *Catalysis Today*, 36(1):45–56, April 1997.
- [3] Nobuhiro Iwasa, Tomoyuki Mayanagi, Wataru Nomura, Masahiko Arai, and Nobutsune Takezawa. Effect of Zn addition to supported Pd catalysts in the steam reforming of methanol. *Applied Catalysis A: General*, 248(1–2):153–160, October 2002.
- [4] Shetian Liu, Katsumi Takahashi, and Muneo Ayabe. Hydrogen production by oxidative methanol reforming on PdZnO catalyst: Effects of Pd loading. *Catalysis Today*, 87(1–4):247–253, November 2003.
- [5] Shetian Liu, Katsumi Takahashi, Haruki Eguchi, and Kazuo Uematsu. Hydrogen production by oxidative methanol reforming on Pd/ZnO: Catalyst preparation and supporting materials. *Catalysis Today*, 129(3–4):287–292, November 2007.
- [6] J. A. Barker and D. J. Auerbach. Gas-surface interactions and dynamics; Thermal energy atomic and molecular beam studies. *Surface Science Reports*, 4(1–2):1–99, 1984.
- [7] Harald Ibach. *Physics of Surfaces and Interfaces*. Springer Verlag, 2006.
- [8] Klaus Christmann. *Introduction to Surface Physical Chemistry*. Springer Verlag, 1991.
- [9] Andrew Zangwill. *Physics at Surfaces*. Cambridge University Press, 1988.
- [10] Stephen J. Lombardo and Alexis T. Bell. A review of theoretical models of adsorption, diffusion, desorption, and reaction of gases on metal surfaces. *Surface Science Reports*, 13(1–2):3–72, July 1991.
- [11] Richard I. Masel. *Theoretical surface science*. Springer, 2003.

- 
- [12] Axel Groß. *Principles of Adsorption and Reaction on Solid Surfaces*. Wiley & Sons, 1998.
- [13] Bjørk Hammer, Matthias Scheffler, Karsten W. Jacobsen, and Jens K. Nørskov. Multidimensional Potential Energy Surface for H<sub>2</sub> Dissociation over Cu(111). *Phys. Rev. Lett.*, 73(10):1400–1403, Sep 1994.
- [14] George C. Schatz. The analytical representation of electronic potential-energy surfaces. *Rev. Mod. Phys.*, 61(3):669–, July 1989.
- [15] J. C. Polanyi and W. H. Wong. Location of Energy Barriers. I. Effect on the Dynamics of Reactions A + BC. *The Journal of Chemical Physics*, 51(4):1439–1450, 1969.
- [16] K. Oura, V.G. Lifshits, A.A. Saranin, A.V. Zotov, and M. Katayama. *Surface Science. An Introduction*. Springer Verlag, 2003.
- [17] David A. King and Michael G. Wells. Molecular beam investigation of adsorption kinetics on bulk metal targets: Nitrogen on tungsten. *Surface Science*, 29(2):454–482, February 1972.
- [18] George Comsa and Rudolf David. Dynamical parameters of desorbing molecules. *Surface Science Reports*, 5(4):145–198, December 1985.
- [19] R. R. Cavanagh and D. S. King. Internal energy distributions in thermally desorbed molecules. *Journal of Vacuum Science & Technology A: Vacuum, Surfaces, and Films*, 1(2):1267–1268, 1983.
- [20] Ivan Kuščer. Reciprocity in scattering of gas molecules by surfaces. *Surface Science*, 25(2):225–237, April 1971.
- [21] E. P. Wenaas. Equilibrium Cosine Law and Scattering Symmetry at the Gas-Surface Interface. *The Journal of Chemical Physics*, 54(1):376–388, 1971.
- [22] W. Van Willigen. Angular distribution of hydrogen molecules desorbed from metal surfaces. *Physics Letters A*, 28(2):80–81, November 1968.
- [23] K. D. Rendulic and A. Winkler. Adsorption and desorption dynamics as seen through molecular beam techniques. *Surface Science*, 299-300:261–276, January 1994.
- [24] M. J. Cardillo, M. Balooch, and R. E. Stickney. Detailed balancing and quasi-equilibrium in the adsorption of hydrogen on copper. *Surface Science*, 50(2):263–278, June 1975.

- [25] George Comsa, Rudolf David, and Bernd-Josef Schumacher. The angular dependence of flux, mean energy and speed ratio for  $D_2$  molecules desorbing from a Ni(111) surface. *Surface Science*, 85(1):45–68, June 1979.
- [26] M. Balooch and R. E. Stickney. Angular distributions of  $H_2$  desorbed from the (100), (110), and (111) faces of copper crystals. *Surface Science*, 44(2):310–320, August 1974.
- [27] C. M. Chan, R. Aris, and W. H. Weinberg. An analysis of thermal desorption mass spectra. I. *Applications of Surface Science*, 1(3):360–376, May 1978.
- [28] C. M. Chan and W. H. Weinberg. An analysis of thermal desorption mass spectra. II. *Applications of Surface Science*, 1(3):377–387, May 1978.
- [29] R. L. Palmer, Jr. Joe N. Smith, Howard Saltsburg, and D. R. O’Keefe. Measurements of the Reflection, Adsorption, and Desorption of Gases from Smooth Metal Surfaces. *The Journal of Chemical Physics*, 53(5):1666–1676, 1970.
- [30] J.M. Soler and N. García. How much quantitative information may be expected from programmed desorption experiments? *Surface Science*, 124(2-3):563–570, January 1983.
- [31] E. Habenschaden and J. Küppers. Evaluation of flash desorption spectra. *Surface Science*, 138(1):L147–L150, March 1984.
- [32] Deborah Holmes Parker, Mark E. Jones, and Bruce E. Koel. Determination of the reaction order and activation energy for desorption kinetics using TPD spectra: Application to  $D_2$  desorption from Ag(111). *Surface Science*, 233(1-2):65–73, July 1990.
- [33] P. A. Redhead. Thermal desorption of gases. *Vacuum*, 12(4):203–211, 1962.
- [34] Arnold Hellmann, Egon Wiberg, and Nils Wiberg. *Lehrbuch der anorganischen Chemie*. de Gruyter, 101 edition, 1995.
- [35] Jean d’Ans, Ellen Lax, and Roger Balchon. *Taschenbuch für Chemiker und Physiker: Elemente, anorganische Verbindungen und Materialien, Minerale*, volume 3. Springer, 1998.
- [36] Anton Kokalj. Computer graphics and graphical user interfaces as tools in simulations of matter at the atomic scale. *Computational Materials Science*, 28(2):155–168, October 2003. Code available from <http://www.xcrysden.org/>.
- [37] Zhao-Xu Chen, Konstantin M. Neyman, and Notker Rösch. Theoretical study of segregation of Zn and Pd in Pd-Zn alloys. *Surface Science*, 548(1-3):291–300, January 2004.

- [38] Andreas Bayer, Ken Flechtner, Reinhard Denecke, Hans-Peter Steinrück, Konstantin M. Neyman, and Notker Rösch. Electronic properties of thin Zn layers on Pd(111) during growth and alloying. *Surface Science*, 600(1):78–94, January 2006.
- [39] José A. Rodriguez, Robert A. Campbell, and D. Wayne Goodman. Electron donor-electron acceptor interactions in bimetallic surfaces: theory and XPS studies. *J. Phys. Chem.*, 95(15):5716–5719, July 1991.
- [40] José A. Rodriguez. Interactions in Bimetallic Bonding: Electronic and Chemical Properties of PdZn Surfaces. *J. Phys. Chem.*, 98(22):5758–5764, June 1994.
- [41] Zhao-Xu Chen, Konstantin M. Neyman, Aleksey B. Gordienko, and Notker Rösch. Surface structure and stability of PdZn and PtZn alloys: Density-functional slab model studies. *Phys. Rev. B*, 68(7):075417–, August 2003.
- [42] T. Engel and H. Kuipers. A molecular-beam investigation of the scattering, adsorption and absorption of H<sub>2</sub> and D<sub>2</sub> from/on/in Pd(111). *Surface Science*, 90(1):162–180, December 1979.
- [43] H. Conrad, G. Ertl, and E. E. Latta. Adsorption of hydrogen on Palladium single crystal surfaces. *Surface Science*, 41(2):435–446, February 1974.
- [44] G. Alefeld and J. Völkl. *Hydrogen in metals*, volume 2. Springer, 1978.
- [45] Klaus Christmann. Interaction of hydrogen with solid surfaces. *Surface Science Reports*, 9(1–3):1–163, July 1988.
- [46] Axel Gross, Steffen Wilke, and Matthias Scheffler. Six-Dimensional Quantum Dynamics of Adsorption and Desorption of H<sub>2</sub> at Pd(100): Steering and Steric Effects. *Phys. Rev. Lett.*, 75(14):2718–, October 1995.
- [47] G. R. Darling and S. Holloway. The role of parallel momentum in the dissociative adsorption of H<sub>2</sub> at highly corrugated surfaces. *Surface Science*, 304(3):L461–L467, March 1994.
- [48] Michael Beutl, Manfred Riedler, and Klaus D. Rendulic. Strong rotational effects in the adsorption dynamics of H<sub>2</sub>/Pd(111): evidence for dynamical steering. *Chemical Physics Letters*, 247(3):249–252, December 1995.
- [49] J. Rogozik and V. Dose. The role of the 2 $\pi$  level in CO chemisorption on metal surfaces. *Surface Science*, 176(1-2):L847–L851, October 1986.
- [50] Evgeny Shustorovich. Bonding vs. antibonding states in transition metal bond activation: energetic grounds and stereochemical implications. *Journal of Physical Chemistry*, 87(1):14–17, 1983.

- [51] Evgeny Shustorovich and Roger C. Baetzold. Toward A Coherent Theory of Chemisorption. *Science*, 227(4689):876–881, February 1985.
- [52] Christian Eibl. *Kinetik und Dynamik der Adsorption und Desorption von Wasserstoff (Deuterium) auf Vanadiumoberflächen*. PhD thesis, Institut für Festkörperphysik der Technischen Universität Graz, 2001.
- [53] Gernot Pauer. *Desorption and Reaction Dynamics of Hydrogen on Clean and Modified Rhodium and Palladium Crystal Surfaces*. PhD thesis, Institute of Solid State Physics, Graz, University of Technology, 2005.
- [54] Markus Kratzer. Flugzeituntersuchungen von Desorptions- und Reaktionsprodukten an modifizierten Pd-Oberflächen. Master's thesis, Institut für Festkörperphysik der Technischen Universität Graz, 2004.
- [55] Paul W. Palmberg, Gerald E. Riach, Roland E. Weber, and Noel C. MacDonald. *Handbook of Auger Electron Spectroscopy. A reference Book of Standard Data for Identification and Interpretation of Auger Electron Spectroscopy Data*. Physical Electronics Industries Inc., 1972.
- [56] Johanna Stettner. Angular distributions of deuterium desorption from modified Pd(111) surfaces. Master's thesis, Institute of Solid State Physics, Graz, University of Technology, 2007.
- [57] Harald Gabasch, Axel Knop-Gericke, Robert Schlögl, Simon Penner, Bernd Jennewein, Konrad Hayek, and Bernhard Klötzer. Zn Adsorption on Pd(111): ZnO and PdZn Alloy formation. *Journal of Physical Chemistry B*, 110(23):11392–11398, July 2006.
- [58] R. Opila and R. Gomer. Thermal desorption of Xe from the W(110) plane. *Surface Science*, 112(1-2):1–22, December 1981.
- [59] A. Zaoui. Energetic stabilities and the bonding mechanism of ZnO0001/Pd(111) interfaces. *Phys. Rev. B*, 69(11):115403–, March 2004.
- [60] M. K. Rose, T. Mitsui, J. Dunphy, A. Borg, D. F. Ogletree, M. Salmeron, and P. Sautet. Ordered structures of CO on Pd(111) studied by STM. *Surface Science*, 512(1-2):48–60, June 2002.
- [61] W. Kevin Kuhn, Janos Szanyi, and D. Wayne Goodman. CO adsorption on Pd(111): the effects of temperature and pressure. *Surface Science*, 274(3):L611–L618, August 1992.
- [62] X. C. Guo and J. T. Yates. Dependence of effective desorption kinetic-parameters on surface coverage and adsorption temperature - CO on Pd(111). *Journal of Chemical Physics*, 90(11):6761–6766, June 1989.

- [63] T. Gießel, O. Schaff, C. J. Hirschmugl, V. Fernandez, K. M. Schindler, A. Theobald, S. Bao, R. Lindsay, W. Berndt, A. M. Bradshaw, C. Baddeley, A. F. Lee, R. M. Lambert, and D. P. Woodruff. A photoelectron diffraction study of ordered structures in the chemisorption system Pd(111)-CO. *Surface Science*, 406(1-3):90–102, May 1998.
- [64] H. Ohtani, M.A. Van Hove, and G.A. Somorjai. LEED intensity analysis of the surface structures of Pd(111) and of CO adsorbed on Pd(111) in a ( $\sqrt{3} \times \sqrt{3}$ )R30° arrangement. *Surface Science*, 187(2-3):372–386, September 1987.
- [65] Bernhard Klötzer, Werner Unterberger, and Konrad Hayek. Adsorption and hydrogenation of CO on Pd(111) and Rh(111) modified by subsurface vanadium. *Surface Science*, 532-535:142–147, June 2003.
- [66] Matthias Morkel, Günther Rupprechter, and Hans-Joachim Freund. Ultrahigh vacuum and high-pressure coadsorption of CO and H<sub>2</sub> on Pd(111): A combined SFG, TDS and LEED study. *Journal of Chemical Physics*, 119(20):10853–10866, November 2003.
- [67] E. Jerero, V. Lebarbier, A. Datye, Y. Wang, and J.M. Vohs. Interaction of CO with surface PdZn alloys. *Surface Science*, 601(23):5546–5554, December 2007.
- [68] C. Harendt, J. Goschnick, and W. Hirschwald. The interaction of CO with copper (110) studied by TDS and LEED. *Surface Science*, 152-153(Part 1):453–462, April 1985.
- [69] Stefan Vollmer, Gregor Witte, and Christof Wöll. Determination of site specific adsorption energies of CO on copper. *Catalysis Letters*, 77(1-3):97–101, May 2001.
- [70] José A. Rodriguez. Physical and chemical properties of bimetallic surfaces. *Surface Science Reports*, 24(7-8):223–287, 1996.
- [71] G. E. Gdowski, T. E. Felter, and R. H. Stulen. Effect of surface temperature on the sorption of hydrogen by Pd(111). *Surface Science*, 181(3):L147–L155, March 1987.
- [72] M. P. Kiskinova and G. M. Bliznakov. Adsorption and coadsorption of carbon monoxide and hydrogen on Pd(111). *Surface Science*, 123(1):61–76, December 1982.
- [73] Xingcai Guo, Alon Hoffman, and John T. Yates, Jr. Adsorption kinetics and isotopic equilibration of oxygen adsorbed on the Pd(111) surface. *J. Chem. Phys.*, 90(10):5787–5792, May 1989.

- [74] H. Conrad, G. Ertl, J. Küppers, and E. E. Latta. Interaction of NO and O<sub>2</sub> with Pd(111) surfaces II. *Surface Science*, 65(1):245–260, June 1977.
- [75] F. P. Leisenberger, G. Koller, M. Sock, S. Surnev, M. G. Ramsey, F. P. Netzer, B. Klötzer, and K. Hayek. Surface and subsurface oxygen on Pd(111). *Surface Science*, 445(2–3):380–393, January 2000.
- [76] E H Voigt, A J M Mens, O L J Gijzeman, and J W Geus. Adsorption of oxygen and surface oxide formation on Pd(111) and Pd foil studied with ellipsometry, LEED, AES and XPS. *Surface Science*, 373(2–3):210–220, March 1997.
- [77] Harald Gabasch, Werner Unterberger, Konrad Hayek, Bernhard Klotzer, Georg Kresse, Christof Klein, Michael Schmid, and Peter Varga. Growth and decay of the Pd(111)-Pd<sub>5</sub>O<sub>4</sub> surface oxide: Pressure-dependent kinetics and structural aspects. *Surface Science*, 600(1):205–218, January 2006.
- [78] J. Klikovits, E. Napetschnig, M. Schmid, N. Seriani, O. Dubay, G. Kresse, and P. Varga. Surface oxides on Pd(111): STM and density functional calculations. *Physical Review B (Condensed Matter and Materials Physics)*, 76(4):045405, 2007.
- [79] G. Zheng and E. I. Altman. The oxidation of Pd(111). *Surface Science*, 462(1–3):151–168, August 2000.
- [80] J. Segner, C. T. Campbell, G. Doyen, and G. Ertl. Catalytic oxidation of CO on Pt(111): The influence of surface defects and composition on the reaction dynamics. *Surface Science*, 138(2–3):505–523, March 1984.

# A. Appendix - Matlab Programme and Calculated Values

## A.1. Calculation of the Desorption Energy and the Coverage Using the Matlab Programme

The values of the desorption energy and the coverage which were calculated from the zinc TDS (figure 4.5 and 4.8) by using the below mentioned programme are shown in the following tables. The number of the actual curve of the thermal desorption series which was used in the programme is given in the the fist column of each table.

Calculated desorption energy and coverage of the Zn desorption spectra in figure 4.5 (Zn layer prepared at 150 K) by using the Matlab programme:

curve number in figure 4.5	$E_{\text{des,multi}} /$ $\text{kJ mol}^{-1}$	$E_{\text{des,1}} /$ $\text{kJ mol}^{-1}$	$E_{\text{des,2}} /$ $\text{kJ mol}^{-1}$	$E_{\text{des,3}} /$ $\text{kJ mol}^{-1}$	$E_{\text{des,4}} /$ $\text{kJ mol}^{-1}$
6				126.8	139.4
7			114.2	129.7	143.6
8		116.2	121.4	124.9	137.6
9		117.4	121.3	127.8	135.8
10	115.9	118.9	120.0	129.6	137.6
mean	116	117	119	128	139
std dev	-	1	3	2	3

curve number in figure 4.5	$\theta_{\text{total}} / \text{ML}$	$\theta_{\text{multi}} / \text{ML}$	$\theta_1 / \text{ML}$	$\theta_2 / \text{ML}$	$\theta_3 / \text{ML}$	$\theta_4 / \text{ML}$
6	0.76				0.51	0.25
7	2.67			0.84	1.24	0.59
8	4.07		0.20	1.37	1.89	0.62
9	5.18		0.55	1.85	2.05	0.73
10	7.45	0.46	0.94	2.40	2.68	0.97
mean of the relative amount / %			9	34	47	20
standard deviation / %			3	1	11	8

Calculated desorption energy and coverage of the desorption spectra in figure 4.8 (Zn layer prepared at 300 K) by using the Matlab programme:

curve number in figure 4.8	$E_{\text{des,multi}} /$ $\text{kJ mol}^{-1}$	$E_{\text{des,1}} /$ $\text{kJ mol}^{-1}$	$E_{\text{des,2}} /$ $\text{kJ mol}^{-1}$	$E_{\text{des,3}} /$ $\text{kJ mol}^{-1}$	$E_{\text{des,4}} /$ $\text{kJ mol}^{-1}$
7					137.4
8				126.6	135.0
9			122.6	127.8	135.6
10			123.8	127.0	135.6
11		123.5	124.2	129.6	137.6
12		121.7	124.7	129.2	138.1
13	118.7	121.9	124.9	128.9	137.4
mean	119	122	124	128	137
std dev	-	1	1	1	1

curve number in figure 4.8	$\theta_{\text{total}} / \text{ML}$	$\theta_{\text{multi}} / \text{ML}$	$\theta_1 / \text{ML}$	$\theta_2 / \text{ML}$	$\theta_3 / \text{ML}$	$\theta_4 / \text{ML}$
7	0.67					0.67
8	1.54				0.50	1.04
9	2.97			0.29	1.49	1.20
10	4.22			0.75	2.02	1.44
11	5.57		0.47	1.21	2.40	1.49
12	7.62	0.39	1.00	1.60	2.85	1.78
13	10.00	1.08	1.42	1.72	3.45	2.33
mean of the relative amount / %			12	20	38	24
standard deviation / %			3	2	4	2

## A.2. The Matlab Programme

The matlab programme computes the desorption rate according to the Polanyi Wigner equation 2.19 for a given set of parameters. The rate is calculated iteratively at each temperature step. This can be done for multiple peaks whereupon the single peaks are then added to give a cumulative signal. The programme tries to minimize the sum of the squared deviations between the measured and the approximated values. This is done by changing the parameters of the Polanyi Wigner equation randomly and accepting the new ones according to a simulated annealing strategy.

However, the programme and especially the numerical approximation of the Polanyi Wigner equation are very sensitive to the parameters. Thus if the the starting values are chosen badly the programme will fail to converge.

First one has to load the measured data into the programme. The best way to do this is to save them in a file called **data.txt** with the temperature being the first column and the desorption rate (or QMS-signal) being the second column.

Next, you should set the variable **monolayer** to the empirical monolayer in terms of particles·cm<sup>-2</sup> and the variable **Peaks** to the number of desorption peaks that shall be simulated. The monolayer may also be taken arbitrary, however the coverage output will not be correct in this case.

Then the starting values which will be used to compute the desorption rate have to be chosen. Since we want to calculate several peaks, these parameters are stored in vectors whereupon each element of the vector corresponds to the parameter of one single peak starting with the peak at the lowest temperature. The parameters are:

- **ordnbest** - vector with the orders of desorption
- **initialcovbest** - vector with the initial coverages  $\theta_0$  in terms of monolayer
- **nubest** - vector with the preexponential or frequency factors
- **Ebest** - vector with the desorption energies in eV

Despite that, the experimental heating rate  $\beta$  (**beta**) and the parameter  $\omega$  (**omega**) should be given. The parameter  $\omega$  allows a simple approximation for a coverage dependent desorption energy  $E_{\text{des}}(\theta)$  by calculating  $E_{\text{des}}(\theta) = (1 - \omega \cdot \theta)E_{\text{des},0}$  at each temperature step. For example this comes into play if there are repulsive forces between the adsorbates. However, you may set the parameter to 0, which gives rise to a coverage-independent desorption energy.

It shall be noted once more that one has to be very careful when choosing this starting values since the program may not converge or may even give non-physical desorption rates in the case of a bad guess.

The programme will then compute the desorption rate according to the Polanyi

Wigner equation with the given parameters. It calls the function **peaksum.m** which calculates the cumulative desorption rate by adding the individual desorption rates of the single peaks. Therefore another function **dthetadT.m** is called which computes the desorption rate of a single peak iteratively by the following: For each temperature step  $T_i$  the change of the coverage  $\Delta\theta$  is determined according to the Polanyi Wigner equation which gives rise to an approximative value for the new coverage  $\theta_{i+1} = \theta_i - \Delta\theta$  and the desorption rate  $r_{\text{des},i+1} = \Delta\theta/\Delta T$ .

The aim is now to minimize the sum of the squared deviations between the measured and the approximated desorption rates. Thus the programme changes the starting parameters randomly and calculates again the sum of deviations for the new parameters. The new parameters are then accepted according to a certain probability, depending on the change of the error. The whole procedure is done according to a simulated annealing strategy. Here you might be willing to change the stepwidth with which the new guessed parameters are determined and do so by changing the variable **sigma**.

Finally the program will plot the simulated result together with the measured values, display the best parameters and write them to the file **FittingValues.txt**.

## The Programme Code

```
#####  
% PolanyiFit.m  
% Author: Anton Tamtögl  
% Last modified: 01.05.2008  
% Dependencies: The functions peaksum.m and dthetadT.m are needed!  
#####  
% Fits experimental desorption rates by iteratively computed desorption  
% rates according to the Polanyi Wigner equation.  
#####  
  
clear all; close all;  
f1=figure('units','normalized','position',[0.005,0.07,0.99,0.88]);  
  
% experimental data, temperature = 1st column, desorption rate = 2nd column  
load('data.txt');  
T = data(:,1)'; % measured temperature during the TDS  
rateempirical = data(:,2)'; %measured desorption rate (QMS signal)  
rateempirical = (rateempirical-min(rateempirical)); %subtract the background  
  
% The empirical monolayer in particles / cm2. It may also be choosen  
% arbitrary, however the coverage output will not be correct in this case!  
monolayer = 2.6E-9;  
Peaks = 5; %how many peaks are used to fit  
  
% create a file named FittingValues.txt to output fitting parameters;  
fid = fopen('FittingValues.txt','w');  
  
#####  
% Choose the starting values for the fitting procedure:  
#####  
% all vectors start with the value of the peak at the lowest temperature!  
  
% order kinetics: vector with the orders of desorption of each single peak  
ordnbest = [ 0.5, 0.5, 0.5, 0.5, 2];  
% initial coverage: vector with the initial coverage [ML] of each peak  
initialcovbest = [ 0.4 , 0.45 , 0.55 , 1.2 , 0.7 ];  
% preexponential factor: vector with the exponent of nu for each peak  
nubest=zeros(1,Peaks);  
nubest(ordnbest==0.5)=8.5; nubest(ordnbest==1)=13; nubest(ordnbest==2)=22;  
% this nus work for the zinc-TDS but may need to be changed in other cases  
% desorption energy [eV]: vector with the desorption energy of each peak  
Ebest = [ 1.23 , 1.27 , 1.3 , 1.33 , 1.43 ];
```

```

% omega: coverage dependency paramter of Edes
omega=0.0; %omega=0 for a coverage-independent desorption energy
% heating rate beta: Set the same heating rate as used in the experiments!
beta=2;

% Define the stepwidths for the determination of the new fitting parameters
sigma = 0.001; % stepwidth for new guess values, default 0.001
initialcovsigma = sigma*0.1;
nusigma = sigma*0.1;
Esigma = sigma*0.02;
ordnsigma = sigma*0;

besterror = Inf;

#####
% Start the annealing procedure
% starting temperature chosen so that ~80% of the new values are accepted
AnnealTemp(1)=5;
q=0.9; %factor for the cooling down strategy

for mm = 1:20 %loop over annealing-temperature

    for ii = 1:10000 %loop per fixed annealing temperature

        % Now try to change the parameters randomly
        initialcov = initialcovbest+initialcovsigma.*randn(1,Peaks);
        nu = nubest+nusigma.*randn(1,Peaks);
        Edes = Ebest+Esigma.*randn(1,Peaks);
        ordn = ordnbest+ordnsigma.*randn(1,Peaks);

        % Compute the rate and the coverage using the new parameters
        [ thetaall, rateall, ratesum ] = ...
            ... peaksum(T,initialcov,10.^nu,Edes,ordn,beta,omega,monolayer);
        thiserror = norm((rateempirical-ratesum)); %error = sum of deviations
        diff=thiserror-besterror;

        % New parameters are accepted according to the Metropolis algorithm
        if min(1,exp(-diff/AnnealTemp(mm)))==1
            besterror = thiserror; initialcovbest = initialcov;
            nubest = nu; Ebest = Edes; ordnbest=ordn; thetabest = thetaall;
            ratebest = rateall; ratesumbest = ratesum;
        else
            r=rand(1);

```

```

        if r < exp(-diff/AnnealTemp(mm))
            besterror = thiserror; Ebest = Edes; ratesumbest = ratesum;
            ratebest = rateall; thetabest = thetaall; nubest = nu;
            ordnbest=ordn; initialcovbest = initialcov;
        end
    end
end

end %end of loops per fixed annealing temperature

%produce a plot of the fitted data
plot(T,rateall,T,ratesum,'c',T,rateempirical,'ko');
drawnow;

%decrease the annealing temperature
AnnealTemp(mm+1)=AnnealTemp(1)*q^mm;

end %end of temperature loop

#####
% Compute a plot with the best fitting values but use now more iterations
% for the temperature to get a smoother plot
Temp=linspace(min(T),max(T),1000);
[ thetaall, rateall, ratesum ] = ...
    ... peaksum(Temp,initialcov,10.^nu,Edes,ordn,beta,omega,monolayer);
plot(Temp,ratesum,'c',T,rateempirical,'ko',Temp,rateall);
legend('measured data','simulated data');

for kk=1:Peaks
    coverage(kk)=trapz(Temp,rateall(kk,:));
end
coverage = coverage/monolayer;
coveragesum = trapz(Temp,ratesum)/monolayer;
coverageempirical = trapz(T,rateempirical)/monolayer;

% Display the best fitting values
disp(['total coverage measured [ML] = ',num2str(coverageempirical)]);
disp(['total coverage calculated [ML] = ',num2str(coveragesum)]);
disp(['initial coverage [ML] = ',num2str(coverage)]);
disp(['nu = 10^ ',num2str(nu)]);
disp(['Edes [eV] = ',num2str(Edes)]);
disp(['Edes [kJ/mol] = ',num2str(Edes.*96.485)]);
disp(' ');

```

```
% Save the best fitting values to the file FittingValues.txt
fprintf(fid,'%s\n',['Error = ',num2str(besterror)]);
fprintf(fid,'%s\n',['total coverage measured [ML] = ', ...
    ... num2str(coverageempirical),'    total coverage calculated [ML] = ' ...
    ... ,num2str(coveragesum)]);
fprintf(fid,'initial covage [ML] = %6.3f    nu = 10^%4.3f    ...
    ... Edes [eV] = %6.3f\n',[initialcov ; nu ; Edes ]);
fprintf(fid,'\n');
disp('Fitting values written on FittingValues.txt!');
```

```

#####
% function peaksum.m
% Author: Anton Tamtögl
% Last modified: 01.05.2008
#####
% Computes the sum of all peaks according to the Polanyi Wigner for a given
% set of parameters
#####
% ----- input variables -----
% T ... temperature vector
% initialcov ... initial coverage for each peak, vector
% nu ... frequency factor for each peak, vector
% Edes ... desorption energy [eV] for each peak, vector
% ordn ... order of desorption for each peak, vector
% beta ... heating rate
% omega ... coverage dependency factor of Edes
% monolayer ... empirical monolayer in particles / cm2
#####
% ----- output variables -----
% thetaall ... coverage of the individual peaks, matrix
% rateall ... desorption rate of the individual peaks, matrix
% ratesum ... desorption rate of the cumulative peak, vector
#####

function [ thetaall, rateall, ratesum ] = ...
    ... peaksum(T,initialcov,nu,Edes,ordn,beta,omega,monolayer)

Peaks=length(Edes);
ratesum = zeros(1,length(T));
rateall = zeros(Peaks,length(T));
thetaall = zeros(Peaks,length(T));

for nn = 1:Peaks %loop over the peaks
    % calculate the coverage and desorption rate for one single peak
    [ theta, rate ] = dthetadT(T,initialcov(nn),nu(nn),Edes(nn), ...
        ... ordn(nn),beta,omega,monolayer);
    ratesum = ratesum + rate; %sum the rate of all peaks
    thetaall(nn,:) = theta;
    rateall(nn,:) = rate;
end

```

```

% #####
% function dthetadT.m
% Author: Anton Tamtögl
% Last modified: 01.05.2008
% #####
% Calculates the desorption rate and the coverage iteratively according
% to the Polanyi Wigner equation (for a given set of parameters)
% #####
% ----- input variables -----
% T ... vector with the temperature steps
% initialcov ... initial coverage in monolayer
% nu ... preexponential factor
% Edes0 ... desorption energy at zero coverage
% ordn ... order of desorption
% beta ... heating rate
% omega ... coverage dependency paramter of Edes
%       Edes = (1-omega*coverage)*Edes_0
% monolayer ... emperical monolayer in particles/cm^2
% #####
% ----- output variables -----
% theta ... approximated coverage at each temperature step (vector)
% rate ... approximated desorption rate at each temperature step (vector)
% #####

function [ theta, rate ] = ...
    ... dthetadT(T,initialcov,nu,Edes0,ordn,beta,omega,monolayer)

k=8.6*10^-5; %Boltzmann constant in eV/K

thetareal=zeros(1,length(T));
thetareal(1)=initialcov*monolayer; %calculate the coverage in particles/cm^2
rate=zeros(1,length(T));

%loop over the temperature steps
for kk=2:length(T);
    %New desorption energy due to the coverage dependence
    Edes=(1-((thetareal(kk-1)/monolayer))*omega)*Edes0;
    Td=Edes/k;
    deltaT=(T(kk)-T(kk-1));
    Temp=T(kk-1)+deltaT/2;
    %calculate the change of the coverage dtheta at the temperature T+dT/2
    Arrh=nu/beta*thetareal(kk-1)^ordn*exp(-Td/Temp)*deltaT;
    thetaneu=thetareal(kk-1)-Arrh; %new coverage = old coverage - dtheta

```

```
thetareal(kk)=thetaneu;
rate(kk)=Arrh/deltaT; %rate = dtheta/dT
% truncation condition: exits the loop if the actual coverage is ~0
if thetaneu<eps
    break
end
end
end

theta=thetareal/monolayer; %return theta in terms of monolayer
```